Microstructural Modifications of Copper Zinc Oxide Catalysts as a Function of Precipitate Ageing

vorgelegt von

Diplom-Chemiker

Benjamin-Louis Kniep

aus Leonberg

Fakultät II – Mathematik und Naturwissenschaften
der Technischen Universität Berlin
zur Erlangung des akademischen Grades
Doktor der Naturwissenschaften
-Dr. rer. nat.-

genehmigte Dissertation

Promotionsausschuss

Vorsitzender:	Prof. Dr. rer. nat. M. Gradzielski
Berichter/Gutachter:	Prof. Dr. rer. nat. M. Lerch
Berichter/Gutachter:	Prof. Dr. rer. nat. R. Schlögl

Tag der wissenschaftlichen Aussprache: 5. Juli 2005

Berlin 2005

D 83

Microstructural Modifications of Copper Zinc Oxide Catalysts as a Function of Precipitate Ageing

Dissertation vorgelegt von Benjamin-Louis Kniep

Abstract

Microstructural characteristics of copper zinc oxide catalysts for methanol steam reforming (MSR) were investigated as a function of ageing of the precipitated hydroxycarbonates during catalyst preparation. Microstructural changes of the active catalysts were determined by in situ X-ray diffraction (XRD) and in situ X-ray absorption spectroscopy (XAS) combined with on-line mass spectrometry, nuclear magnetic spin resonance (NMR) and transmission electron microscopy (TEM). The strong increase in catalytic activity observed for Cu/ZnO catalysts obtained from precipitates aged for more than 15 min cannot be explained alone by the higher Cu surface area of the catalysts, as determined by N_2O decomposition. The microstrain in the copper particles as detected by XRD, NMR, and XAS was determined as an additional bulk structural parameter that correlates with the increase in catalytic activity. Additionally, TEM investigations show that the less active Cu/ZnO catalyst (non-aged precipitate) comprises a heterogeneous microstructure of large and isolated Cu and ZnO particles, whereas the more active catalyst (120 min aged precipitate) shows small and intimately mixed Cu and ZnO particles (homogenous microstructure). Moreover, continuous precipitate ageing leads to a decreasing amount of Zn in the copper clusters of the Cu/ZnO catalysts. A schematic model of the structural characteristics of Cu/ZnO catalysts as a function of precipitate ageing is proposed. The model emphasizes the defect-rich state of the homogeneous microstructure of Cu/ZnO catalysts and its implication for the catalytic activity in the steam reforming of methanol.

The present work reports, that microstructural characteristics of a “real catalyst” can be controlled by suitable preparation conditions. The preparation of Cu/ZnO catalysts by precipitation of mixed metal hydroxycarbonates is a multi-step process, including ageing, washing, drying, calcination and reduction. Ageing of freshly precipitated precursors leads to characteristic phase transformations and enables designing a desired catalyst performance by modifying the precipitation conditions instead of varying the chemical composition. All materials obtained from the intermediate preparation procedures (i.e. calcination and reduction) exhibit a “chemical memory” on their treatment during the first stages of preparation (i.e. ageing) and none of the subsequent treatment procedures appears to erase that memory and level out the characteristic structural differences.

Mikrostrukturelle Modifizierungen von Kupfer-Zinkoxid Katalysatoren als Funktion der Alterung der Vorstufen

Dissertation vorgelegt von Benjamin-Louis Kniep

Kurzzusammenfassung

Im Rahmen dieser Arbeit wurde der Einfluss der Alterung von ausgefällten Kupfer-Zink-Hydroxycarbonaten auf die mikrostrukturellen Eigenschaften der resultierenden Kupfer-Zinkoxid-Katalysatoren für die Methanoldampfreformierung untersucht. Die Mikrostruktur des aktiven Katalysators wurde mit in situ Röntgenbeugung (XRD) und in situ Röntgenabsorptionsspektroskopie (XAS) jeweils kombiniert mit Massenspektrometrie (MS), sowie magnetischer Kernspinresonanz (NMR) und Transmissionselektronenmikroskopie (TEM) bestimmt. Die deutliche Zunahme der katalytischen Aktivität der Cu/ZnO Katalysatoren, die aus Vorstufen hergestellt wurden die für mehr als 15 Minuten in der Mutterlauge gealtert wurden, ist nicht ausschließlich auf eine Vergrößerung der Kupferoberfläche zurückzuführen. Als zusätzlicher volumenstruktureller Parameter korreliert die Mikroverspannung in den Kupferclustern mit der Zunahme der katalytischen Aktivität, wie durch Analyse der XRD, XAS und NMR Messungen belegt werden konnte. TEM-Untersuchungen zeigten, dass die weniger aktiven Cu/ZnO-Katalysatoren (ungealtert) eine heterogene Mikrostruktur aus großen, voneinander isolierten Cu- und ZnO-Partikeln aufweisen, wohingegen die aktiveren Katalysatoren (120 min gealtert) aus kleinen, eng miteinander verknüpften Cu- und ZnO-Partikeln bestehen (homogene Mikrostruktur). Des Weiteren konnte gezeigt werden, dass zunehmende Alterung der Vorstufen zu einem abnehmenden Anteil an Zn in den Kupferclustern der Katalysatoren führt. Auf der Basis dieser experimentellen Befunde wurde ein schematisches Model über die strukturellen Eigenschaften von Cu/ZnO-Katalysatoren als Funktion der Alterung der Vorstufen aufgestellt, in dem der positive Einfluss einer defektreichen homogenen Mikrostruktur der Cu/ZnO-Katalysatoren auf die katalytische Aktivität in der Methanoldampfreformierung beschrieben wird.

In dieser Arbeit konnte gezeigt werden, dass mikrostrukturelle Eigenschaften von „Real-katalysatoren“ durch geeignete Wahl der Präparationsbedingungen bestimmt werden können. Die Präparation von Cu/ZnO-Katalysatoren aus Fällung von gemischten Metall-hydroxycarbonaten ist ein mehrstufiger Prozess, indem die Vorstufen gealtert, gewaschen, getrocknet, kalziniert und reduziert werden. Das Altern der Fällungsprodukte führt zu charakteristischen Phasenumwandlungen und ermöglicht das „Design“ des gewünschten Katalysators, indem die Präparationsbedingungen und nicht die chemische Zusammensetzung variiert werden. Alle Materialien, die durch die zwischengelagerten Präparationsschritte erhalten wurden (z.B. Kalzinierung und Reduktion) zeigen ein „chemisches Gedächtnis“ gegenüber des ersten Präparationsschrittes (d.h. Altern). Die charakteristischen strukturellen Unterschiede, die durch gezieltes Altern bestimmt wurden, bleiben auch nach den nachfolgenden Präparationsschritten erhalten.

Danksagung

Diese Arbeit wurde im Zeitraum vom Januar 2002 bis Juni 2005 in der Abteilung Anorganische Chemie am Fritz-Haber Institut der Max-Planck Gesellschaft angefertigt.

Herrn Prof. Schlögl danke ich für die interessante Themenstellung und die Möglichkeit ein anwendungsorientiertes Thema aus der Festkörperchemie sowohl präparativ als auch charakterisierend zu bearbeiten. Herrn Prof. Lerch danke ich für die Übernahme des Zweitgutachtens.

Des Weiteren danke ich Herrn PD Dr. Ressler für die Einführung in die Röntgen-absorptionspektroskopie und sein andauerndes Interesse an dieser Arbeit. Seine tatkräftige Unterstützung und stete Diskussionsbereitschaft haben wesentlich zum Gelingen dieser Arbeit beigetragen.

Weiterhin möchte ich all denen danken, die durch ihre Unterstützung und ihr Know-How das Zustandekommen dieser Arbeit ermöglicht haben: Ernee Muhamad und Gisela Lorenz für die perfekte Hilfe bei der Präparation; Manfred Swoboda, Dr. R. Jentoft und der Werkstatt, ohne die die Realisierung neuer experimenteller Aufbauten gar nicht möglich gewesen wäre; Igor Kassatkine für den bildgebenden Einblick in die reale Struktur des Katalysators ; Michael Hävecker für die XPS Experimente, die glücklicherweise zu eher unerwarteten Ergebnissen geführt haben, Annegrit Rabis für die NMR Untersuchungen und die Unterstützung bei der doch recht komplexen Interpretation.

Alexandra Szizybalski sei für die angenehme Atmosphäre in unserem Büro gedankt, sowie der Möglichkeit, Pflanzen in ungeahntem Tempo wachsen zu sehen. Den Mitgliedern der Gruppe Geometrische Strukturen danke ich für die Hilfe an manchmal doch recht langwierigen Messzeiten in Hamburg. Darüber hinaus gilt mein Dank allen Mitarbeitern der Abteilung Anorganische Chemie für die kollegiale Atmosphäre.

1 Introduction

1.1 Catalytic Hydrogen Production from Methanol

The combustion of oil, coal and natural gas still provided 80% of the primary energy consumed worldwide in 2002 [1]. The resulting CO_2 emissions have caused a significant increase of the concentration of CO_2 in the atmosphere during the last decades from 15700 mT (1973) to 24100 mT (2002). There is strong evidence that the growth of the atmospheric concentration of CO_2 is the origin of the increase of the average global temperature observed during the last century, the so called "greenhouse effect". It is suggested that the emissions of greenhouse gases could lead to an increase in global mean temperatures of about 1-4 degree centigrade at the end of this century. Thus, many international organizations and a large part of the public are calling for a significant reduction of CO_2 emissions. A more efficient use of renewable energy sources such as biomass, sunlight, wind, and geothermal power would lead to a decrease in CO_2 emissions.

A most promising solution as alternative energy source is hydrogen. Hydrogen ideally produces only water during combustion, which makes it an interesting alternative for decreasing CO_2 emission. Since 27% of the worldwide CO_2 emission is caused by transportation, hydrogen can be used as fuel to power vehicles with fuel cell engines. Generating electricity by the chemical process, combining hydrogen and oxygen to form water, produces no emissions at all. Other advantages of using hydrogen in the fuel cell in comparison to the conventional internal combustion engine are higher energy efficiency, low noise, no formation of soot particle, which can impact the human health. In addition, hydrogen is used in large quantities in the chemical industry. The largest proportion of hydrogen in the world is consumed for ammonia synthesis (Haber-Bosch Synthesis). Furthermore, hydrogen is used for the hydrogenation of hydrocarbons (e.g. coal, natural gas, tar and organic fats), the synthesis of hydrogen chlorides, rocket fuel, and as reduction agent to manufacture metals (e.g. Mo, W, Co, Ge).

Hydrogen can be produced from fossil, renewable sources and by electrolysis of water using solar energy. The largest quantities are manufactured from natural gas. However, storing hydrogen on board a vehicle poses many concerns regarding safety and handling. The use of hydrogen as an automotive fuel requires storage systems that have inherent safety as well as volumetric and gravimetric efficiency. H_2 can be stored as compressed gas, cryogenic liquid,

hydrocarbon liquids, liquid ammonia or solid metal hydrides. Especially solid metal hydrides such as numerous alloys and intermetallic compounds that have reversible hydriding properties and liquid ammonia which can be cracked into his constituents hydrogen and nitrogen are subject of ongoing research. Another alternative to storage hydrogen on board is to carry liquid fuels that have high energy densities and convert those to a hydrogen-rich gas via an on-board fuel cell processor. One of the most favorable liquid fuels used to produce hydrogen on board is methanol. Methanol is a primary alcohol with a high hydrogen-to-carbon ratio, which can be produced from renewables, such as natural gas and biomass.

In principle, there are four routes available for the catalytic generation of hydrogen from methanol, which can be carried out at moderate temperatures (200°C - 300°C) using transition metal catalysts [2]:

Decomposition: $CH_3OH \rightarrow CO + 2\ H_2$ $\Delta H^0_{298} = +92\ kJ\ mol^{-1}$ **(1-1)**

Partial Oxidation: $CH_3OH + ½\ O_2 \rightarrow CO_2 + 2\ H_2$ $\Delta H^0_{298} = -192 kJ\ mol^{-1}$ **(1-2)**

Steam Reforming: $CH_3OH + H_2O \rightarrow CO_2 + 3\ H_2$ $\Delta H^0_{298} = +50\ kJ\ mol^{-1}$ **(1-3)**

Autothermal Reforming: $CH_3OH + (1\text{-}2\delta)\ H_2O + \delta O_2 \rightarrow CO_2 + (3\text{-}2\delta)\ H_2$

if δ = 0.25 $\Delta H^0_{298} = -71\ kJ\ mol^{-1}$ **(1-4)**

The decomposition is less suitable for catalytic hydrogen generation because the reaction is strongly endothermic and requires a lot of energy to operate, the reaction produces stoichometrically less H_2 compared to the reforming reactions (1.3; 1.4), and the large concentration of CO (CO is poison the fuel cell performance). In contrast, the partial oxidation offers some advantages over the decomposition since the reaction route is exothermic, i.e. thermodynamically favourable [3]. However, partial oxidation with oxygen yields H_2 and CO_2 almost quantitatively at a 2:1 ratio. If air is used as oxidant, the reformate gas also contain about 40% nitrogen. Because of this drawback, the partial oxidation is found to be less suitable for the catalytic hydrogen production. On the other hand, for the purpose of fuel cell in mobile application, the steam reforming reaction is considered to be the most suitable since the reaction produces stoichiometrically more H_2 than is actually available in methanol alone due to the participation of water in the overall process. Moreover, the by-product is CO_2 rather than CO. Although the autothermal reforming is frequently discussed as alternative reaction route to produce hydrogen [4] since the heat requirement can be provided by the reaction itself (autothermal reaction), the H_2 to CO_2 ratio was found to be below the

steam reforming [5,6,7]. The high H_2 production capacity is the main argument for choosing the steam reforming process over the other available reaction routes.

Many different reaction pathways for the steam reforming of methanol have been suggested in the literature. Controversies remain concerning the reaction sequence and the intermediates formed during catalytic conversion. In principle, the key reactions are some combination of the direct interaction between methanol and water (1.3), the decomposition (1.1) and the water-gas shift reaction ($CO + H_2O \rightarrow CO_2 + H_2$) [8]. In particular, CO and methyl formate formation were found as intermediate products in many reaction mechanism studies. Formic acid, formaldehyde and dimethyl ether have also been observed by some researchers [9,10,11]. Purnama et al. [12] found that CO is formed as consecutive product by reverse water-gas shift reaction on Cu/ZrO_2 catalysts. The currently suggested mechanism over $Cu/ZnO/Al_2O_3$ catalysts first proposed by Jiang et al. [10] is given below:

$$CH_3OH \rightarrow CH_3O_a + H_a$$
$$CH_3O_a \rightarrow CH_2O_a + H_a$$
$$H_2O \rightarrow H_2O_a$$
$$2\ H_a \rightarrow H_2$$
$$2\ CH_2O_a \rightarrow CH_3OCHO_a$$
$$CH_3OCHO_a + H_2O_a \rightarrow HCOOH_a + CH_3OH$$
$$HCOOH_a \rightarrow H_2 + CO_2$$

The mechanism of steam reforming strongly depends on the composition and nature of the catalyst, e.g. behavior of the transition metal and the support. Different types of supported transition metal such as copper, platinum, rhodium, palladium, and nickel are known to be active for the steam reforming of methanol. Takezawa et al. reported that the steam reforming activity of group 9-10 transition metal catalysts was much poorer than that of copper-based catalysts, due to differences in reactivity of formaldehyde species [13]. Consequently, copper based catalysts have received considerable attention. The effect of transition metal modified copper catalysts (Cu-Zn, Cu-Zr, Cu-Cr, Cu-Mn, Cu-Fe, Cu-Ti) on the selectivity and activity in methanol steam reforming was also investigated [14,15]. Transition metal catalysts are usually supported by metal oxide such as ZnO, Al_2O_3, SiO_2, ZrO_2, CeO_2. Controversies remain concerning the rule of the support on the catalytic generation of hydrogen from methanol.

Cu-based catalysts are active in a large variety of methanol related catalytic reactions. Especially, Cu/ZnO-based catalysts are of large importance due to their high selectivity to H_2 and CO_2 in methanol steam reforming.

1.2 Preparation of Cu/ZnO-based catalysts

1.2.1 Methods

Various preparation routes are available to prepare Cu/ZnO catalyst. These include processes, such as impregnation [16], co-precipitation [17,18,19,20], sol-gel techniques [21], chemical vapor deposition (CVD) [22], and mechanical milling [23]. The most appropriate method for industrial catalysts preparation is the co-precipitation. Since complete mixing at the molecular level is possible in solution, a solution of all the metal salts is taken as the common starting material leading to a homogenous solid precursor. The first catalyst for low pressure methanol process (ICI) was prepared by continuous precipitation from mixed metal nitrates (Cu, Zn, Al) and sodium carbonate [24]. The major advantage of precipitation is the flexibility of the process with respect to the specific properties of the precursor and the resulting catalyst. These properties could be the chemical composition, purity, homogeneity, particle size, surface area, the nature of the phase formed, pore size, epitaxy and intergrowth, chemical and structural disorder and many more. The precursors can be chemically modified by the precipitating agent, solvent, additives, complexing agent, as well as physically modified by the addition rate of precipitating agent, temperature, stirring velocity, reactor volume and pH. Thus, precipitation (co-precipitation) of Cu/ZnO catalysts enables to control and design the specific catalyst characteristics. A more detailed description of the parameters effecting the precipitation is given in chapter 1.2.2.1.

1.2.2 Co-precipitation of Cu/ZnO-based catalysts

Different precipitating agents have been employed for the common precipitation route in aqueous solution to obtain Cu, Zn (Al) based precursors, e.g. sodium carbonate [17], oxalic acid [19], ammonia [20,25], sodium aluminate [18] and urea [26]. Industrially prepared Cu, Zn (Al) catalysts are precipitated by using metal nitrate solution and sodium carbonate as precipitating agent. The following crystalline phases were identified in the precipitates:

$Cu_2(OH)_2CO_3$ (malachite), $Cu_2(OH)_3NO_3$ (gerhardite), $Zn_5(OH)_6(CO_3)_2$ (hydrozincite), $(Cu_{1-x}Zn_x)_5(OH)_6(CO_3)_2$ (aurichalcite), $(Cu_xZn_{1-x})_2(OH)_2CO_3$ (rosasite), $(Cu/Zn)_2(OH)_2CO_3$ (georgeite) as well as aluminum containing phases such as $Al(OH)_3$, $(Cu_xZn_{1-x})_{16}Al_2(OH)_6CO_3*4H_2O$ (roderite), and sodium containing phases, e.g. $NaNO_3$ and $Na_2Zn_3(CO_3)_4 * 3H_2O$.

Depending on the preparation conditions and catalyst composition, the precursor occurs either in monophasic or multiphasic hydroxycarbonate phases. It is commonly aceppted that the copper zinc containing hydroxycarbonate phases (rosasite, aurichalcite, georgeite) result in the most active and stable catalyst. However, the relation between the chemical, structural and morphological identity of the precursor to the activity of the final catalyst still remains unclear [27]. The preparation of Cu/ZnO catalysts via co-precipitation is a multistep procedure. The typical reaction route contains the ageing of the precursors in the mother liquor, followed by washing, drying, calcination and reduction. In principle, each preparation step affects the performance of the final catalyst.

1.2.2.1 Crystallization in solution

The crystallization in solution is a sequence of consecutive events of nucleation, growth, phase transition, ripening, and aggregation. The crystallization in aqueous solution enables a large flexibility in a controlled manufacturing of solids, because the reaction profile is shifted from a thermodynamic to kinetic driving forces (Figure 1).

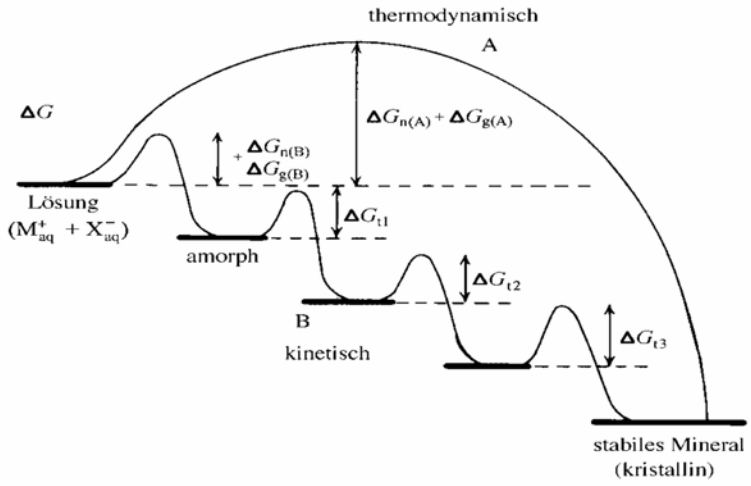

Figure 1: Thermodynamic (path A) and kinetic control of crystallization (path B). [***28***]

In a thermodynamic controlled process the product with the highest thermodynamic stability is formed first (i.e. the product with the lowest Gibbs Energy). In a kinetically controlled process the product with the highest rate of formation is formed first (i.e. the product with the lowest reaction path activation energy). A kinetically controlled crystallization proceeds in a multi sequential reaction route of increasingly stable intermediates (small activation energies), which often involves and initial amorphous phase that may be susceptible to rapid phase transformations. Phase transitions in solution by dissolution-renucleation processes depending on the solubilities of the phase formed and their free activation energies of their interconversions. A brief introduction of the major events during crystallization in solution, such as nucleation, growth, ripening, phase transition, and aggregation is described in the following.

Nucleation and Growth: The classical nucleation theory given by Gibbs [29], provides a description of the nucleation process in terms of the total energy change of the system (ΔG) during particle formation. The total energy is given by the sum of two contributions: The nucleus/solution interface energy, proportional to the square of the radius, which increases the total energy of the system and the bulk lattice energy, proportional to the cube of the particle radius, which alone leads to a decrease of the total energy of the system. At the beginning of nucleation, the interfacial energy dominates, and the total energy of the system increases. At some point, the so-called critical radius of the nucleus, the bulk lattice energy dominates the total energy change of the system, and the total energy decreases with further particle growth. Thus, continuous particle growth is energetically favored instead of the formation of new nuclei, because ΔG becomes more negative. Several smaller contribution, such as motion of the particles, defect energies and electrostatic contributions affect the total free energy, but can be neglected for this model.

Supersaturation of the aqueous solution controls both, nucleation and growth processes. From the metal ions in solution a precursor species is formed, for instance by hydrolysis or raising the pH. A critical precursor (e.g. metal ion) concentration in the solution must be exceeded to form a nucleus from uncharged precursors. As long as the concentration of metal ions stays above the critical concentration, new nuclei are formed. As soon as concentration falls below the critical metal ion concentration due to consumption by nucleation, only particle growth of the existing particles takes place.

Aggregation: An additional model for the growth mechanism is the aggregation. In the classical crystallization model, stable nuclei are enlarged by unit-cell replication without taking into account structural changes in the bulk or at the surface. The model neglects the role of aggregation which can result in larger particles than expected from the classical model. Crystal growth by aggregation of already present particles is a mesoscale assembly process. Primary nano particles can be attached stepwise to a growing assembly of aligned building blocks to produce, for example, chains of orientated nano crystals [28]. The aggregation process is expected to be important in the crystallization and particle growth of copper oxalates [30] and copper oxides [31], that can readily undergo cluster formation in aqueous solution.

Ripening: The so called "Ostwald ripening" is the growth of larger crystals on the expense of those of smaller size which have a higher solubility than the large one. Ostwald ripening only concerns particles with the same structure, e.g. same phase. Upon crystallization the mother liquor consist of crystals of different sizes according to the time on which they are formed and their growth rate. The equilibrium of a solid state phase and the corresponding solute is determined by the solubility of the crystalline phase. The solubility of small particles is larger than the solubility of larger ones. Thus, two particles of different sizes are surrounded by spheres of different concentration. The intersection of both spheres results in a mass transfer of the solute from the small particle to the larger particle. In order to achieve the equilibrium condition between a solid and its solute, the smaller particle must partially dissolve, whereas the large particles begin to growth. Consequently, the dissolution processes finally result in the disappearance of the smaller particles. With increasing time only one crystal should remain in the system. Osswald ripening is very fast for crystals of a radius less than 1 μm, but very slow as soon as the crystals reach about 100 μm [32].

Phase transition: In closed systems, there is a continuous decrease of the supersaturation when crystallization occurs. If a solution is supersaturated with respect to many phases at the same time, it is often the phase of highest solubility, i.e. the less supersaturated, which crystallites first, according to "Ostwalds rule of stages" [33]. Ostwalds rule only concerns phases with exactly the same chemical composition but different crystal structures (polymorphs). Under defined experimental conditions (e.g. temperature, pressure, composition) only one polymorphous solid state is thermodynamically stable and all the other

metastable phases disappear as function of time (Figure 1). However, the metastability of the solids does not preclude their existence for a relatively long time period. According to Ostwalds Law, the metastable phase is formed as the initially precipitate (phase A). At this point the solution is supersaturated with respect to a thermodynamically more stable phase (phase B) so that it is reasonable to suppose that some nuclei of phase B are formed. The formation and the growth of the particles of the stable phase result in a decrease of the solute concentration and the solution becomes undersaturated with respect to the metastable phase. Thus, phase A crystals dissolve rapidly producing supersaturation for the continued growth of phase B. A large variety of the so called solvent-meditated phase transformations are known [34]. For example, transformation of amorphous calcium carbonate in crystalline vaterite or transformation from amorphous calcium phosphate to hydroxyapatite and many more.

1.2.2.2 Parameters effecting the precipitation

Precipitation processes such as nucleation, growth, ripening, and phase transitions are strongly influenced by the preparation conditions. Thermodynamic variables (solution composition, cation concentration, redox potential of the solution, complexing agents), kinetic variables (reactor size, rate of addition, stirring velocity) and coupled parameters (e.g. pH, temperature) affect the reactivity of the solids formed in the solution.

The effect of solution composition and cation concentration on the catalytic activity of precipitated Cu,Zn hydroxycarbonates has been extensively investigated [17, 24, 35, 36]. A successive change form malachite, rosasite, multiphasic composition of aurichalcite/rosasite, and hydrozincite precursors with increasing zinc cation concentration was found. The maximum activity is observed in an intermediate compositional range of precursors obtained by Cu to Zn concentration in the solution of 70/30 mol%. In addition to copper to zinc ratio, precipitation pH, and temperatures affect the composition of the precursor and the resulting activity. Li and Inui [37] concluded that co-precipitation of Cu/Zn/Al precursors with a constant atomic ratio of 6/3/1 should be performed at pH of 7 and 343 K. Recently, it was demonstrated that kinetic variables strongly affect the quality of precipitated Cu,Zn hydroxycarbonates [38] by comparing continuous “micro reactor” precipitation with the standard batch precipitation. The precipitate in a micro reactor is formed in the shortest possible time and a small volume of solution, which enables the exclusion of kinetically controlled process parameters such as stirring velocity, reactor size and rate of addition. M.

Schur et al. concluded that a change in kinetic boundary conditions of the precipitation reaction, through short reaction times, a small volume and efficient temperature control leads to a usable catalysts.

The co-precipitation of Cu/ZnO catalysts is a multi-step preparation process, including ageing, washing, drying, calcination, and reduction. During ageing and washing of the catalyst precursor, complex processes occur such as redissolution, recrystallization, and ion exchange, which are similarly affected by the process parameters (e.g. pH, temperature, reactor size, stirring velocity). In principle, each preparation step affects the microstructure and the resulting activity of the final catalyst. It is therefore necessary to optimize and control the preparation parameters in order to produce the desired material.

1.3 Motivation

Recent investigations on differently prepared Cu/ZnO-based catalysts clearly indicate significant changes in the catalytic activity per unit of Cu surface area. In addition, microstructural characteristics of the catalysts such as morphology, particle size, microstrain, structural disorder, impurities, or different surface terminations affect the catalytic activity. The properties of the active catalysts are determined by the characteristics of the precursors. A fundamental understanding of the relation between surface structure, bulk structure, and catalytic activity is necessary to elucidate pathways to design highly active catalysts. Furthermore, with respect to a “knowledge based catalyst design”, only a detailed synthetic understanding of each preparation step and the control of the preparation parameters enables to synthesize improved catalysts.

The effect of preparation on the activity and microstructure of co-precipitated Cu/ZnO catalysts with varying molar ratios of Cu to Zn was investigated in previous works [17,36]. A strong relation between the precursor structure formed during co-precipitation of metal hydroxycarbonates at constant pH (pH=7) and their resulting microstructure of the final catalyst was found. M. Günter [36] ascribes an enhanced activity to structurally disordered (strained) copper particles. The work was related to differently precipitated copper based catalysts (constant and decreasing pH, varying molar ratio) prepared by B. Bems [17]. In addition, the effect of selected preparation steps (e.g. ageing, washing and calcination) on the precursor formation of a sample with a cation ratio of Cu/Zn 70/30 mol% was investigated. This work is related to the previous investigations of B. Bems and M. Günter.

The aim of the present investigation is to elucidate the effect of precipitate ageing on the microstructural modifications of Cu/ZnO catalysts for methanol steam reforming. It is assumed that ageing in the mother liquor of freshly precipitated Cu,Zn hydroxycarbonates allows designing the desired catalyst properties by tailoring the preparation conditions instead of varying the chemical composition. Although the positive influence of precipitate ageing on the catalytic activity of Cu/ZnO catalysts has been described in the literature [39,40,41], bulk structure-activity relationship still remains unclear.

The influence of differently aged precursors on selected post treatment steps (i.e. calcination and reduction) is investigated using the two complementary bulk methods in-situ X-ray absorption spectroscopy (XAS) and X-ray diffraction (XRD) in combination with on-line mass spectrometry (MS) as well as thermogravimetric measurements (TG) and UV-Vis spectroscopy. The structure of the active catalyst under working conditions is investigated by using in situ XRD, XAS and ex-situ Cu^{63} nuclear spin resonance (NMR). High-resolution transmission electron micrography (HRTEM) of freshly reduced catalysts obtained from differently aged precursors enable to study the morphology and microstructure of the catalysts. Thus, HRTEM is an additional tool to compare the results obtained by integral bulk structural methods with the morphological arrangement and performance of the catalysts. Furthermore, the surface structure of the catalysts is studied by X-ray photon spectroscopy (XPS). Finally, a combined in-situ XAS/UV-Vis cell is developed in order to elucidate the relationship between electronic structure, geometric structure and the activity of the catalysts.

In summary, structure-activity relationships of Cu/ZnO catalysts prepared under industrial conditions are necessary to prepare improved catalyst. Several suggestions were made to the nature of the “real” structure of the copper phase under reaction conditions including the simplifying assumption that activity increases linearly with the copper surface area. However, bulk structural characteristics such as microstrain, impurities, structural disorder, and particle size may significantly influence the performance of the corresponding copper catalyst. The use of complementary characterization methods may allow unraveling the relation between structural characteristics of the catalyst and the chemistry of the precursor phase. In addition to precipitate ageing, each step in subsequent treatment of the precipitate and the resulting oxide precursor affects the microstructure of the active catalyst (chemical memory). This work is focused on elucidating the microstructural modifications of Cu/ZnO catalysts and the ability to tailor such characteristics by subsequent ageing of freshly precipitated hydroxycarbonate precursors. The “chemical memory” of the differently aged precipitates is

investigated on selected post treatment steps such as calcinations and reduction. A microstructural model of the active catalyst as function of ageing and its influence on the catalytic activity is proposed. The present work clearly demonstrates that ageing allows designing the desired properties of Cu/ZnO catalysts and is thus a first step in direction to a knowledge based catalyst design.

2 Experimentals

2.1 X-ray diffraction (XRD)

X-ray diffraction can be used for the identification of crystalline bulk phases, the crystallinity, and to estimate particle size, microstrain and texture effects. The method based on elastic scattering of X-rays by the atoms of an ordered crystal. An ordered crystal can be described as regular repeating array of packed atoms, ions or molecules leading to a three-dimensional lattice. Diffraction in crystals occurs if the scattered waves from atoms of parallel lattice planes interfere constructively. The requirements for constructive interference are given by the Bragg equation ($n\lambda=2d \sin\theta$), with λ the X-ray wavelength, n the order of reflection, d the spacing of the lattice planes, and θ the angle between the incoming X-rays and the normal of the reflecting lattice plane. The equation relates the spacing between a set of parallel lattice planes with Miller indicies *hkl* (d_{hkl}) to the particular Bragg angle (θ_{hkl}) at which diffractions from this planes are observed. The intensity of a reflection I_{hkl} is proportional to the square of the structure factor $|F_{hkl}|$. The structure factor is dependent on both the position of each atom in the crystal and its scattering factor,

$$F_{hkl} = \sum_j f_j e^{2\pi i i(hx_j+ky_j+lz_j)} \qquad \textbf{(2-1)}$$

where fj is the scattering factor of the j^{th} atom and x_j, y_j, z_j are its fractional coordinates. Diffractogramms are measured as a function of the 2θ angle and thus enable to identify phases by calculating the d spacing of the lattice. Furthermore, simulation of the reflex intensities and their positions using least-squares methods allows refining the position and occupation factors of the atoms in the lattice.

2.1.1 Diffraction-Line profile analysis

XRD lines are usually broadened in their shape. Broadening of X-ray diffraction line profiles is mainly caused by non-ideal optics of the instrument, wavelength dispersion, and microstructural imperfections of the crystal. The microstructural line broadening can be subdivided in size broadening and strain broadening. Size broadening is due to the finite size of domains by stacking faults, by twins or other imperfections, which diffract incoherently

with respect to another. In principle, domain size is not generally the same as particle size, crystal size and crystallite size. The size of coherently diffracting Domains *D*, with the wavelength λ, and the diffraction angle 2θ, is related to line broadening β_D by the Scherrer formula:

$$\beta_D = \frac{\lambda}{D\cos\theta} \qquad \textbf{(2-2)}$$

On the other hand, strain broadening is caused by varying displacement of the atoms with respect to their reference-lattice positions. A uniform compressive or tensile strain (macrostrain) results in a peak shift of the X-ray diffraction lines, whereas a non-uniform statistic distribution of both tensile and compressive strain result in a broadening of the diffraction lines (microstrain). Line broadening β_S caused by inhomogeneous lattice strain ε is given by the following equation:

$$\beta_S = 4\varepsilon\tan\theta \qquad \textbf{(2-3)}$$

Both effects are interconnected, which makes it difficult to separate size and strain contribution underlying a XRD line.

Many approaches exist for the evaluation and separation of microstructural size and strain parameters from the occurring line broadening. Two methods were employed in this work: Separation of size and strain by using either a “single-line analysis” [42] or a “multiple-line analysis” (Williamson-Hall) [43]. For the single line profile analysis a Pseudo-Voigt function, which is a combination of a Lorentzian and Gaussian function is used,

$$f(x) = \eta L + (1-\eta)G \qquad \textbf{(2-4)}$$

with the Lorentzian part *L*, the Gaussian part *G* and the shape parameter η. The shape parameter can be refined as a linear function of 2θ wherein the refinable variables are *NA* and *NB* (η=*NA*+*NB**(2θ)*). The integral breadth of the Lorentzian part β_L and Gaussian part β_G can be calculated using the shape parameter η and the integral breadth of the corresponding line β:

$$\frac{\beta_L}{\beta} = 0.01745 + 1.50048\eta - 0.534156\eta^2 \qquad \textbf{(2-5)}$$

$$\frac{\beta_G}{\beta} = 0.18446 + 0.81269(1-0.998497\eta)^{1/2} - 0.534156\eta + 0.44542\eta^2 \qquad \textbf{(2-6)}$$

The volume weighted size part D and the average strain ε can be obtained from equation (2-2)

and (2-3) ($\beta_L=\beta_D$; $\beta_G=\beta_S$).

An alternative method to determine crystallite size and microstrain by analyzing X-ray diffraction line profiles is described by Williamson and Hall [24]. An hkl-indexed plot of the integral breadth in reciprocal space ($\beta^*= \beta\cos\theta/\lambda$) as function of the reciprocal lattice spacing ($d^*= 2\sin\theta/\lambda$) yields size and strain from the intercept and slope of the resulting line, respectively. An isotropic distribution of both size and strain is a prerequisite for a linear correlation between d* und ß* and the applicability of the Williamson-Hall analysis.

X-ray powder diffraction patterns were analyzed by the Pawley method ("full pattern refinement"). Therefore, a sum of Pseudo-Voigt profile functions and an appropriate background function were refined to the experimental X-ray diffraction patterns. Free running parameters in the refinement were the lattice constants, the intensities and the Gaussian and Lorentzian parts of the profile of the individual hkl lines, a linear zero shift in the 2θ scale, and four coefficients for the background polynomial.

In this work, X-ray diffraction (in-situ and ex-situ) was performed to analyze particle size, microstrain, and the phase composition. Size and strain analysis was done by profile refinement using WinXAS 3.2 [44]. Quantitative phase analysis was done with the program PowderCell 2.4 [45]. Structural data were taken from the single crystal database ICSD (Inorganic Crystal Structure Database) maintained by the FIZ Karlsruhe.

2.1.2 XRD Experiments

In situ X-ray powder diffraction experiments were performed using a STOE Bragg-Brentano diffractometer (Cu K_α radiation, secondary monochromator, scintillation counter). The experiments were carried out in an in situ cell (Bühler, HDK S1, total volume = 400 ml). 25 mg of the catalyst were ground, sieved (200 mesh) and applied to the sample holder (resistively heated stainless steel band) in slurry with acetone. The in-situ experiments were performed in different atmospheres controlled by *Bronkhorst* mass flow controllers (total flow 160 ml/min). Reduction of the calcined CuO/ZnO precursors was carried out in 2 vol-% H_2 in helium in a temperature range from 300 K - 523 K (heating ramp of 6 K/min). XRD patterns were recorded at 523 K in reducing atmosphere and under methanol steam reforming conditions in a range from 28.0° to 93.0° 2θ with a step width of 0.04° 2θ (counting time: 2 s/dp). Changes in gas phase composition were analyzed on line with a mass spectrometer

(Omnistar Pfeiffer).

Calcination of the washed and dried Cu,Zn hydroxycarbonate precursors was carried out in a STOE Theta-Theta diffractometer (Cu K_α radiation) connected with a mass spectrometer to analyze the gas phase. The diffractometer was equipped with a XRK 900 high temperature cell for in situ measurements. 50 mg of the precursors were ground and sieved and placed on the sample holder. Calcination was carried out in 80% He and 20% O_2 (total flow = 100 ml/min) in a temperature range from 300 K to 873 K. In-situ XRD patterns were recorded in 20°C steps (average heating ramp: 3.5 K/min) in a range from 37.0°- 40.0° 2θ with a step width of 0.06 2θ (counting time: 2 s/dp) and in 50°C steps (average heating ramp: 2 K/min) in a range from 30° - 45° 2θ (step width = 0.04 2θ; counting time = 2 s/dp).

Ex-situ XRD patterns of freshly reduced catalysts were measured in transmission mode at a STOE Stadi-P diffractometer in Debye-Scherrer geometry (Cu K_α radiation, linear position sensitive detector). The catalysts were reduced in 2% H_2 diluted in He at 523 K in a glass reactor. The reduced sample was transferred in a glass capillary. The sample preparation was conducted in a glove box to prevent exposure of the reduced Cu/ZnO catalysts to air. XRD patterns of the freshly reduced catalysts were recorded in a range from 28° to 105° 2θ (step width = 0.5 2θ, counting time 450 s/step). Additionally, ex-situ XRD patterns were monitored for non-activated CuO/ZnO catalysts in a range of 28° - 78° 2θ (step width = 0.5 2θ, counting time 650 s/step).

2.2 X-ray absorption (XAS)

X-ray absorption spectroscopy (XAS) is an element specific method providing information about the local structure such as coordination geometry, average valence, and structural disorder. Thus, in-situ XAS is a complementary technique compared to XRD, enabling to investigate the local geometry of a catalyst under working conditions.

2.2.1 Theory

A schematic view of the electronic transition by atomic absorption of an X-ray photon is depicted in Figure 2. X-ray absorption spectroscopy is based on the transition of an electron from a core state to an empty state above the Fermi level E_f induced by the absorption of a

photon. To excite an electron, the photon energy $h\upsilon$ has to be larger than the energy of the core level E_0. The photo electron leaves the core level with a kinetic energy $E_k = h\upsilon - E_0$. If an X-ray has sufficient energy to excite a core level, the resultant photoelectron will excite into unoccupied states. For higher kinetic energies of the photoelectron scattering at neighboring atoms occur.

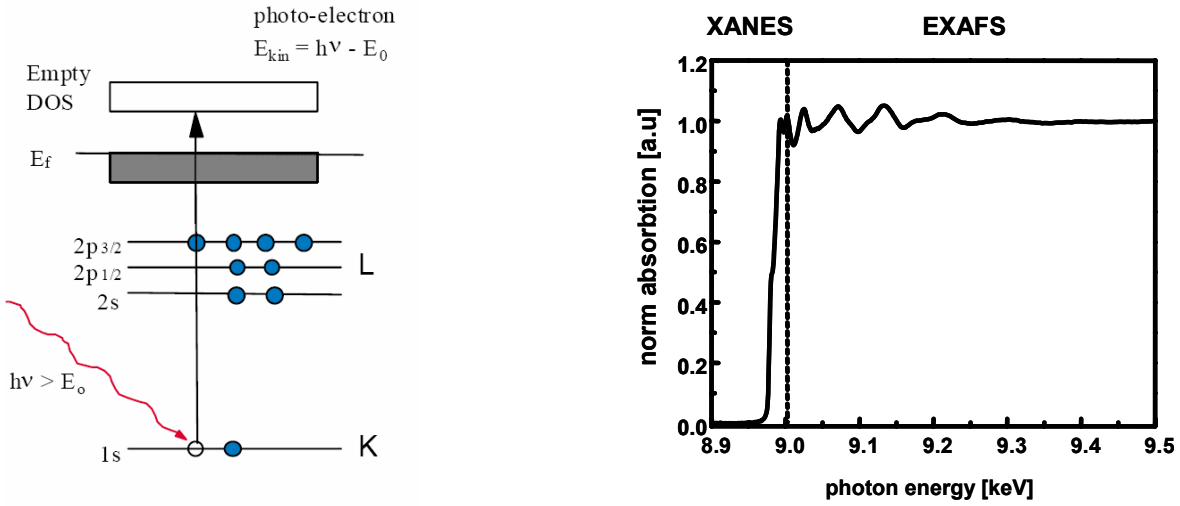

Figure 2 Electronic transition of an electron from a 1s core level induced by a X-Ray photon (a) and example for a XAS spectrum (Cu K-edge: 8.970 keV) (b)

X-ray absorption spectra are commonly separated in two regions: The X-ray absorption near edge structure (XANES) and the extended X-ray absorption fine structure (EXAFS). The XANES region is dominated by the local atomic resonance and multiple scattering at neighboring atoms (~ 50 eV above the core level energie). The EXAFS region is determined by single and multiple scattering events at neighboring atoms.

XANES:

The intensity of an attenuated X-ray beam by a sample I is defined by the intensity of the beam before the sample I_0, the length of the sample d and the absorption cross section μ (Figure 3). Thus, the height of the absorption edge is a function of the length of the sample and the absorption cross section, which depend on the mass of the sample and the element specific mass absorption coefficient. XANES spectra are labeled by the energy levels of the electron in the core state, e.g. 1s (K-edge), 2s (L_3-edge), $2p_{1/2}$ and $2p_{3/2}$ (L_2 and L_3-edge). The energy of the absorption edge is determined by the binding energy of a core hole

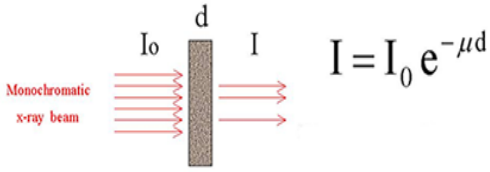

Figure 3 Absorption by a uniform sample

E_0. Shifts in E_0 are related to changes in the average valence of an absorbing atom. The XANES shape is determined by electronic transition and multiple scattering at neighboring atoms and gives information about the oxidation state, the density of state, and the local geometry.

EXAFS:

If the energy of the incident photon *hv* is larger than the energy of the core level E_0 the excessive energy is stored as in kinetic energy of the photo-electron E_K. In that case the exited photo electron can be described as spherical electronic wave which can be scattered by the neighboring atoms, producing a backscattered wave (Figure 4). The outgoing wave of the absorber atom and the backscattered wave of the neighbor atoms interfere constructive or destructive. The resulting interference pattern depends on the energy of the ejected electron (i.e. the wavelength of the outgoing wave) and the distances between the absorber and the neighboring atom. Thus, a continuous increase of the energy of the incident photon results in variation of the total absorption (minima and maxima) due to variation in the interference pattern, the so-called EXAFS region. In addition to single scattering (i.e. the outgoing wave scatters backwards only once from a neighboring atom) multiple scattering (i.e. scattering from one neighbor to the next before combining with the unscattered wave) contributes to the interference pattern (Figure 4). The EXAFS fine structure (i.e. interference pattern) strongly depends on the distance between the absorbing atom and the backscattering atom and the number of neighboring atoms. Furthermore, if there is disorder induced by structural defects or thermal oscillation, the positions of the neighboring atoms will not be exactly defined and different interference patterns will be generated. Simulation of experimental EXAFS spectra can be used to obtain the distances (R) between the absorber and backscatters, the coordination number of the absorber atom (CN) and the disorder, characterized by the Debye Waller factor (DWF).

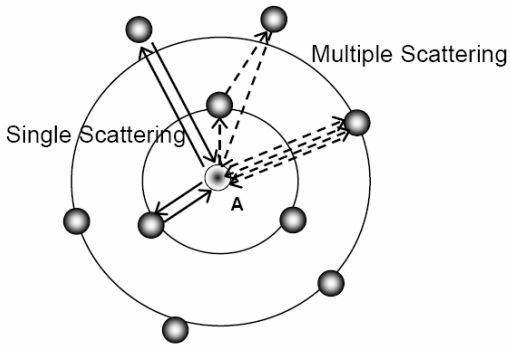

Figure 4 Scattering paths of an absorbing atom A on surrounding neighbors

The theoretical relation between the EXAFS function (χ(k)) and the structural parameters is given by Sayers et al. [46]:

$$\chi(k) = \sum_j S_o^2 N_j \frac{|f_j(k)|}{kR_j^2} \sin(2kR_j + 2\delta_c + \Theta_j) e^{\frac{2Rj}{\lambda(k)}} e^{2\sigma_j^2 k^2} \quad \textbf{(2-7)}$$

The structural parameters are the mean distance between the absorber and the atom in the j_{th} shell R_j, the number of atoms in the j_{th} shell N_j and the temperature dependent fluctuation of the atomic distances including effects by structural disorder (Debye-Waller-Factor) σ_j. Further parameters are the amplitude reduction factor S_0, the magnitude of the backscattering amplitude of the j_{th} neighbour $|f_j(k)|$, the phase shift on the absorbing atom δ_c, the phase shift of the backscattering atom Θ_j, and the mean free path of the photoelectron $\lambda(k)$. The Fourier transformed χ(k) correspond to a radial distribution function (RDF) with slightly phase shifted maxima (~ 0.4 Å) at distances of the nearest neighbors. The EXAFS equation (2-7) enables to analyze experimental data to obtain structural information such as distances, number of atoms around a particular atomic species and disorder. Theoretical backscattering phases and amplitudes can be calculated using the *ab inito* code FEFF [47] and enable to simulate experimental spectra by refining the distances, coordination number, and the Debye-Waller-factor. In summary, EXAFS provides information about the number and type of neighboring atoms, the distances, and structural disorder.

2.2.2 XAS Experiments and data analysis

In situ XAS experiments were performed in a flow reactor in transmission geometry (designed by M. Hagelstein, T. Neisius et al. ESRF, in collaboration with FHI) at the Cu K-edge (E= 8.979 keV) and Zn K-edge (E=9.659 keV) at the Hamburger Synchrotron Radiation Laboratory (HASYLAB, beamline E4 and X1). The CuO/ZnO precursor was diluted in boron nitride (ratio CuO/ZnO : BN = 1:10) and pressed for 1 min at 1.5 t into a pellet of 5 mm in diameter. Reduction of the precursor was performed in 2 vol-% H_2 in He (1 bar, total flow 40 ml/min) in a temperature range from 303 K to 523 K with a heating ramp of 6 K/min. Time resolved XANES (X-ray absorption near edge structure) measurements at the copper K edge (time resolution = 100 s/spectrum; energy range 8.9 to 9.2 keV) enabled to determine phase transition and kinetics during reduction. The number of reference spectra required to simulate a set of experimental XANES spectra was obtained by a principle component analysis (PCA)

[48,49] implemented in WinXAS 3.2. The fraction of the reference spectra in each single XANES spectrum was determined by a least-square fit of a linear combination of the reference spectra to the experimental spectrum.

After reduction of the CuO/ZnO precursor, the extended X–ray absorption fine structure (EXAFS) of the resulting Cu/ZnO catalyst was monitored under methanol steam reforming conditions at 523 K (ratio $CH_3OH:H_2O$ = 1:1 ; ~2.5 vol-% CH_3OH / 2.5 vol-% H_2O / 95 vol-% He; total flow 40ml/min). Copper foil was used as reference for energy calibration, two polynomials were used for background subtraction and normalization, and an atomic background in the EXAFS region was determined by cubic splines. The radial distribution function was obtained by Fourier transformation of the k^3 weighted experimental spectrum $\chi(k)$ (k range from 2.3 $Å^{-1}$ to 11.5 $Å^{-1}$ for Cu K-edge; from 2.3 $Å^{-1}$ to 10.5 $Å^{-1}$ for Zn K-edge) in the R space. The multiple and single scattering paths in an fcc bulk Cu, hexagonal ZnO and monoclinic CuO model structures were calculated using FEFF 8 [47] in an R range from 1.5 Å to 6.0 Å for copper, from 1.9 Å to 3.6 Å for ZnO, from 1.9 Å to 3.2 Å for CuO (5 % lower limit with respect to the strongest scattering path). Refinement of the Cu, CuO and ZnO model structure to the experimental EXAFS spectrum was carried out in R space. The structural parameters refined are the single scattering shell distances (R), the Debye Waller factors of the single scattering paths (σ^2), and one E_0 shift for all scattering paths. The coordination numbers (CN) were kept constant because of the rather large Cu, CuO and ZnO crystallite sizes (> 70 Å).

Additionally, EXAFS spectra at the Zn K-edge were monitored under isothermal reduction conditions. Therefore, catalyst pellets (BN:Cat ratio 10:1) were heated up in He from 303 K to 523 K (heating ramp 6 K/min) followed by introduction of 2% vol-% hydrogen in the gas mixture at 523 K. Changes in the structure of Zn containing solids under isothermal reduction conditions were investigated by measuring Zn K-edge EXAFS every 4 min. Zn foil was used as reference for energy calibration, background subtraction and atomic background determination was done as described above. Fourier transformation of the experimental $\chi(k)$ was done in a k range from 2.0 $Å^{-1}$ to 9.5 $Å^{-1}$.

2.3 Nuclear Spin Resonance (NMR)

2.3.1 Theory

Nuclear magnetic resonance (NMR) spectroscopy probes molecules or crystals by recording

the interaction of radiofrequency electromagnetic radiation with the nuclei placed in a strong magnetic field. The method is based on the "Zeeman Effect", which describes the behavior of certain nuclei exposed to a strong magnetic field. If a magnetic field is present, the atom energy levels split into a larger number of levels with different energies given by the *magnetic quantum number m*. The population of these levels is given by the Boltzmann equation, which means that the lower energy level contains more nuclei than the higher energy level. The lower the temperature the higher the population of the lower energy level. A nucleus of a lower energy level can be exited in a higher one if the frequency of electromagnetic radiation (i.e. the corresponding energy) matches with the energy difference between the two energy levels (resonance). After Fourier transformation NMR spectroscopy gives a spectrum of the resonance signals of nuclear spins as function of the frequency of electromagnetic radiation.

The excitation of the nuclei results in equal populations of the lower and higher energy levels and no further excitation occurs. The spin system is saturated. Thus relaxation processes have to occur which return nuclei from higher to lower energy states in order to enable continuous excitation. There are two major relaxation processes. *Spin-Lattice* and *Spin-Spin* relaxation. Spin-Lattice relaxation describes the interaction of the nucleus with the surrounding lattice. The motion of the nuclei creates a complex macroscopic magnetic field, the so called lattice field. The lattice field can interact with the nuclei in the exited state and cause a relaxation of the nuclei in the lower energy level. The loss in energy increases the amount of nuclei motion in lattice and results in an increase in temperature. Spin-Spin relaxation describes the interaction between neighboring nuclei with different magnetic quantum states. A nucleus in the lower energy level will be excited, while the exited nucleus relaxes to the lower energy state. This exchange of quantum states results in a decrease of the average lifetime of the nucleus in the exited state.

The line width of an NMR signal is inverse proportional to the Spin-Spin relaxation time. The quicker the relaxation the broader is the NMR signals. Spin-Spin relaxation is dominated by dipole-dipole interaction between spatially neighboring nuclear spins, the quadrupole moments (for nuclei with spin $I > 1$; e.g. Cu $I = 3/2$) and the electrical field gradient at the site of the nucleus. In solid-states the neighboring nuclei are near each other and effect the spin-spin relaxation much more than in liquids. The resulting quick relaxation times lead to broad solid-state NMR lines. Rapid sample rotation around an axis in the magic angle of 54° (MAS: magic angular spinning) helps to average out or at least reduce the anisotropic solid state interactions (e.g. dipole-dipole interaction, anisotropies in chemical shifts, quadrupole

interaction). CuO and Cu_2O reveal an asymmetric local surrounding and can only be detected by using the MAS-NMR technique. Controversially, copper metal is more symmetric in the local surrounding and can thus be measured under static conditions using a Spin-Echo puls (90°-tau-180°) technique. More details about Spin-Echo NMR are given elswehre [50]. Thus, the NMR method used to investigate the reduced catalysts is Cu metal sensitive.

2.3.2 NMR Experiments

Cu NMR investigations were performed at the Max-Planck Institute of Chemical Physics of Solids in Dresden by A. Rabis. After reduction of the copper oxides in 2% hydrogen diluted in He, ^{63}Cu- and ^{65}Cu-NMR spectra of the Cu/ZnO catalysts were measured with a Bruker MSL 300 spectrometer at 79.618 MHz for ^{63}Cu and 85.288 MHz for ^{65}Cu at 4.2 K in an Oxford cryostat. Spin-echo experiments (90°-tau-180°) were performed with a 90° pulse of 5.5 μs, a ”recycling delay” of 2 s and a tau value of 25 μs. The spectra shown are calibrated against $CuBr_{(s)}$ at - 381 ppm. The results obtained for ^{65}Cu correspond to those for ^{63}Cu. The NMR investigations were done to analyze the particle size and microstrain of the copper metal.

2.4 Ultraviolet/Visible Spectroscopy (UV-Vis)

UV-Vis spectroscopy is based on the excitation of an electron from a lower to a higher atomic or molecular energy level induced by irradiation of ultraviolet with (UV) and/or visible (Vis) electromagnetic radiation. Three types of electron transfer processes can be distinguished: the π-π* and n-π* electronic transitions, d-d excitations and charge transfer transitions. The excitation from a non-bonding electron into an anti-boning molecular π orbital (n-π*) as well as the excitation from a bonding in anti-bonding π orbital (π-π*) are mainly observed in covalent inorganic or organic molecules. In charge transfer (CT) excitation processes a large fraction of an electronic density is transferred from one region of a molecular entity, called the electron donor, to another called the electron acceptor. Ligand to metal charge transfer (LMCT) transitions occur in ligands with a lone electron pair of high energy and metals with low unoccupied energy levels (i.e. high oxidation state; transition metals with partially filled d orbitals). In contrast, metal to ligand charge transfer (MLCT) transition takes place by the interaction of low energy and unoccupied π* ligand orbitals with oxidisable metals (low

oxidation state). The intervalence charge transfer (IVCT) transition describes the electron transfer (thermally or photoinduced) between two metal sites differing only in oxidation state. Quite often such electron transfer reverses the oxidation states of the sites. The term is frequently extended to the case of metal-to-metal charge transfer (MMCT) between non-equivalent metal centers.

The d-d excitation can be described by the crystal field theory. The crystal field theory is based on the strictly ionic character of the central atom and the ligands; covalent bonding is completely neglected. When the metal is surrounded by ligands arranged in a particular geometry with respect to the metal centre, splitting or separation of energy levels of the five degenerated d orbitals in a transition metal occurs (crystal field splitting). The electron occupation of the degenerated d orbitals depends on the oxidation state of the transition metal atom. Electron transfer from occupied d orbitals in unoccupied d orbitals is called d-d transition. The number of d-d transitions strongly depends on the electronic configuration, which is determined by the arrangement and nature of the ligands with respect to the central atom (e.g octahedral, tetrahedral or planar geometry).

Finally, in metal nano particles smaller than the wavelength of the irradiated light, collective electronic oscillation – the so called *Mie-plasmons* – can be exited by light (collective excitations of conduction electrons) and results in pronounced resonance in the visible or UV range of the spectrum.

UV-Vis measurements of liquids and gas phases usually take place in the transmission geometry where the absorption is determined by the intensity ratio of an incident light I_0 to the transmitted light I (Lambert-Beer Law). Since it is difficult to obtain transparent solids or powders, UV-Vis spectroscopy of solids usually takes place in the reflectance mode. The reflected beam of a sample consists of two components: *Specular and Diffuse reflectance*. The reflection of a light beam by a surface under the same angle as that of the incident beam is called specular reflectance. Diffuse reflection involves photons which adsorb into the solid and are multiply scattered in all directions. Diffuse reflectance provides information of the oxidation state and the coordination geometry of a transition metal and thus is the more valuable component to be measures absorption. To collect diffuse reflected light, integration spheres are used in UV-Vis spectrometers. The absorbance $F(R_\infty)$ using diffuse reflectance spectroscopy (DRS) can be calculated by the Kubelka-Munk equation,

$$F(R_\infty) = \frac{(1 - R_\infty)^2}{2R_\infty} \qquad \textbf{(2-8)}$$

with the diffuse reflectance of an infinitely thick layer R_∞. The Reflectance of a spectrum R is calculated by the reflectance of the sample R_λ vs. the reflectance of a non absorbing reference S_λ ("white standard") and a background reflection of surrounding light D_λ:

$$\%R = \left(\frac{S_\lambda - D_\lambda}{R_\lambda - D_\lambda} \right) \cdot 100 \qquad \textbf{(2-9)}$$

In this work UV-Vis reflectance spectroscopy was performed with an optical fiber equipment. An optical fiber consist of synthetic fused silicaglas (amorphous silicon dioxide) as light guidance, a cladding (fluorine doped fused silica) where the transported light is internally reflected and a buffer to protect the fiber (e.g gold for high temperature resistance or polyimide for lower temperatures). The basic principle of light transportation through an optical fiber is a multiplicity of internal total reflections on the cladding of the light guidance. Total internal reflection requires a smaller refractive index of the cladding n_2 compared to the light guidance n_1 (Fig.5).

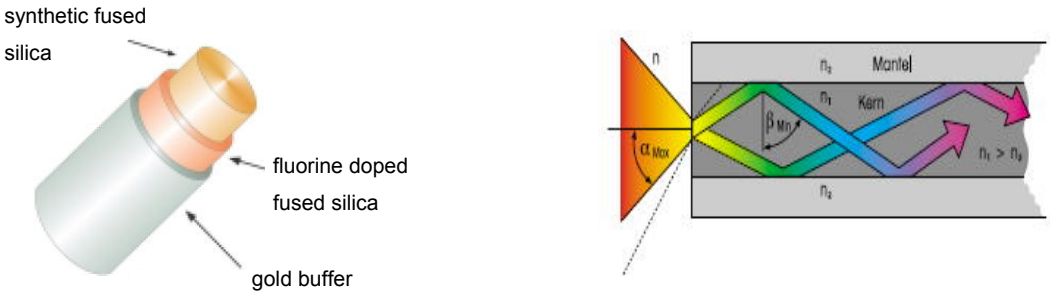

Figure 5 Fiber optic design and principle of light transportation

The fiber optics used consists of 18 (illumination) light guidance around 1 (detection) light guidance. The 18 illumination fibers are tilted in an angle of 45° relative to the detection fiber in order to avoid collection of specular reflectance. The Fiber is connected to the spectrometer. A schematic drawing of the spectrometer is depicted in Figure 6. The light from the fiber enters the spectrometer (1), passes trough an installed slit (2) which acts as an entrance aperture and determines the amount of light entering the optical bench. The light is collected by the collimating mirror (4) reflecting the light as a collimated beam to the grating (5) which decomposes the collimated light in

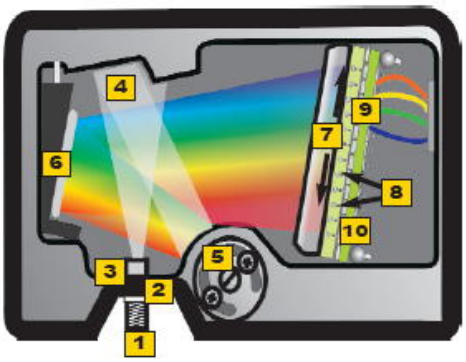

Figure 6 schematic draw of the UV-Vis spectrometer

spectral light (prisma) and furthermore determines the spectral range possible to measure. After the light passes the grating, it is reflected from a focusing mirror (6) to a cylindrical collecting lens (7) which increases the light-collection efficiency and is finally detected by a CCD array (10). The pixel number of the CCD array (2048), the grating (300 lines mm^{-1}) and the width of the slit (5 μm) determines the spectral range (200-1100 nm) and the resolution of the spectrometer (0.7 nm). A detailed description of the experimental conditions is given in the corresponding chapter (3.1; 4.2).

2.5 Additional methods

2.5.1 Transmission electron microscopy (TEM)

Transmission electron microscopy (TEM) probes a thin sample with an electron beam. The penetration depth of the beam depends on the thickness and density of the sample and the energy of the incident electron beam. For a thin sample (a few nm) and a high energy electron beam (100 keV to a few MeV) the incident electron beam passes trough the sample accompanied by an energy intensity loss of the electron beam due to elastic scattering (i.e. diffraction). Elastic scattering of electrons by atoms of the sample refract the primary electron beam. Thus, the primary beam loses intensity on passing trough the sample while the intensity of the diffracted beam increases. The number of diffracted electrons depends on the crystal orientation, the structure, the chemical composition, and structural defects of the sample. Both, the intensity of the diffracted and transmitted beam are used for projection of the sample and to obtain structural information. TEM was performed on a Phillips CM 200 FEG TEM. The reduced Cu/ZnO catalysts were deposited on holey-carbon films supported on gold grids. The sample preparation was conducted in a glove box to prevent exposure of the reduced Cu/ZnO catalysts to air.

2.5.2 Thermogravimetry (TG-MS)

Thermogravimetric analyses were conducted on a NETSCH STA 499 C in a constant gas flow of 100 ml/min of 2 vol-% H_2 in helium. Approximately 15 mg of the calcined precursors were heated in an Al_2O_3 crucible to 523 K with a heating rate of 6 K/min. Evolution of gas

phase during reduction was monitored with a quadropole mass spectrometer (Pfeiffer QMS200 Omnistar).

2.5.3 Activity measurements and surface area determination (RFC)

Activation of the CuO/ZnO precursors was performed in 2 vol-% H_2 in the temperature range between 300 K and 523 K at a heating rate of 6 K/min followed by an isothermal period of 30 min at 523 K. For in situ XRD and in situ XAS experiments, the four Cu/ZnO samples obtained from the differently aged precursors were cooled down to 298 K after reduction and exposed to the steam reforming gas mixture at atmospheric pressure using saturators for methanol and water (ratio CH_3OH:H_2O = 1:1 ; ~2.5 vol-% CH_3OH / 2.5 vol-% H_2O / 95 vol-% He). A total flow of 160 ml/min in the in situ XRD cell and 40 ml/min in the in situ XAS cell was employed. The temperature was increased from 298 K to 523 K with a heating rate of 6 K/min. Gas phase evolution of products and reactants was monitored with a mass spectrometer (Omnistar, Pfeiffer). 13 mg of the catalyst sample were used for the XRD experiments, while 3 mg catalyst diluted in 30 mg BN were used for the XAS experiments. The methanol steam reforming activity determined by the hydrogen production rate was calculated under isothermal conditions (523 K) after a steady state in catalytic activity was reached. All Cu/ZnO catalysts studied exhibited a rapid decrease in catalytic activity in a time period of 10 min to approximately 5% of the maximum value, whereas only slight changes in activity were recorded after the activity decrease. The catalytic activity was determined after a time period of 30 min.

Catalytic activity obtained from the in situ experiments was compared to activity measurements of the catalyst in a tubular stainless steel reactor placed in an aluminium-heating block. For these measurements, the catalyst powder was diluted with BN and pressed in pellets. Subsequently, the pellets were ground and sieved to obtain a defined particle size (20-25 Mesh). The methanol conversion of the four catalysts obtained from differently aged precursors was determined at 523 K by using a Varian GC 3800. The measurements were performed at the Technical University Berlin by Herry Purnama. More details are given elsewhere. [12]

The specific copper surface area was determined by surface titration with N_2O (reactive frontal chromatography (RFC), $N_2O + 2Cu_s \rightarrow N_2 + Cu_s\text{-}O\text{-}Cu_s$) [20, 21] (T = 313 K, 0.5 vol-% N_2O in Helium, 50 mg catalyst diluted in 50 mg BN, Cu surface atom density: $1{,}47 \times 10^{19}$

m^{-2} [51]). Prior to the surface area determination the sample was purged for 30 min in He with a flow of 50 ml/min to diminish the amount of adsorbed molecules followed by reduction in 2 vol% H_2 at 523 K according to the procedure described above.

2.5.4 X-ray photon electron spectroscopy (XPS)

X-ray photon electron spectroscopy (XPS) provides information on the chemical state and the chemical composition of the elements on the surface of a catalyst. The technique is based on the emission of a near-surface core ore valence electron into the continuum (above the Fermi level) induced by an X-ray photon (photoelectric effect). The kinetic energy of the emitted photoelectron E_k correlates linearly with the frequency υ of the incident beam;

$$E_k = h\nu - E_B - \phi \qquad \textbf{(2-10)}$$

with the energy of the X-ray quantum $h\upsilon$, the binding energy of the core level E_B and the work function of the spectrometer Φ. The binding energy of the core level enables to identify the chemical composition of the sample at the surface as well as differences in the oxidation state and molecular environments of identified elements. Furthermore, XPS using synchrotron radiation enables to determine a depth distribution of the different elements down to a surface depth of a few nanometers. Depth profile investigations require the ability to tune the photon energy which is only possible with synchrotron radiation. Depth profiling is based on the properties of photoelectrons generated during an XPS experiment that can only travel a limited distance within a solid before losing energy due to inelastic collision. The ability of a photoelectron to travel through a layer of the thickness L of a solid without losing energy is given by const*$e^{-L/\lambda}$, with the inelastic mean free path λ. Since the inelastic mean free path is a function of the kinetic energy of the photoelectrons it is possible to determine a depth profile by tuning the excitation photon energy. In contrast to the previously explained EXAFS spectroscopy, near edge X-ray absorption fine structure spectroscopy in the soft X-ray range (NEXAFS) can be applied by measuring the electron yield as function of the kinetic energy of the photoelectron. For kinetic energies form 100 to 1000 eV the penetration depth rises from 2 to 6 monolayers, from 3000 eV to 7000 eV the depth rises from 11 to 17 monolayers. Thus, NEXAFS is a near-surface sensitive bulk analysis method. XPS instruments basically consist of an X-ray source, an electron energy analyzer and an electron detector. XPS spectra are recorded by measuring the kinetic energy of the emitted electrons.

A catalyst pellet of 80 mg (13 mm diameter, 1.5 t surface pressure) is placed on a stainless steel plate and covered with a stainless steel cap (5 mm hole). The steel plate can be heated up with a NIR-Laser. Temperature measurement takes place on top of the sample pellet. Reduction of the precursor was performed in 0.5 mbar H_2 in a temperature range from 303 K to 523 K with a heating rate of 5 K/min. The XPS and NEXAFS spectra were measured under isothermal conditions (523K) after reduction. Steam reforming activity of the catalysts was measured in 0.125 mbar H_2O and 0.125 mbar CH_3OH. Gas phase evolution was analyzed using a mass spectrometer. Zn-L_3 and Cu-L_3 NEXFAS spectra were recorded at RT in the non-reduced and at 523 K in the reduced state. The depth profile of the Cu 3p and Zn 3p core levels in the non-reduced and reduced state as well as the C 1s XPS spectra (activated and non-activated) were recorded.

2.6 Preparation

Copper zinc hydroxycarbonate precursors of the Cu/ZnO catalysts (molar ratio of copper to zinc is 70:30) were prepared by co-precipitation. Precipitation was carried out in a reaction container filled with 400 ml bidistilled water (353 K) by simultaneous mixing of an aqueous solution of metal nitrates ($Cu(NO_3)_2$*3 H_2O and $Zn(NO_3)_2$*6 H_2O; 600ml of a 1M concentrated metal nitrate solution) with sodium carbonate (1.2 M) at constant pH (pH 7). The resulting precipitates were aged under continuous stirring in the mother liquor at 353 K for 0 min, 15 min, 30 min, and 120 min. After filtering, 20 g of the undried precursors were washed six times with deionized water (80 ml) in a 250 ml beaker for 10 min under continuous stirring at 333 K. Finally, three Al_2O_3 boats each filled with 1g of the samples were dried at 393 K for 10 h in static air followed by calcination at 603 K in static air for 3 h (heating rate = 6 K/min). More details about the experimental set up and the preparation conditions used, as well as the resulting precursor phases are described in reference [17].

3 Development of a combined In-Situ UV-Vis/XAS cell

A detailed knowledge of the relation between bulk structure, surface structure, electronic structure, and catalytic activity is necessary to understand the functionality of a catalyst. The combination of well developed in-situ techniques (e.g. XAS, XRD) with other techniques (e.g. UV-Vis, Raman) adds complementary information and enables a better understanding of the relation between catalyst and activity. The combination of in-situ XAS, UV-Vis spectroscopy and mass spectrometry (MS) allows investigating simultaneously the geometric structure, electronic structure and activity of the catalyst. XAS provides information of the local structure and the electronic state of a specific element, whereas UV-Vis provides information on electronic transitions between atomic or molecular orbitals and can indicate valence and coordination. The combination of both techniques complements element specific information (XAS) by measuring the complete catalyst system including support and adsorbate. Combined XAS/UV-Vis spectroscopy of metal clusters provides information of the electronic structure in the near surface region and the geometric structure of the bulk metal. Furthermore, the time resolution of the fiber optic UV-Vis system (10 ms) compared to XAS spectroscopy enables to measure rapid structural and electronic changes of the catalyst under working conditions. The following chapter is focused on the development of an in-situ cell for simultaneous time resolved measurement of X-ray absorption and UV-Vis spectra.

3.1 Experimental Set-Up

A schematic drawing of the new combined UV-Vis/XAS cell is depicted in Figure 7. The new cell is related to the design of an in-situ XAS cell for time resolved measurements [52]. The cell consist of a reactor tube (10.2 mm ∅) with a small gas volume (~10 ml) for rapid gas phase response, and is sealed by aluminum or “Kapton” windows to contain the gas phase. XAS experiments were performed in transmission geometry with a 10 mm sample pellet tilted in an angle of 45° to the X-ray beam and held by a sample holder. The sample holder is fixed by a high temperature spring which presses the sample holder on an aperture plate in the centre of the reactor. The UV-Vis spectrum is measured in diffuse reflectance mode using a fiberguide high temperature optical fiber bundle (gold coated). The UV-Vis light irradiates the sample pellet in an angle of 90°. The fiber bundle is connected to an Ocean optics

DH2000 light source equipped with a deuterium (UV) and thungsten lamp (Vis) to illuminate the sample. The reflected light returns through the fiber bundle to an Ocean Optics HR2000CG-UV-NIR spectrometer, which is connected to a Laptop to record the spectrum with the Ocean Optics OOIBase 32 software.

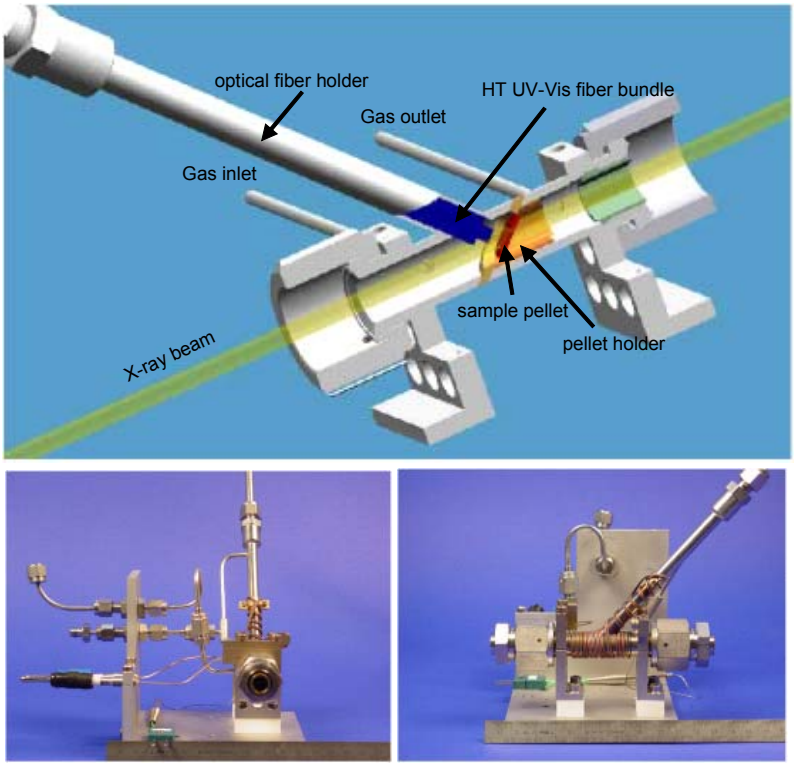

Figure 7 Schematic draw of a combined in situ XAS and UV-Vis cell

The cell and half of the optical fiber holder is wrapped with a coaxial heating wire (1.30 m) which uniformly heats the cell to a maximum temperature of 600°C (maximum operation voltage = 80 V) and allows quick heating and cooling. The cell temperature is measured in the cell wall (aperture plate) and controlled by a Eurotherm PID controller. The UV-Vis cell temperature calibration at 6 K/min is depicted in Figure 8. The sample temperature deviates about 2 °C at a cell temperature of 100 °C and about 7 °C at 600 °C cell temperature. Gas phase composition is measured with a Pfeiffer Omnistar quadropole mass spectrometer. The experiments were performed at 1bar.

UV-Vis spectra were recorded every 10 seconds in a range of 200 nm to 1100 nm (integration time: 1000ms; average: 10; boxcar (smoothing): 15). Hexagonal boron nitride (99.5%-Alfa Aesar) was used as diffuse reflectance standard ("white standard") to define the maximum reflection (100 %). Boron nitride reflects well in a range of 320 nm to 1000 nm, but reveals a

strong absorption band in the UV range at 270 nm. The maximum catalyst concentration in the pellet to measure a transmission X-ray absorption spectrum is limited by the element specific absorption coefficient. The resulting catalyst concentration in a BN diluted pellet (total mass 100 mg) is sufficient for XAS experiments but insufficient for the more surface sensitive UV-Vis spectroscopy. For combined UV-Vis/XAS experiments a "double layer pellet" was prepared. The top layer consist of a mixture of BN and catalyst powder (ratio 2:1) supported by a layer of born nitride (total mass 100 mg).

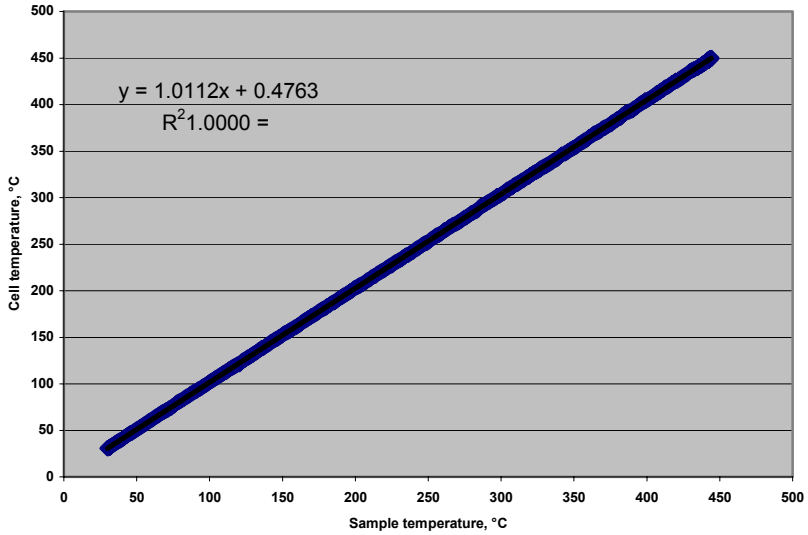

Figure 8 UV-Vis cell temperature calibration at 6K/min

3.2 Cell characteristics

The distance between the tip of the optical fiber bundle and the pellet surface determines the irradiated area on the pellet and the number of counts collected by the detection fiber (intensity). Slight changes in the fiber distance to the pellet due to mechanical expansion of the cell during temperature programmed experiments may result in continous changes of the spectrum. Temperature programmed experiments in a He flow at 6 K/min using $BaSO_4$ as reflectance standard were performed to investigate the effect of thermal expansion on the UV-Vis spectra. Increasing temperature does not affect the intensity of the spectra in a range of 250 nm to 600 nm, but a slight linear decrease in reflectance was observed in a range of 600 nm to 1100 nm. Similar linear trends at higher wavelength as function of the temperature were observed by heating experiments in inert atmosphere using Cu/ZnO and boron nitride. Thus, slight linear changes in the intensity of UV-Vis spectra have to be taken into account for the interpretation of temperature programmed experiments.

Boron nitride UV-Vis reflectance spectra (counts) measured at different angles relative to the surface are depicted in Figure 10. The peaks at 480 nm, 580 nm and 660 nm are due to D_α (3s→2s emission), Fulcher and D_β lines (2p→2s emission) of the Deuterium bulb and are subtracted from the experimental spectrum by the reference standard (BN). The intensity of the D_α line at 480 nm was used to investigate chemical or physical changes of BN during temperature programmed experiments. In Figure 9 the intensity changes in the UV-Vis spectra of an untreated BN pellet during heat treatment in He to 773 K (BN 1st cycle) followed by an additional heat up cycle (BN 2nd cycle) was recorded. The intensity of the BN reflectance spectrum increases significantly up to a temperature of 523 K and remains roughly constant above 523 K, whereas only slight intensity changes were observed for a repeating heat up cycle with the same sample. In contrast, only slight changes were observed for the pre-tempered BN sample (tempered at 573 K for 3h). The result clearly indicates that temperature induced segregation of impurities and inclusions of commercial available boron nitride result in modified reflectance properties. Thermal pre-treatment of BN is thus necessary to avoid temperature induced changes in the reflectance spectra caused by the diluent boron nitride.

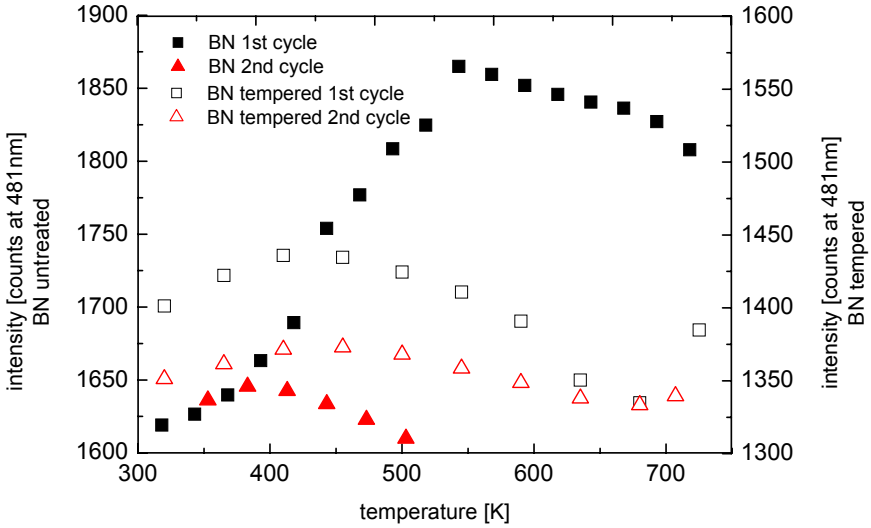

Figure 9 Intensity of diffuse reflectance UV-Vis spectra as function of temperature for a untreated and pre-tempered BN sample

The major advantage of using BN as diluent for XAS experiments is the low absorption of X-ray radiation, the thermal stability, the inert character in catalytic reactions and the mechanical softness which enables to grind a catalyst mixture and to press pellets. The disadvantage of using BN for a combined XAS/UV-Vis experiment is the absorption band in the UV range and the sensitivity of the material to temperature programmed measurements

(Figure 9). For a more UV-Vis sensitive combined XAS experiment alternative diluents should be used. However, well-known diffuse reflectance standards such as $BaSO_4$, MgO or Teflon (Polytetrafluorethylen) and alternative white standards such as boron carbides or cubic boron nitride exhibit major disadvantages. $BaSO_4$ and MgO are inappropriate because their high X-ray absorption coefficient. Teflon cannot be used because of the thermal instability above 573 K. Boron carbide or cubic boron nitride are difficult to handle due to their mechanical hardness. Thus, hexagonal BN was used in this work for the combined XAS/UV-Vis experiments.

The effect of the light irradiation angle relative to the surface was investigated using boron nitride as reflection standard. The normalized intensity for different wavelength (300 nm to 900 nm) as a function of the irradiation angle is compared to a pellet and powder surface (Figure 10) in order to investigate the influence of macroscopic surface properties.

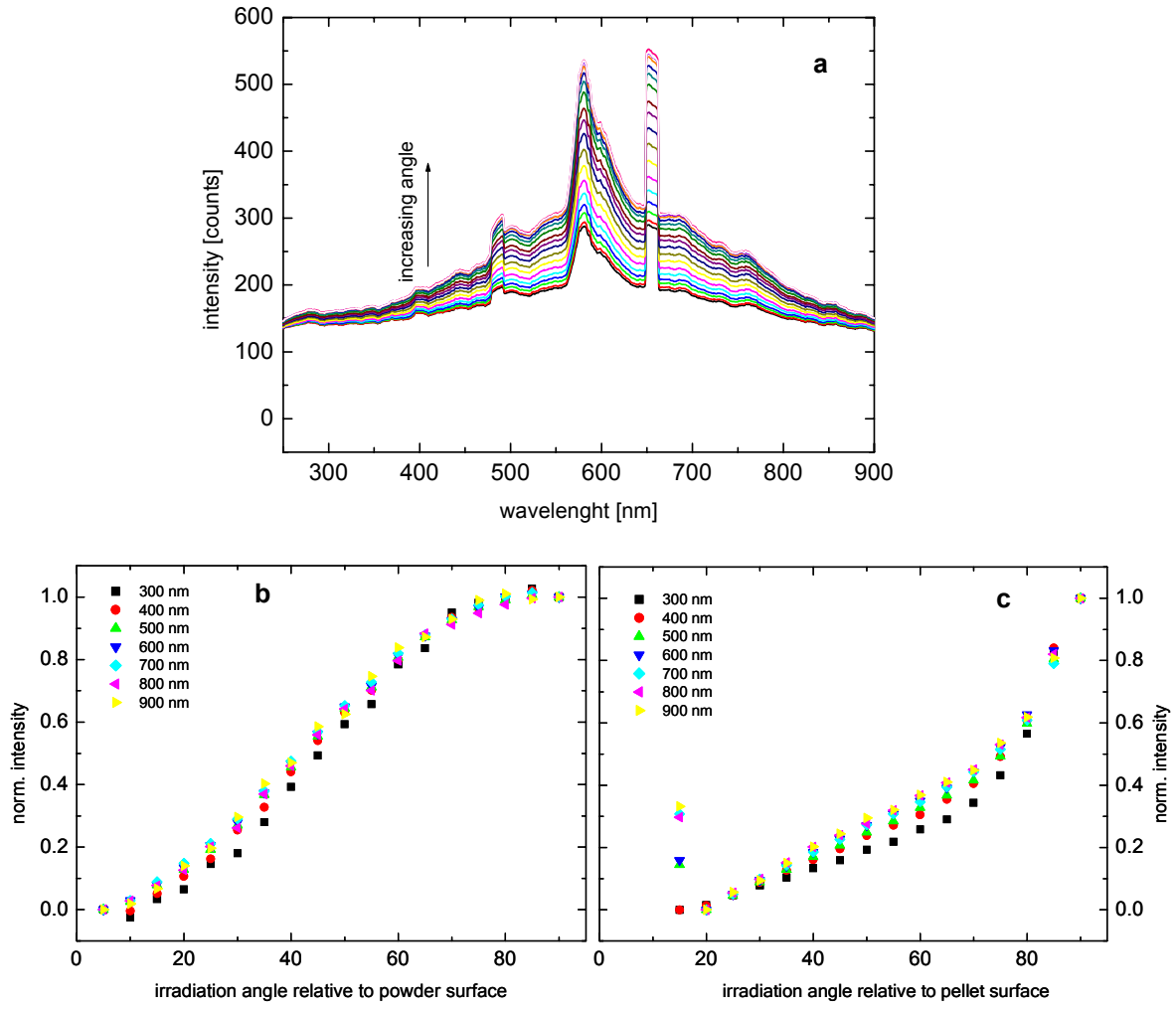

Figure 10 Reflectance intensity of BN as function of the light irradiation angle (a) and normalized intensity as function of the irradiation angle for BN powder (b) and a BN pellet (c)

The reflection intensity of both surfaces (powder and pellet) recorded by the 18 detection fibers increases as function of the irradiation angle. Maximum reflectance intensity of the powder surface is reached at an irradiation angle of 70° (sigmoidal shape). The maximum reflection intensity of the pellet surface can only be reached at an angle of 90° relative to the surface.

In principle, the more the irradiation angle relative to the surface increases the smaller the angle between incidence and reflected beam. The resulting overlap of the incident and reflected beam lead to an increase of intensity, if the angle of observation correspond to the irradiation angle (e.g. fiber bundle). Pressing of a pellet causes orientation of the crystallites, which are "elementary mirrors" and result in a macroscopic mirror plane. Due to the smaller fraction of diffuse reflected light of a mirror plane type surface, the maximum reflectance intensity can only be measured if the incident and reflected beam are perpendicular to the surface. This effect is less pronounced for randomly orientated crystals in a powder. In order to measure UV-Vis spectra of a pellet at maximum intensity, the combined XAS/UV-Vis cell was designed with an irradiation angle of 90° relative to the pellet surface.

The influence of the flattening of the surface on the absorption properties of the sample was investigated comparing a malachite ($Cu_2(OH)_2CO_3$) reference measured in a hemispherical reflectance setup [53] with a malachite pellet and powder spectrum recorded with the fiber optic system in an angle of 90° relative to the surface (Figure 11). A boron nitride pellet or BN powder was used as reflectance standard.

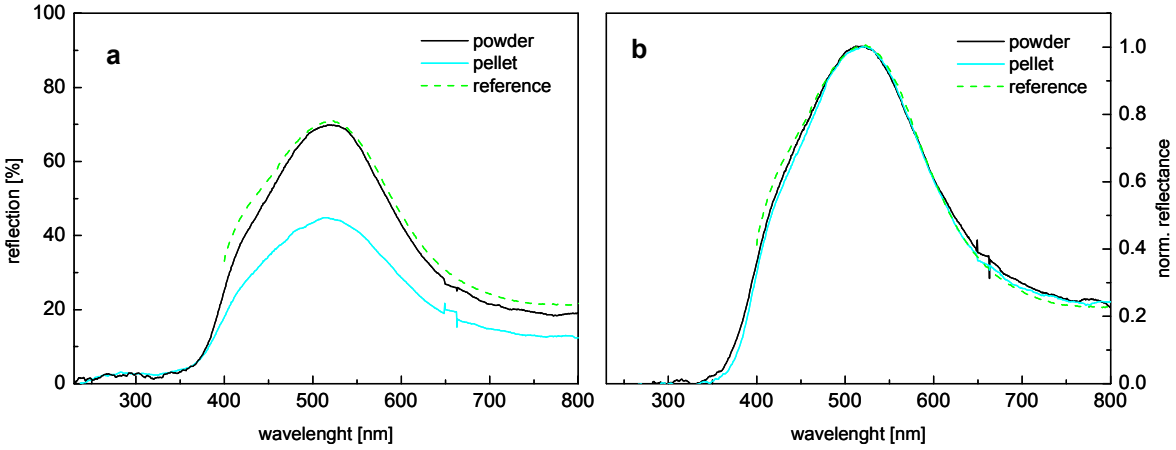

Figure 11 Reflectance UV-Vis spectrum (a) and normalized reflectance UV-Vis spectrum (b) of a malachite ($Cu_2(OH)_2CO_3$) reference [53] measured in hemispherical reflectance, and a malachite pellet and powder measured with the fiber optic system

The reference spectrum measured in the hemispherical reflectance setup, which enables to collect a larger fraction of the diffuse reflected light, is in good agreement with the powder spectrum measured with the fiber bundle system. The larger total reflectance of the powder spectrum compared to the powder spectrum indicates that specular reflection contributes to the whole UV-Vis spectra. However, the spectra shape and thus the absorption properties of the material remains the same (Fig. 11 b), except from slight intensity deviations of the reference sample (400 nm to 450 nm). These deviations may be assigned to the chemical differences of the samples, since the detailed preparation conditions of the reference sample remains unknown. The fraction of diffuse reflected light using a pellet as sample can be increased by roughening the surface. Thus, the sample pellets for the combined diffuse reflectance XAS/UV-Vis experiments were roughened by using (sand) paper.

3.3 Experiments

The efficiency of the combined XAS/UV-Vis cell was tested by several experiments. First, UV-Vis spectra of copper and zinc containing samples measured in the new cell were compared to references taken form the literature. Furthermore, the data quality as function of temperature programmed measurements was investigated for a separated UV-Vis and a combined XAS/UV-Vis experiment.

3.3.1 Reference Compounds

The near-surface electronic structure, the bulk structure and the activity of Cu/ZnO catalyst under working conditions and during activation was investigated in the new developed cell. Since copper metal, copper(II)oxide, copper(I)oxide, and zinc oxide are assumed to be the most prominent phases in the activated and non-activated catalyst, the corresponding references were measured in order to estimate the significance of the UV-Vis data. In Figure 12 the diffuse reflectance spectra measured of the following samples are presented: commercial CuO and Cu_2O powder; a mixture of commercial Cu and BN powder (ratio 1:1), and pure ZnO obtained by calcination of precipitated hydrozincite ($Zn_5(OH)_6(CO_3)_2$). The sample pellets were measured with a roughened surface at room temperature in the new cell.

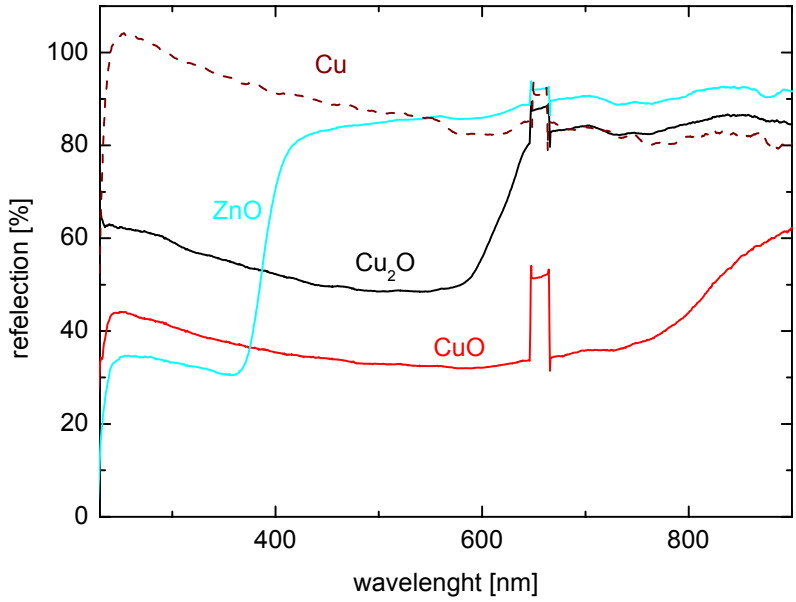

Figure 12 Diffuse reflectance spectra of Cu metal, CuO, Cu_2O and ZnO powder pellets measured in the new XAS/UV-Vis cell at room temperature

The UV-Vis diffuse reflectance spectra are in good agreement with the reference compounds taken from the literature. The broad absorption bands of CuO can be assigned to charge transfer bands at lower wavelength and to d-d transitions of Cu^{2+} in distorted octahedral surrounding (500 nm - 800 nm) [54,55], whereas Cu_2O transitions (Cu^{1+} in tetrahedral surrounding) only occur in a range 330 nm to 580 nm [56]. The resonance line of Cu metal at 570 nm to 620 nm is caused by collective excitation of conduction electrons (Cu plasmon) [57]. The spectral position of the plasmon resonance depends on the dielectric properties of the metal which again depend on the size and shape of the metal cluster. Thus, the plasmon resonance can be used to determine the size of a metal cluster. The minor intensity of the Cu plasmon resonance (Fig. 12) may be caused by the superimposition of partially oxidized metal surface (Cu_2O and CuO resonance) and diluting effects of BN.

ZnO is a band gap semiconductor with the hexagonal wurtzite crystal structure. The absorption edge of ZnO at approximately 330 nm corresponds to the transition from the highest valence band to the lowest conduction band. The absorption edge is in good agreement with the theoretical band gap at 3.26 eV (i.e., about 110 meV below the band gap energy) [58]. The temperature dependence of band gap electron transitions of ZnO is used to investigate the data quality in the UV range (chapter 3.3.2).

3.3.2 Temperature dependence of the band gap energy in zinc oxide

The ZnO band gap is sensitive to small changes in the temperature. As the temperature increases, the band gap energy decreases (i.e. the absorption wavelength gets higher) because the crystal lattice expands and the interatomic bonds are weakened. Thus, less energy is needed to break a bond and excite an electron in the conduction band. The temperature dependent electronic changes of ZnO allow to investigate the UV-Vis data quality of a temperature programmed experiment. In Figure 13 the reflectance spectra of ZnO as function of the temperature (313 K to 523 K) measured with the new cell and the resulting band gap energies determined by the inflection point of the absorption band are shown.

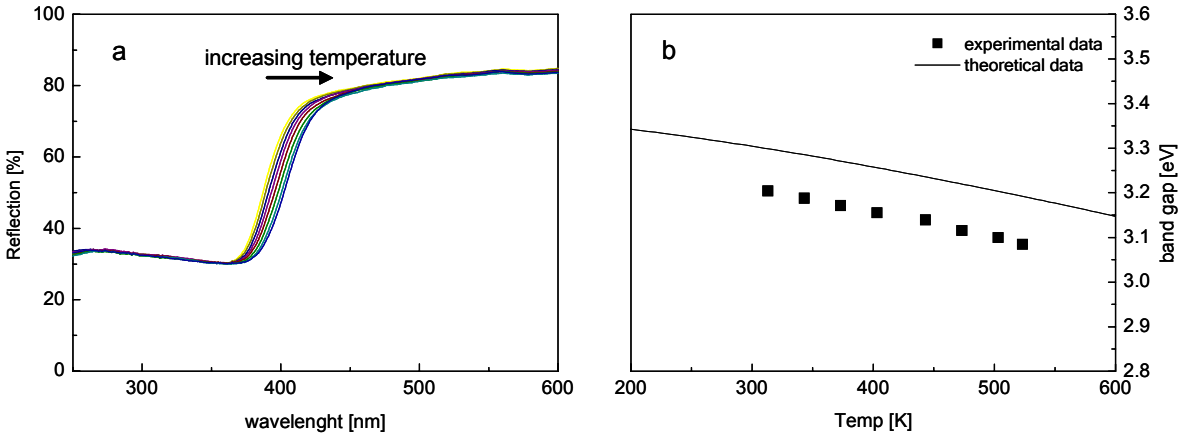

Figure 13 ZnO UV-Vis spectra (a) and the resulting band gap (b) as function of temperature measured with the combined XAS/UV-Vis cell

The relation of band gap energy and temperature is given by the equation,

$$E_g(T) = E_g(0) - \alpha T^2/(T+\beta) \qquad \textbf{(3-1)}$$

with the energy band gap at 0 K $E_G(0)$, and the constants α and β chosen to obtain the best fit to the experimental data. The exponential shape of the function is mainly reflected at lower temperatures, whereby an approximately linear relation of band gap energy and temperature can be assumed at higher temperatures. Qualitatively, the temperature induced decrease in ZnO band gap energy is in excellent agreement with the experimental data. Furthermore, the comparison between the experimentally determined band gap energies and the theoretical energies (Figure 13) taken form [58] ($E_G(0)$=3.380eV; α=(8.2±0.3)x10^{-4} eV/K; β=(700±30K)) shows only slight deviations of 0.1 eV. L Wang et al [58] reported that it is common to observe band gap energies about 0,1 eV below the theoretical determined energy.

The experiment clearly demonstrates that the new XAS/UV-Vis provides qualitative and quantitative information on the electronic structure of solids at higher temperatures. The UV-Vis absorption edge of ZnO can give information of the existence of certain defect types. Incorporation of copper creates acceptor level in ZnO which result in energy shifts of the band gap, and thus shifts in the absorption edge position. Klier proposed that Cu species dissolved in ZnO enhance the catalytic activity of Cu/ZnO catalyst [59]. A combined XAS/UV-Vis experiment of co-precipitated Cu/ZnO based catalysts under working conditions may provide a deeper insight into the geometric and electronic structure of ZnO. However, such an experiment is not suitable for the industrial catalyst (Cu/Zn ratio 70/30) because the UV-Vis spectrum is dominated by the electronic transitions of copper containing phases (e.g. Cu, CuO, Cu_2O, and residual carbonates and nitrates).

3.3.3 Combined in-situ XAS/UV-Vis measurements on the reduction of V_2O_5

Combined XAS/UV-Vis measurements were performed during the temperature programmed reduction of V_2O_5 in 2% H_2 (heating to 773 K at 6K/min). Figure 14a shows the V K-edge near region of the spectra (XANES) during reduction of V_2O_5 using the new combined technique. Each spectrum required 9 minutes to measure. The distinct pre-peak in the V K-edge XANES originates from 1s $\rightarrow$ 3d transitions, which becomes dipole allowed if the local octahedral symmetry is reduced. The decreasing intensity of the pre-peak as function of the reduction temperature indicates a less distorted octahedral symmetry of vanadium surrounded by oxygen. Factor analysis of the data in Figure 14b indicates that three components are significant for the changes in the near edge spectrum. Additionally, from the factor analysis, the abstract concentrations are obtained. The abstract concentrations are the amount of each abstract component required to simulate a set of measured spectra. Because the abstract components correspond to real components in the sample (i.e. chemical phases), the abstract concentrations are indicative of the changes to the chemical phases in the sample. In Figure 14, abstract concentrations are presented after normalization for the concentration of three components. Due to the increasing intensity of the pre-edge and the abstract concentrations, a sequential reduction pathway from V_2O_5 (orthorhombic, layer structure, distorted square pyramidal symmetry) via V_6O_{13} (monoclinic, layer structure, distorted octahedral symmetry) to VO_2 (tetragonal, rutile type, less distorted octahedral symmetry) is proposed. The decreasing “white line intensity” due to the reduction of V(V) to V(IV) corroborates the

assumed reduction pathway.

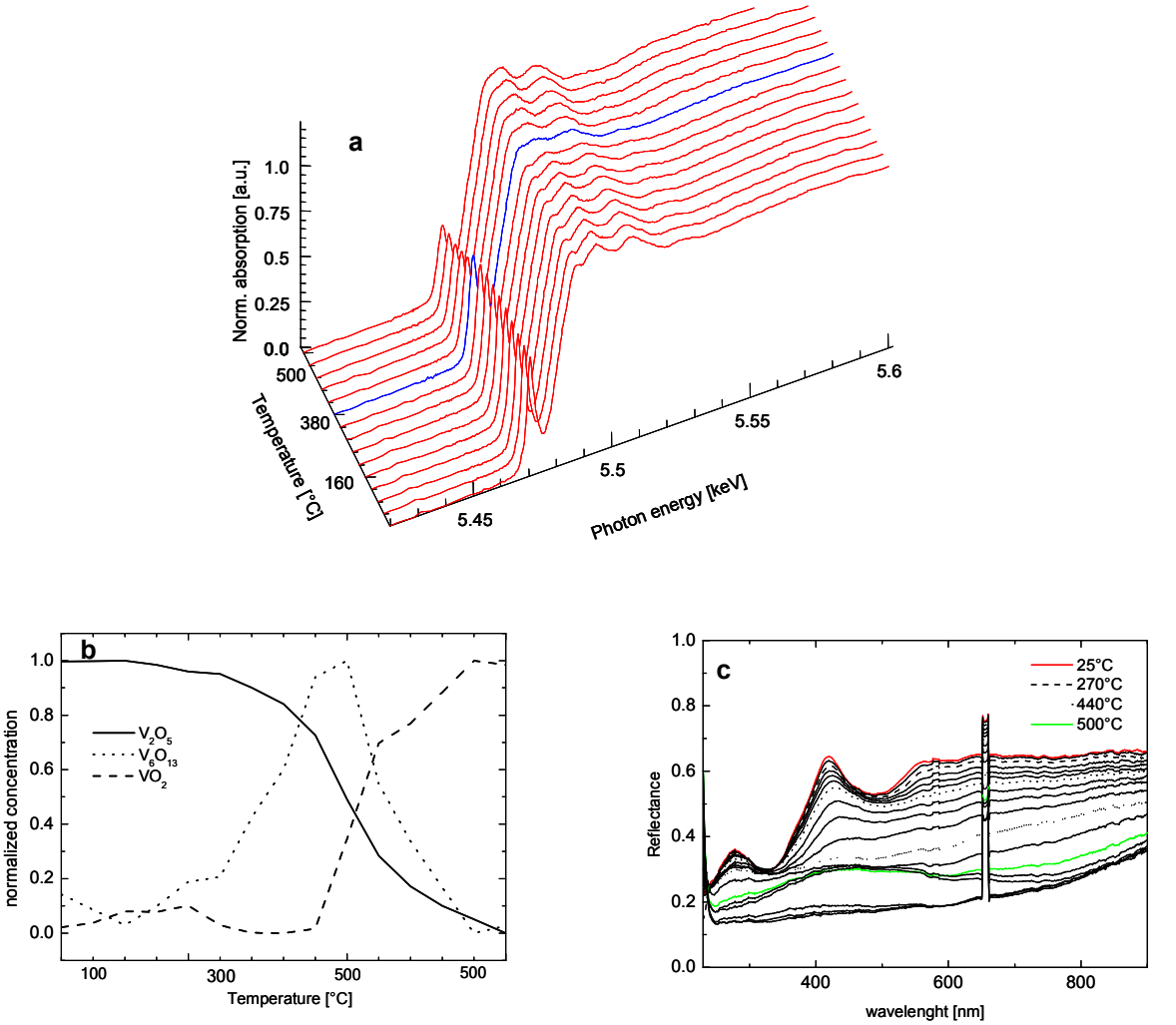

Figure 14 X-ray spectra taken of V_2O_5 during heating to 773 K in 2% H_2 (a), normalized abstract concentrations from principle component analysis (b), and UV-Vis data measured during heating of V_2O_5 to 773 K in 2% H_2 (c)

Figure 14c shows UV-Vis spectra measured during reduction of V_2O_5 by heating to 773 K in 2% H_2. V_2O_5 shows two distinct and broad absorption bands at about 330 and 490 nm. The absorption band at 330 nm is related to oxygen ligand to metal charge transfer bands (LMCT) and the band at 490 nm correspond to V(V) d-d electronic transitions, which is in good agreement with the literature [60]. The d-d transition bands seem to increase and broaden (i.e. decrease in reflectance) during reduction of V_2O_5 to the intermediate phase V_3O_{16}, whereas the LMCT transition gets broadened but remains constant in the intensity. The position of the absorption bands of V_3O_{16} is expected to be very similar to the bands corresponding to V_2O_5 due to the similar layered crystal structure. However, V_3O_{16} is a mixed valence oxide consisting of 4 V^{4+} (d^1) + 2 V^{5+} (d^0) electronic configurations. The partial

reduction of V (V) leads to a shift of the LMCT transitions band, as expected for O→V charge transfers, involving decreasing oxidation states of the metal. Thus, the superimposition of V^{4+} and V^{5+} LMCT and d-d- transitions causes diffuse and broad absorption bands, which is in good agreement with the experimental data. The overall decrease in reflection is probably caused by thermal expansion of the cell and/or changes in the macroscopic surface characteristics during reaction. Two additional broad absorption bands at 600 to 800 nm and below 300 nm occur at temperatures about 773 K. Qualitatively, the transition at 600 to 800 nm is in good agreement with the diffuse reflectance spectra of VO_2 taken from [61]. The results of the UV-Vis spectroscopy support the assumption of a sequential reduction of V_2O_5 via V_3O_{16} obtained by the XAS experiment. The comparison of the UV-Vis and XAS data clearly indicate that an earlier onset of reduction is observed by the UV-Vis spectra. The result can be traced back to the more surface sensitive diffuse reflectance UV-Vis spectroscopy compared to the bulk method XAS. Sequential reaction pathways starting from the surface of the sample into the bulk can thus be investigated by the combination of both methods.

3.4 Conclusion

The combined in-situ XAS and UV-Vis cell is well suited to produce high quality data for both energy ranges. In combination with gas phase analyses this cell can be used for the investigation of solid materials under reaction conditions. First investigations of Cu-based catalysts under working conditions and during reduction using the new cell and a Perkin-Elmer Lambda 9 UV-Vis-NIR spectrometer reveal the complexity of UV-Vis spectra obtained from industrial used Cu/ZnO catalysts. The UV-Vis spectra exhibit broad and diffuse bands in a range from 250 to 900 nm. Cu plasmon resonance of the reduced catalysts was not detectable. The absorption edge of ZnO due to electron transition from the valence band to the conduction band is superimposed by electronic transitions of copper containing phases such as CuO, Cu_2O, and residual carbonate components. The overlap of a large variety of electronic transitions does not allow an unambigous identification of absorption bands. Since the interpretation of Cu/ZnO catalysts remains complicated further investigations have to follow in order to unravel the complex UV-Vis spectrum. However, the investigation of the calcination of hydroxycarbonate precursors using the new combined XAS/UV-Vis cell gives deeper insight into the phase transformation during temperature programmed reaction (chapter_4.3).

4 Preparation of Cu/ZnO catalysts as function of precipitate ageing

4.1 Cu/ZnO catalysts prepared by co-precipitation

Co-precipitation of Cu,Zn (Al) precursors is one of the most common methods to prepare highly active nanostructured Cu catalysts. The industrial relevant "standard batch precipitation" allows to manufacture large quantities of material. The major drawback of the process is the difficulty to control the precipitation. A large variety of kinetic and thermodynamic variables affect the formation of the solids. The concentrations and chemical potentials of the reagents are locally and temporally not constant in a reactor where precipitates and dissolved ions coexist. The homogeneity of the product varies as a function of the precipitation period because phase transitions caused by ageing of first formed precipitates could occur while fresh precipitates are still formed. The "continuous precipitation" at constant temperature allows controlling the pH by changing the dropping velocity of the precipitation agent.

In this work Cu,Zn hydroxycarbonates were precipitated at constant pH (pH=7) at 65 °C. The pre-mixed and pre-heated (60 °C) metal nitrate solution was added to a 2000 ml reactor at a constant drop rate (25 ml/min). The pH was controlled by a "pH-electrode/PC/Na_2CO_3-pump device". Changes in the pH of the reactor solution were measured by a Ag/AgCl single-rod measuring cell. The dropping rate of the sodium carbonate solution is controlled by the computer. Therefore, the incoming signal produced by the pH electrode ("control variable") was compared to the wanted pH value ("reference variable"). Differences in both values were balanced by an according control of the Na_2CO_3 pump. The computer is connected to a real time operating system (VxWorks). The highest possible response on slight changes of the pH was realized with a software implemented Proportional-Integral-Differential (PID) algorithm which allows processing with a time resolution of 100 ms. The precipitation solution was stirred with a paddle mixer at 150 turns per minute. More details on the precipitation reactor are given in the PhD thesis of Bettina Bems [TU Berlin, 2003].

Preparation of Cu/ZnO catalysts by co-precipitation is a multi step process including ageing, washing, drying, calcination and reduction. The general preparation scheme is depicted in Figure 15. Experimental details about the post treatment steps are given in chapter 2.6.

Figure 15 General preparation scheme for the co-precipitation of Cu/ZnO catalysts

In-situ UV-Vis investigations during precipitate ageing add complementary information to already gained results obtained by pH measurements and ex-situ XRD and IR experiments. Diffuse reflectance UV-Vis spectroscopy in solution produces high quality data which enable to follow phase transformations during ageing using a solid sensitive in-situ spectroscopy. The calcination process of differently aged precursors is investigated using the new combined XAS/UV-Vis cell and temperature programmed XRD experiments. In addition to ageing, selected preparation steps such as calcination and reduction were investigated as a function of precipitate ageing. The results are presented in the following chapter. The resulting products were investigated by XRD, XAS, and XPS. Furthermore, the effect of ageing on the reduction properties of the resulting oxide precursors was investigated using XAS, XPS, and TG-MS methods.

4.2 In-situ UV-Vis investigations during precipitate ageing

4.2.1 Introduction

Ageing of freshly precipitated Cu,Zn hydroxycarbonates in the mother liquor is an important procedure to control the microstructure and activity of the resulting Cu/ZnO catalysts. Ripening, phase transitions, agglomeration, and dissolution processes of the precursor phases occur during ageing. A detailed knowledge of the chemical processes occurring during ageing and their implication on the structure of the resulting catalyst is necessary to control the performance of the catalyst. The ageing process of Cu,Zn hydroxy carbonates was frequently

investigated in the last decade [62,63,17]. Ageing of the precipitates leads to a spontaneous crystallization of the initially amorphous precursors accompanied by a color change from blue to green. Detailed investigations of the ageing process of Cu,Zn hydroxycarbonate precursors with a Cu/Zn ratio of 70/30 were performed by B. Bems et al. [17] using ex-situ XRD and IR spectroscopy. It was found that a mixture of amorphous georgeite [$(Cu,Zn)_2(OH)_2(CO_3)$] and a hydroxy-rich carbonate [$(Cu,Zn)(OH)_y(CO_3)_x$] quickly transforms in the crystalline polymorphs rosasite [$(Cu_xZn_{1-x})_2(OH)_2(CO_3)$] and aurichalcite [$(Cu_xZn_{1-x})_5(OH)_6(CO_3)_2$] after approximately 25 min. The amount of aurichalcite decreases to 50% of the initial value (ratio aurichalite/rosaite 70/30) within the first three hours of ageing. A pH drop in the mother liquor from 7 to 6.8 indicates the crystallization of the solids. The increasing acidity is assumed to originate from ion exchange of nitrates incorporated in the amorphous solids to hydroxides. It is suggested that the main fraction of nitrates is incorporated in the hydroxy rich phase. Additionally, incorporation of carbonates during crystallization causes a decrease in the pH, because the resulting lower carbonate concentration in the solution shifts the hydrocarbonate/water equilibrium to the right side ($HCO_3^- + H_2O = H_3O^+ + CO_3^{2-}$). The rapid increase in the pH after the crystallization may be caused by the enrichment of CO_3^{2-} and/or OH^- ions in the mother liquor because of partial dissolution of the crystalline rosasite phase or more likely the delayed transformation of the amorphous hydroxy-rich carbonate to aurichalcite. Assuming a lower concentration of OH^- in the crystalline aurichalcite compared to its hydroxy-rich progenitor, continuous dissolution/re-precipiation processes from the amorphous phase to aurichalcite cause a higher concentration of OH^- ions in the mother liquor.

Structure and composition of the precursors formed during precipitate ageing were investigated directly using ex-situ techniques (XRD and IR) or indirectly by measuring changes of the ion concentration in the mother liquor (pH and conductivity). Additionally, it would be desireable to develop solid sensitive in-situ techniques which provide reliable structural information of the solids during ageing in the mother liquor. Diffuse reflectance UV-Vis spectroscopy is one of the most promising candidates for in-situ investigations of the precipitation and ageing process due to the good time resolution, the easy handling of the fiber optic system, and the low sensitivity to changes in the mother liquor. Combining a variety of methods such as pH, conductivity, UV-Vis spectroscopy, light scattering, and calorimetric measurements may be a step towards unraveling the complex chemical and kinetic processes during precipitation.

4.2.1.1 Structure of Aurichalcite and Rosasite

The structures of aurichalcite $[(Cu_xZn_{1-x})_5(OH)_6(CO_3)_2]$ and rosasite $[(Cu_xZn_{1x})_2(OH)_2(CO_3)]$ are depicted in Figure 16. The structure of aurichalcite has been determined by single crystal structural investigations [64]. Aurichalcite possesess a monoclinic crystal structure in the space group $P1\ 2_1/m1$. The aurichalcite structure is built up of layers of edge-sharing tetragonally distorted octahedra. The distorted octahedral site is occupied by randomly distributed Cu and Zn ions. Additionally, Cu and Zn are trigional bipyramidally coordinated by 5 oxygen. The trigonal bipyramides share corners with the octahedra of the layer. Only the space between every second double layer of octahedra reveals the trigonal bipyramidal polyhedra. The other double layer interspace is occupied by tetrahedrally coordinated Zn atoms (atomic position entirely occupied by Zn has tetrahedral coordination). Thus, the aurichalcite structure can be described by a double layer structure of edge-sharing octahedra, in which the space between each double layer is alternatively occupied by either Cu/Zn containing trigonal bipyramides or tetrahedrally coordinated Zn ions. The carbonate ions (CO_3^{2-}) are located between the double layers. One oxygen atom of a carbonate ion is shared with the octahedra of the layer; the other oxygen atoms are shared with the corners of the trigonal bipyramides or with the corners of the Zn containing tetrahedra.

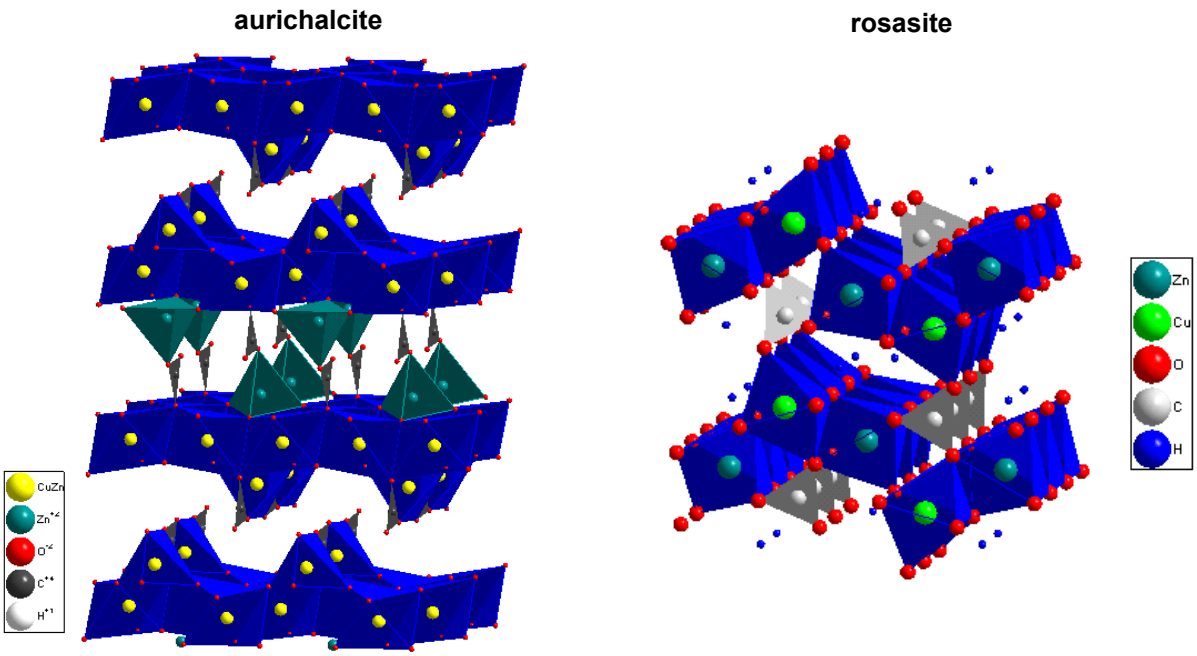

Figure 16 Crystal structure of aurichalcite and rosasite parallel to the [001] plane

Rosasite possessess a monoclinic crystal structure in the space group $P\,2_1/m$ and is an isotype of malachite. The Cu atoms are coordinated by four oxygen and two hydroxy groups in a strongly distorted octahedron, whereas Zn is surrounded by four hydroxy groups and two oxygen in a less distorted octahedron. Both, the Zn and the Cu octahedra share edges forming Cu-based and Zn-based "columns". Two "octahedra columns" form "octahedral ribbons" by sharing the octahedral edges of the Cu-based and Zn-based column. The octahedral ribbons (two columns large) are connected by corner-sharing of the octahedral and carbonate groups. Each carbonate group is linked to three "octahedral ribbons".

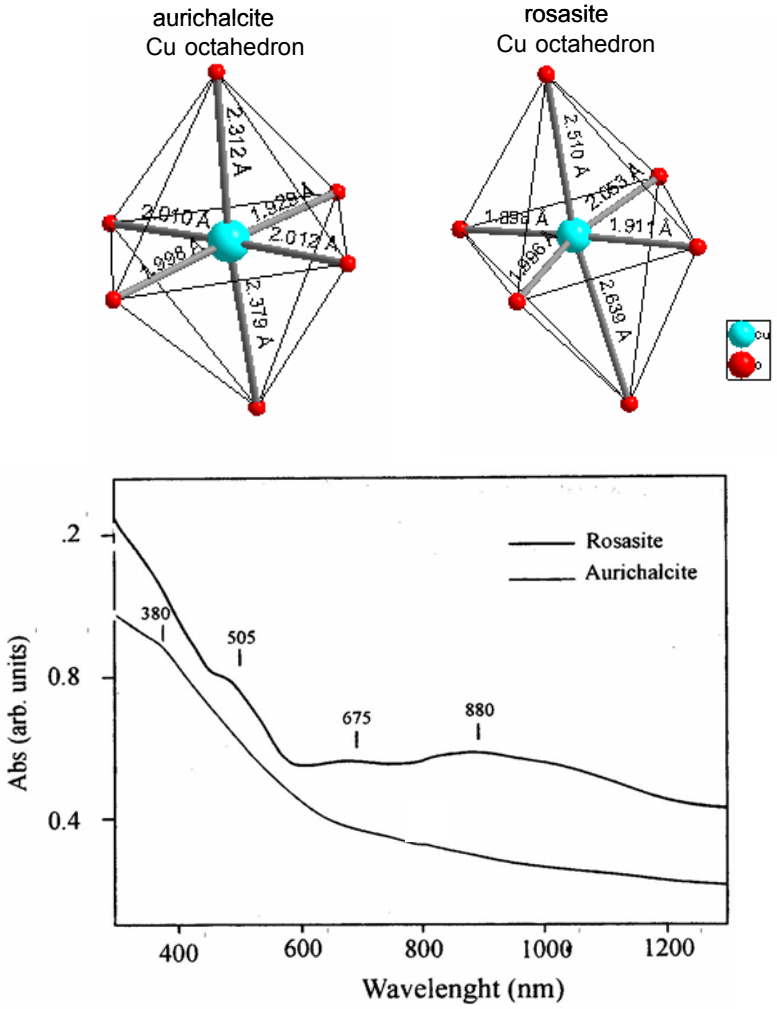

Figure 17 Octahedral coordination of Cu^{2+} in roasite and aurichalcite and the corresponding optical spectra taken from [65]

The optical absorption of rosasite and aurichalcite was investigated by B.J. Reddy et al. [65]. The corresponding absorption spectra are depicted in Figure 17. Absorption bands caused by d-d transitions can only be excepted for divalent copper (Cu^{2+}, electronic configuration $3d^9$) due to unoccupied d states compared to divalent Zn (Zn^{2+}, electronic configuration $3d^{10}$, fully

occupied d states). In a tetragonally distorted octahedron (expansion along the z axis) the d orbitals of the ground state ^2E (d_{xy}, d_{xz}, d_{yz}) split into two degenerated orbitals with lower energy $^2B_2$ (d_{xz}, d_{yz}) and one with higher energy $^2A_1$ (d_{xy}). The upper state $^2T_2$ (d_{x2-y2}, d_{z2}) split into an energetically lower $^2B_2$ state (d_{z2}) and higher state ^2E (d_{x2-y2}). In a tetragonally distorted octahedron, three bands can be assigned to the following transition according to the selection rules of dipole allowed transitions: $^2B_1 \rightarrow {}^2A_1$, $^2B_1 \rightarrow {}^2B_2$, and $^2B_1 \rightarrow {}^2E$.

Rosasite exhibits three absorption bands at 880, 675, and 505 nm, which is in good agreement with d-d transitions of Cu^{2+} in tetragonal symmetry (Figure 17). The absorption band at 380 nm may originate from metal to ligand charge transfer of Cu^{2+} of Zn^{2+} and oxygen. The less distorted symmetry of the Cu octahedron in aurichalcite (Figure 17) leads to a smaller crystal field splitting and, hence, to a shift of the three d-d transitions to lower energies (e.g. higher wavelength). The optical spectra of aurichalcite exhibit broad and diffuse absorption bands. Only one broad absorption at 380 nm could be identified. The superimposition of d-d transitions of Cu^{2+} in tetragonal symmetry and Cu^{2+} in trigonal bipyramidal symmetry as well as additional charge transfer bands may be the explanation for the broad and diffuse optical spectra of aurichalcite. In a precursor composition where aurichalcite and rosasite coexist, an unambiguous separation of the absorption bands related to one single component will be complicated. However, the two optical spectra differ in the intensity ratio of the absorption bands at 380 nm and 505 nm as well as the minor absorption at wavelengths of 550 nm to 1000 nm in aurichalcite. In particular, the more pronounced absorption of aurichalcite at 380 nm relative to the absorption at 505 nm can be used for the qualitative interpretation of the following diffuse reflectance UV-Vis measurements during aging in the mother liquor.

4.2.2 Results and Discussion

Diffuse reflectance UV-Vis spectra of the precipitates were recorded every 10 seconds in a range of 230 to 800 nm during precipitation and ageing (integration time: 1000 ms; average:10). Prior to the time-resolved measurement, the UV-Vis spectrometer was calibrated using $BaSO_4$ as white standard. Therefore, 115 g $BaSO_4$ were dispersed in 2000 ml water (~ 6 g per 100 ml). The “white standard” spectrum was recorded during constant stirring under reaction conditions (150 turns per minute, 333 K). The resulting UV-Vis spectra and the corresponding pH evolution during precipitation at constant pH and during precursor ageing are depicted in Figure 18.

After approximately 5 min precipitation the first optical reflection spectrum can be measured (Figure 18). After that time a sufficient number of particles are present to yield a detectable reflection signal. Continuous precipitation results in an increase in the total reflection up to 300 %. It is assumed that the increase in total reflection above 100 % is caused by a larger number of particles crossing the light beam compared to the white standard $BaSO_4$.

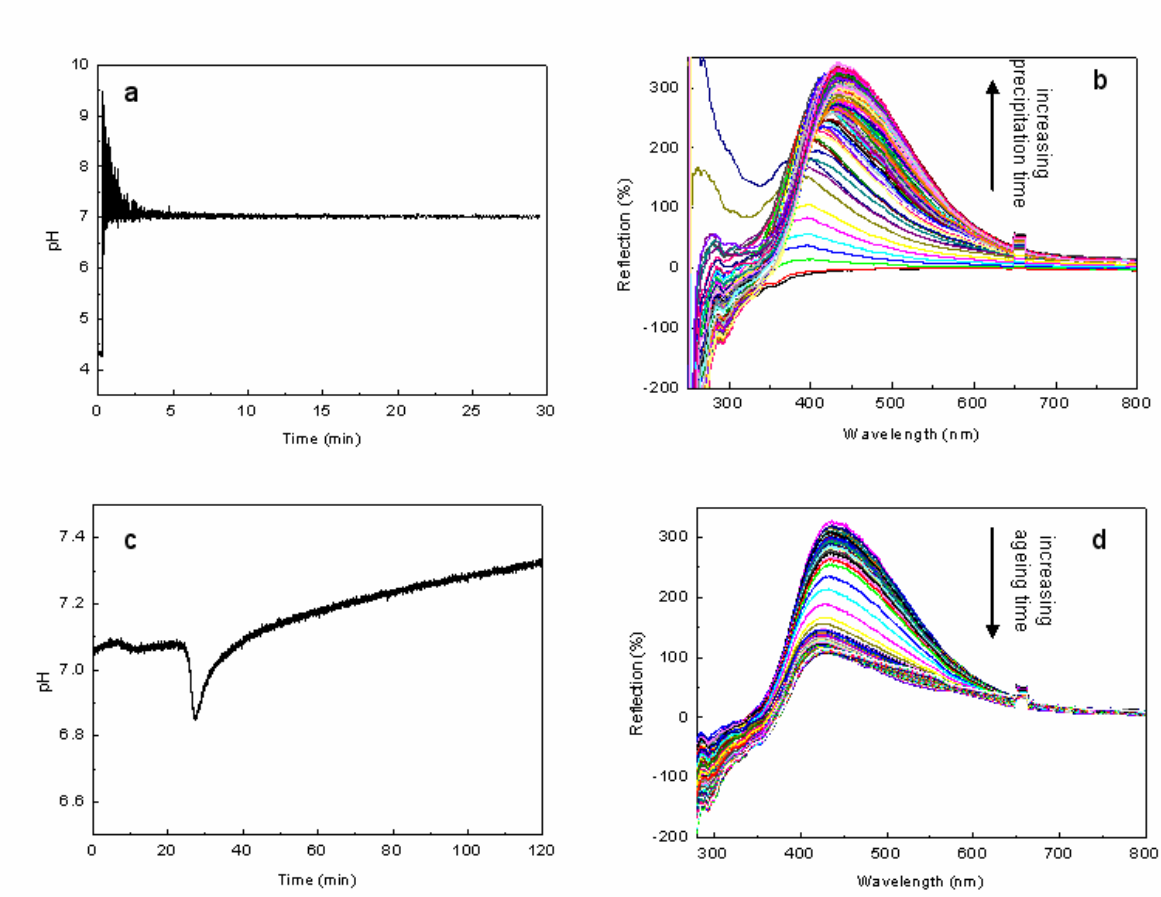

Figure 18 Diffuse reflectance UV-Vis spectra (b) and the corresponding pH (a) during precipitation and diffuse reflectance spectra (d) and the corresponding pH (c) during precipitate ageing in the mother liquor

The UV-Vis spectra exhibit distinct absorption bands in a range of 500 to 800 nm which are assumed to originate from the amorphous precursors (georgeite and hydroxy-rich carbonate). The crystallization during ageing of the initially amorphous precursor indicated by the pH drop after ~25 min (Figure 18 c) is accompanied by a color change from blue to green. A sudden increase in the optical absorption during precipitate ageing in the mother liquor correlates with the spontaneous crystallization. Only slight changes in the absorption properties of the precipitates were observed during the first 25 min of ageing. However, a strong increase in absorption (e.g. decrease in reflection) in a range of 400 to 600 nm after 25

min indicates the crystallization, which is in good agreement with the corresponding pH drop. For a detailed determination of the absorption bands developing during ageing, difference spectra of the UV-Vis reflection spectra (Figure 18 d) were calculated by subtracting each measured spectrum (time t > 0) from the first measured one (time t = 0). The resulting difference spectra were normalized from 0 to 100 in the y-axis scaling to enable the conversion into Kubelka-Munk units (F(R)*). The normalization was conducted by rescaling the maximum intensity of the most intensive difference spectrum depicted in Figure 19a (i.e. ~ 190) to 100. All the other spectra were rescaled relative to the maximum intensity (i.e. 190). The resulting difference spectra calculated in Kubelka-Munk units are shown for 10-20 min ageing, 20-30 min ageing and 30-70 min ageing in Figure 19 b,c, and d, respectively.

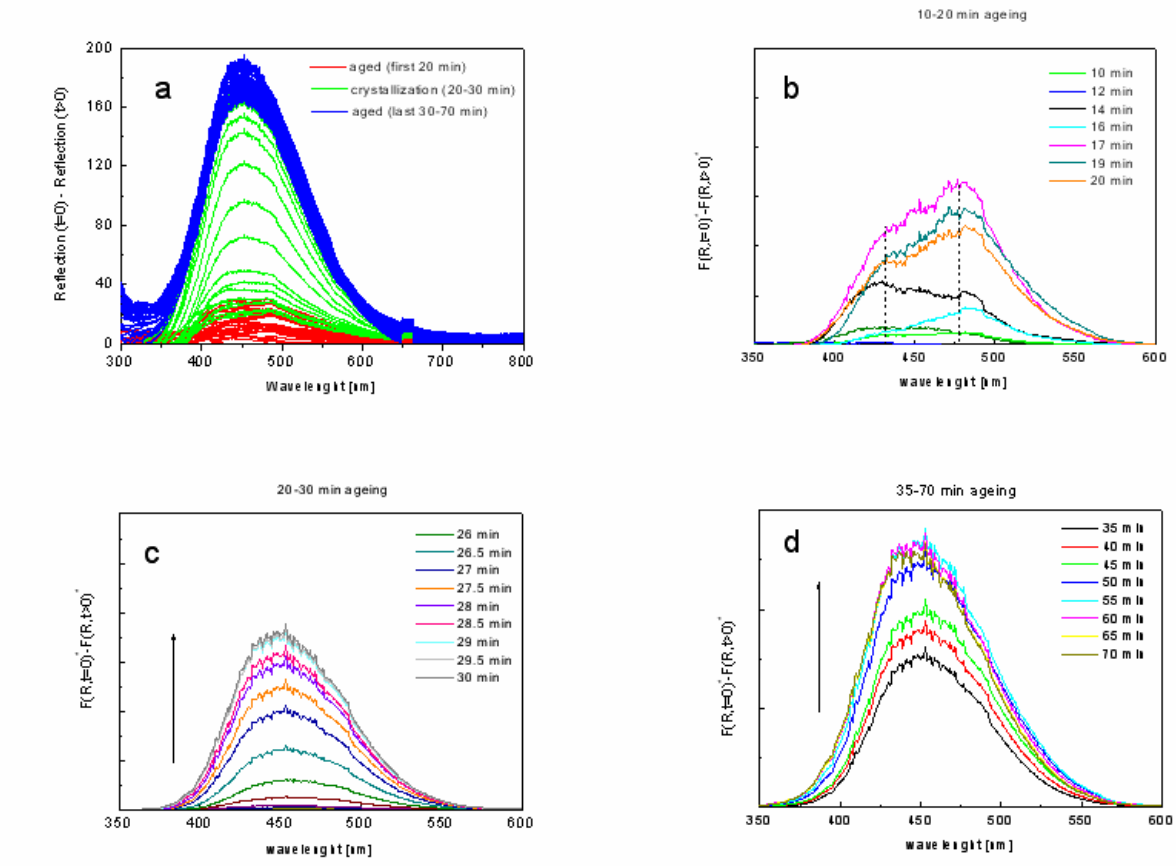

Figure 19 Difference spectra (Reflection (t=0)- Reflection (t>0)) calculated from the reflection data (Figure 18 d) (a) and the difference spectra (Figure 19b) converted into Kubelka-Munk units from 10 to 20 min ageing (b), 20 to 30 min ageing (c) and 35 to 70 min ageing (d)

Two broad and diffuse absorption bands at 430 and 470 nm could be identified during the first

20 min ageing (Figure 19 b; dotted line). A sudden increase in the intensity of both absorption bands accompanied by slight shifts in band position to lower wavelengths occurred between 20 and 30 min ageing time (Figure 19c, a). In the time range from 45 to 55 min precipitate ageing, one observes a weak increase in the intensity of the two absorption bands (Figure 19 a). However, the "blue shift" (i.e. the shift to lower wavelength) is much more pronounced between 35 and 70 min ageing (Figure 19d) compared to the "blue shift" between 20 to 30 min ageing (Figure 19c). Thus a stronger increase in the absorption band at 430 nm compared to the absorption at 470 nm can be assumed.

In addition to the method described above (i.e. calculating the absorbance in Kubelka-Munk units by using the normalized difference spectra of the reflection raw data), a second method was employed to determine the absorption bands developing during ageing.

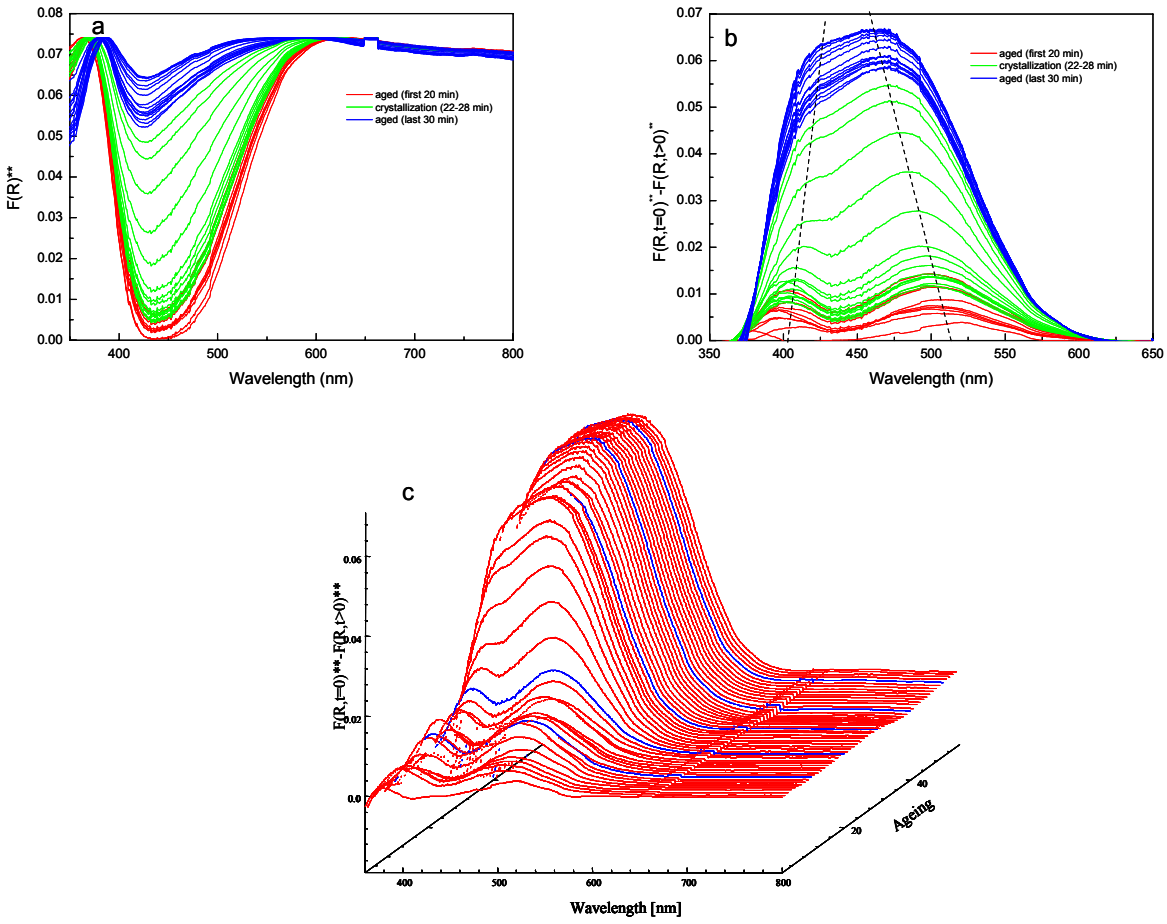

Figure 20 Optical absorbance of the precipitates as a function of ageing in Kubelka-Munk units (a) and the resulting difference spectra (b) calculated by subtracting the measured spectrum from the first measured one (0 min ageing). Three dimensional evolution of the absorption bands as function of ageing (c)

For this, the reflection data were normalized prior to converting into Kubelka-Munk units (F(R)**). Both, the resulting absorption spectra and the difference spectra calculated by subtracting the first measured spectrum (time t=0) from each measured one (time t>0) are depicted in Figure 20. Two absorption bands in a range of 400-430 nm and 470-510 nm could be identified between the 0 and 20 min ageing, which is in good agreement with observed absorption bands in Figure 19. Furthermore, the sudden increase in the intensity of both absorption bands between 20 to 30 min ageing and weak increase of both bands between 35 to 60 min ageing coincide with the results obtained from the first calculation method. Therefore, changes of the precursor during ageing identified by UV-Vis spectroscopy can be separated into two steps: A first step with a major increase in absorbance between 20 and 30 min and a second step between 45 and 55 min ageing (minor increase in absorbance). In contrast to the uniform increase of both absorption bands during the first step, the increase of the absorption band at 400-430 nm is more pronounced during the second step compared to the band at 470-510 nm (Figure 20 c), which is in good agreement with Figure 19 d.

The evolution of the absorbance at 470/510 nm compared to the pH evolution during ageing is shown in Figure 21. The sudden increase in absorbance at 25 min ageing is in good agreement with the pH drop indicating the crystallization of the precursors. Slight and continuous increase in the pH was observed after the crystallization which may be caused by continuous dissolution/re-precipitation from the hydroxy-rich amorphous phase to aurichalcite (p.44). The increase in absorbance after the crystallization (second step) clearly indicates that not only ripening occurs during precipitate ageing but also additional reactions after crystallization need to be taken into account.

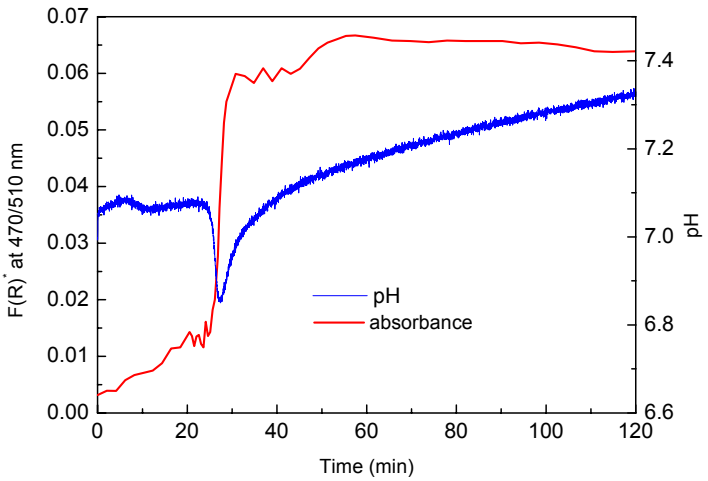

Figure 21 Evolution of absorbance at 470/510 nm and pH evolution during precipitate ageing

The absorption band at 470-510 nm and 400-430 nm can be assigned to d-d transitions of Cu^{2+} electrons of rosasite and aurichalcite, which is in good agreement with the literature [65] and the experimental result obtained by ex-situ XRD measurement. The pH drop and the color change from blue to green can be assigned to the crystallization of amorphous precursors to crystalline rosasite and aurichalcite. The unknown local geometry of Cu^{2+} and Zn^{2+} in the amorphous precursor does not allow a detailed description of the electronic transitions leading to the measured UV-Vis spectrum at the beginning of the ageing process. However, qualitatively the absorption bands of the amorphous precursor (600 to 800 nm, Figure 18d first spectrum) correlate with the blue color of the suspension. Absorption in a range of 600 to 800 nm leads to a selective filtering of red and orange light from the visible white light. Thus the precursor compound exhibits a bluish green color (complementary color). The color change of the precursor after crystallization is caused by the additional absorption bands at 400-430 nm and and 470-510 nm. The superimposition of the blue color related to the absorption above 600 nm and yellow/orange color (400-430 and 470-510 nm) result in an overall green color of the suspension after crystallization. The theory of color is a useful method to roughly interpret optical spectra. Both, the color change of the suspension from blue to green and the corresponding crystallization of the precursors is reflected in the UV-Vis spectra recorded during ageing

The increase in absorbance between 45 and 60 min ageing may be caused by particle size effects. Furthermore, the solute concentration may locally differ in a continuous stirring reactor (2000 ml) which may cause a locally delayed crystallization of the amorphous precipitates. However, changes in the optical absorption spectra due to particle size effects or locally delayed crystallization result in a uniform increase of the overall absorption. Thus, both effects do not explain the non-uniform changes of the UV-Vis spectra observed during the second step of ageing.

The UV-Vis data clearly indicate the separation of the ageing process in two general steps (Figure 21) according to a non-simultaneously crystallization. A sequential crystallization of the amorphous georgeite to rosasite followed by a delayed transformation of the amorphous progenitor of aurichalcite is assumed, as discussed in the following:

1. The pH drop does not necessarily correlate with the crystallization of the amorphous modification of aurichalcite. B. Bems attributed the pH drop in the mother liquor to the crystallization from georgeite to rosasite [17]. The investigations of binary Cu/Zn hydroxycarbonates with varying molar ratio clearly indicate that the sudden decrease

of the pH is only observed in the presence of an amorphous modification of rosasite [17]. Ageing of Cu,Zn hydroxycarbonates with a molar ratio Cu/Zn 70/30 results in a mixture of 80 % rosasite and 20 % aurichalcite. Thus, it is questionable if the crystallization attributed to aurichalcite is detectable using pH measurement of the mother liquor. The powder XRD pattern of the precursor obtained directly after the pH drop exhibit lines attributed to aurichalcite and rosasite. It is assumed that a small fraction of aurichalcite is already formed after crystallization of rosasite, but the main fraction of the polymorph related to aurichalcite remains amorphous.

2. The precipitation is a complex sequence of events starting with the formation of copper hydroxides due to the more acidic character of Cu^{2+} compared to Zn^{2+} which then reacts with Zn^{2+} and CO_3^{2-} forming a mixed hydroxycarbonate (georgeite). In a second step, the more slowly precipitating zinc forms a hydroxy-rich material together with the residual Cu^{2+} ions [17]. The precipitates first formed (e.g. georgeite) are aged for a longer time in the mother liquor. Thus an earlier crystallization of the amorphous progenitor of rosasite compared to that of aurichalcite is expected.
3. Although both amorphous progenitors precipitate simultaneously (i.e co-precipitation) they probably differ in the kinetics of phase transformation. The kinetics of solvent mediated phase transitions was investigated in detail by P.T. Cardew and R.J. Davey [34]. The overall transformation rate depends on both the growth rate of the crystalline phase and the dissolution rate of the amorphous progenitor. The dissolution rate may deviate for both amorphous phases. Consequently, the kinetics of phase transformation deviate between the progenitors of rosasite and that of aurichalcite.
4. The in situ UV-Vis data recorded during ageing support the assumption of a sequential crystallization of the amorphous progenitors (Figure 19 d; Figure 20 c). The intensity ratio of the two absorption bands (400-430nm and 470-510 nm) remains roughly constant during the first crystallization step, whereas the increase in absorption at ~400 nm is more pronounced for the second step. The experimental results are in good agreement with the reference spectra of aurichalcite and rosasite (Figure 17). The formation of aurichalcite should lead to UV-Vis reflectance spectra with a more pronounced absorption band at ~400 nm compared to rosasite.

4.2.3 Conclusion

In summary, in-situ diffuse reflectance UV-Vis spectroscopy is a powerful tool to obtain complementary information concerning solid precipitates formed during a subsequent ageing procedure. The investigations clearly demonstrate that an in-situ solid sensitive spectroscopy gives a deeper insight into the complex chemical processes during precipitate ageing. Basically, the results of the UV-Vis investigations correlate with the results obtained by pH, conductivity, and ex-situ XRD measurements during ageing (i.e. crystallization of the amorphous precursor). Changes in the absorption properties of the suspension after the pH drop clearly indicate ongoing chemical events such as phase transition, dissolution, and renucleation processes, which could not be identified by measuring the pH and/or conductivity of the solution. A sequential crystallization pathway of rosasite followed by the delayed transformation of the amorphous progenitor of aurichalcite could be proposed based on the UV-Vis investigations.

4.3 Calcination as function of precipitate ageing

4.3.1 Introduction

The thermal decomposition of Cu-based hydroxycarbonate precipitates (calcination) results in mixed metal oxides. In addition to the precursors formed during precipitation and ageing, the decomposition and calcination steps determine the microstructural properties of the catalyst. Changes in the crystallinity, phase composition, and homogeneity of the precursor during precipitate ageing will be reflected in the characteristics of the thermal decomposition ("memory of the material"). The gas phase evolution of H_2O and CO_2 during temperature programmed decomposition in synthetic air (RT to 600°C) of a non-aged and a 120 min aged precipitates is compared in Figure 22 a. Prior to calcinations, the aged precipitates were washed 5 times in destilled water and dried at 120 °C in static air for 20 h. The calcination of Cu,Zn based hydroxycarbonates can be separated into three different decomposition steps (Figure 22 b). Water is released in a first step between 100 and ~ 250 °C. In a second step, water and CO_2 are released simultaneously in a temperature range from 250 and ~ 400°C.

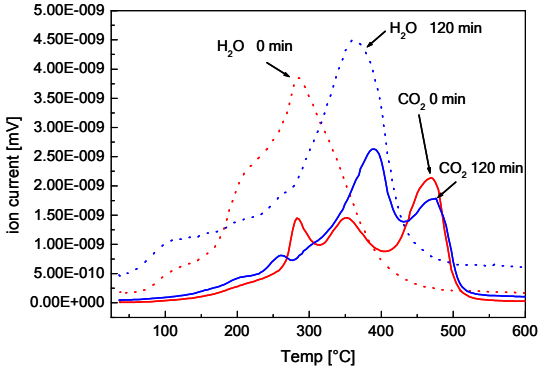

Figure 22 a Gas phase evolution of CO_2 and H_2O during thermal decomposition in air of a 0 min and 120 min aged precursor

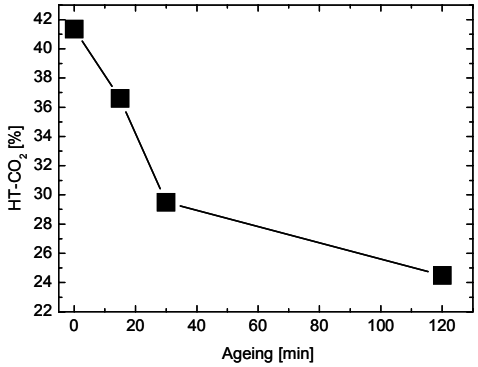

Figure 22 b Amount of CO_2 above 400°C (HT-CO_2) relative to the overall CO_2 amount during thermal decomposition as function of precipitate ageing

The high temperature decomposition step above 400°C is exclusively due to the release of CO_2, referred to as, high temperature carbonate in the following. The distinction of three different decomposition steps agrees with DTA/TG measurements. The decomposition steps of the 0 min aged precipitate compared to the 120 min precipitate differ in the onset temperature of the first and second step as well as the total amount of the water and CO_2 released. The calcination temperature affects the catalytic activity of Cu/ZnO catalysts. W.H. Cheng et al. [66] reported an abrupt decrease in methanol decomposition activity of Cu/ZnO catalysts prepared by co-precipitated Cu,Zn hydroxy carbonates calcined above 400°C. Similar trends were observed in the methanol synthesis activity of Cu/ZnO catalysts calcined above 400°C [Thesis, B.Bems]. In general, thermal decomposition of Cu based hydroxycarbonates at 330°C (3h) result in the most active Cu/ZnO catalyst. Hence, a significant amount of residual carbonate (HT-CO_3) remains in the precursor after calcinations, but the effect of residual carbonates on the structure and activity of the resulting catalyst remains unclear. Several suggestions were made concerning the origin of the HT-CO_3. In the literature the HT-CO_3 species is attributed to a final decomposition step of aurichalcite forming an oxo-carbonate [67] or stem from Zn centers in rosasite [68]. However, crystalline aurichalcite exhibits only one sharp decomposition step at 400°C [17], and thus, the HT-CO_3 cannot be attributed to an inherent feature of aurichalcite. Furthermore, 120 min ageing of co-precipitated Cu,Zn hydyroxycarbonates (molar ratio Cu to Zn 70/30) results in a precursor mixture of 80% rosasite and 20% aurichalcite. If the HT-CO_3 was attributed to the decomposition of an oxo-carbonate stemming from aurichalcite, a release of 7% CO_2 relative to the overall CO_2 release during decomposition would be expected. However, 25% CO_2 were

calculated during final decomposition of a 120 min aged precipitate (Figure 22 b). Recent investigations attributed the HT-CO_3 species to aurichalcite and more directly to its progenitor, the hydroxy-rich amorphous phase [17]. Composite or core-shell particles formed by dissolution/re-precipitation processes at the surface of aurichalcite were proposed.

The amount of the HT-CO_3 relative to the overall amount of CO_2 evolving during thermal decomposition is depicted as a function of ageing in Figure 22 b. While the amount of HT-CO_3 increases significantly from 42 to 30 % in a time period of 30 min ageing, only a slight decrease from 30 to 25 % was observed during ageing between 30 and 120 min. The slight decrease of the HT-CO_3 after 30 min ageing corroborates the assumption of a more slowly (delayed) crystallization of the amorphous progenitor of aurichalcite compared to rosasite (chapter 4.2, UV-Vis in solution). An incomplete crystallization of the amorphous progenitor of aurichalcite after 30 min ageing results in progressive dissolution-renucleation processes of the amorphous progenitors, and, thus, in a continuous decrease of HT-CO_3 species as a function of ageing. Here, the effect of ageing on the formation of CuO during thermal decomposition of hydroxycarbonate precipitates is investigated using in situ XRD. Furthermore, a UV-Vis/XAS/MS experiment during calcination of a non-aged precursor was performed using the new UV-Vis/XAS cell.

4.3.2 Results and Discussion

4.3.2.1 In situ XRD

The in situ XRD experiments were performed during calcination under the conditions described in chapter 2.1.2. The integral breadth of the CuO 111 peak and the corresponding CO_2 evolution during thermal decomposition of washed and dried 0 min aged and 120 min aged hydroxycarbonate precipitates is shown in Figure 23. Qualitatively, the CO_2 profile measured in the XRD cell agrees with the gas phase evolution obtained from TG measurements (Figure 22b). Both, the carbonate decomposition step below and above 400 °C are reflected in the CO_2 profile. The gas phase evolution of CO_2 during calcination can thus be used as indicator for the reliability of the XRD data. The CuO 111 peak appears at calcination temperatures of 340 °C and 430 °C for the non aged and 120 min aged precipitates, respectively.

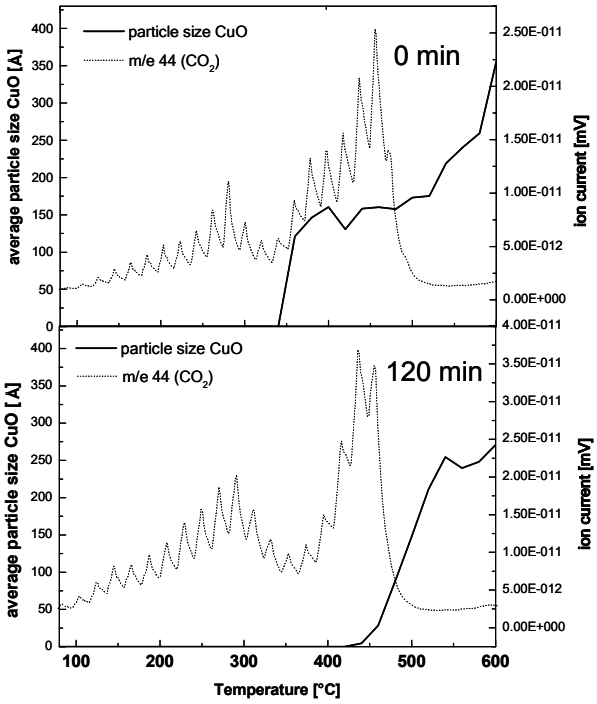

Figure 23 Average particle size of CuO (111 peak) and CO_2 release during thermal decomposition (RT-600 °C) of a 0 min and 120 min aged hydroxycarbonate precipitates.

Surprisingly, CuO formation starts at the second CO_2 decompositon step (HT-CO_3). The delayed onset of CuO formation compared to precursors calcined in static air at 330°C (3 h) in a furnace, can be ascribed to the shorter isothermal periods during the in situ XRD experiment. However, the two differently aged precursors deviate in the onset temperature of CuO formation during calcination. The earlier onset of CuO formation and the rapid increase of the CuO particle size of the non-aged precipitate (330°C) compared to the longer-aged precipitate (430°C), clearly reflect the memory of the material and the dominant influence of the preparation (i.e. ageing). These results predict a larger average CuO particle size of the non-aged precursor compared to the 120 min aged precursor under the calcination conditions described above (330°C, 3h, static air). Additionally, the CuO particle size of both precursors increases with calcination temperature which is in good agreement with the literature [66]. However, W.H. Cheng [66] reported that the resulting loss in surface area cannot be used to explain the decrease in catalytic activity at an intermediate calcination temperature. Hence, additional experiments have to follow in order to elucidate the origin of the residual HT-CO_3 and its effect on the catalytic performance. In the following combined UV-Vis/XAS investigations of structural changes of the precursor during the calcination process is described.

4.3.2.2 In-situ UV-Vis/XAS

A brief overview of experiments performed during calcination using the new combined XAS/UV-Vis cell is given in the following chapter. Combined time-resolved XAS/UV-Vis experiments have to follow including detailed XANES, EXAFS, and UV-Vis analysis. The UV-Vis diffuse reflectance spectra and the corresponding absorbance difference spectra (calculated by subtracting the current spectrum from the first measured one) measured during calcination of a 0 min aged precursor from RT to 600°C (6 K/min) is shown in Figure 24. The characteristic color change of the precursor during calcination from greenish blue to black can be seen in a non-simultaneous increase in absorbance in the visible range of the spectrum accompanied by slight shifts in the band position with maxima at wavelengths of 430 nm and 490 nm. Furthermore, a decrease in the absorbance of the precursor in the UV range (240 nm to 330 nm) is observed at higher decomposition temperatures.

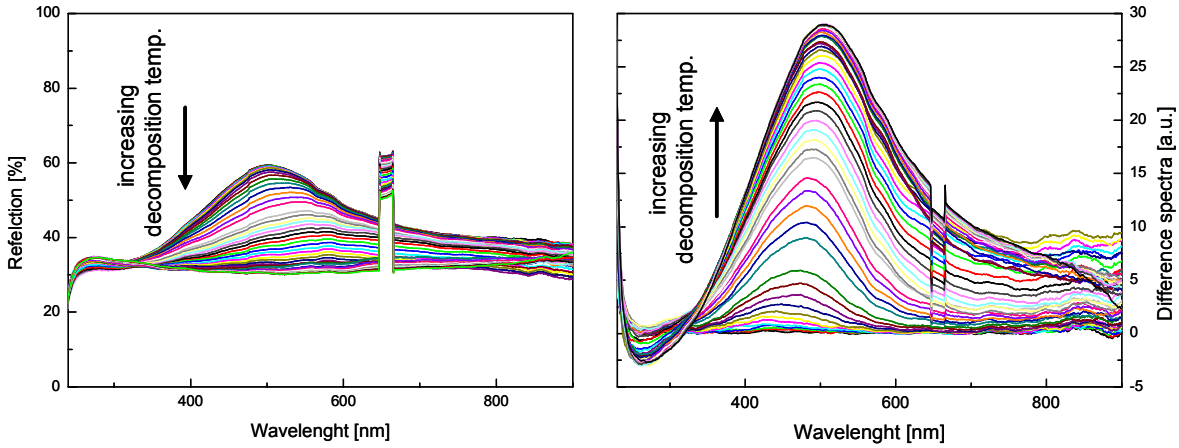

Figure 24 UV-Vis reflection spectra during temperature programmed calcination (RT- 600 °C at 6K/min) of a 0 min aged hydroxycarbonate precursor (a) and the resulting difference spectra calculated by subtracting the current spectrum form the first measured (b)

A detailed analysis of the UV-Vis spectra during temperature programmed calcination of mixed metal hydroxycarbonates will require model experiments using pure metal hydroxycarbonates (aurichacite, rosasite or malachite) in order to reduce the complexity, as well as theoretical calculations of the electronic transitions of aurichalcite/rosasite, and a combined time-resolved XAS/UV-Vis experiment. Qualitatively, the evolution of the

precursor absorbance correlates with the decomposition steps during calcination. Figure 25 shows the reflectance at 490 nm and 260 nm as a function of the calcination temperature of the 0 min aged precursor in comparison to the gas phase evolution of CO_2 and H_2O measured during thermal treatment. The absorbances at 490 nm and 260 nm represent exemplary the reflectance of the precursor in the Vis and the UV range, respectively. The onset of the decrease in reflectance in the Vis range (i.e. increase in absorbance) coincides with the onset of the first decomposition step at ~ 120°C (water release). In addition to the slowed increase in absorbance in the Vis range during the second decomposition step at ~ 220°C (H_2O and CO_2 release) a minor reflectance in the UV range is observed. During the HT-CO_3 decomposition step only a continuous decrease in the UV reflectance of the precursor is observed, whereas the absorbance in the Vis range remains constant. The combined UV-Vis/MS experiment during temperature programmed calcination indicates that the decrease in absorbance in the UV range above 250°C (i.e. increase in reflection) is attributed to the CO_2 decomposition steps. The increase in absorbance in the Vis range can be assigned to H_2O containing decomposition steps. It is assumed that the absorption in the visible range indicates the formation of Cu_2O or CuO (Figure 12) and the decreasing absorption in the UV range can be assigned to the decomposition of CO_3^{2-} stem from aurichalcite or rosasite.

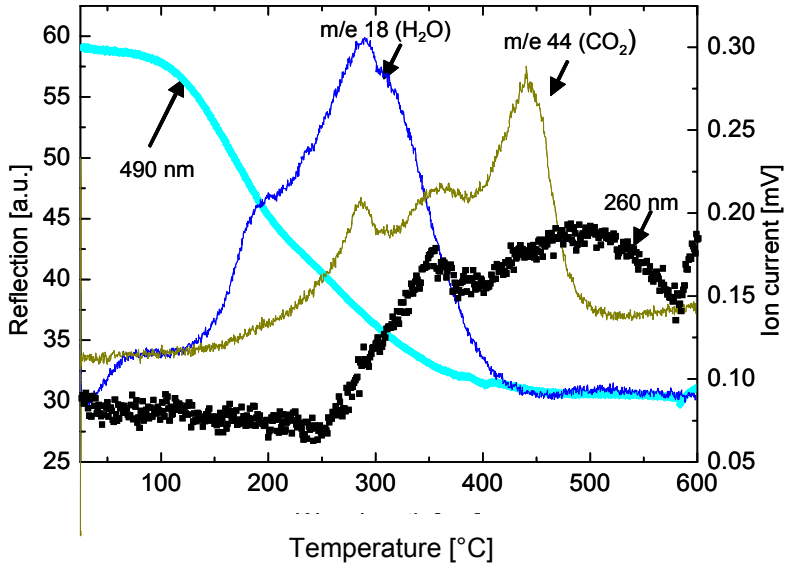

Figure 25 UV-Vis reflection of a 0 min aged precursor at 490 nm and 260 nm and gas phase evolution (CO_2, H_2O) as function of calcination temperature (20 % O_2 ; 80 % He)

The Cu K edge and Zn K edge FT(χ(k)*k^3) measured at room temperature after calcinations of a 0 min aged precursor at 330 °C and 600 °C is depicted in Figure 26. The first peak in the Cu K-edge FT(χ(k)*k^3) attributed to Cu surrounded by oxygen in a square-planar coordination, and the second peak, attributed to the first Cu shell in CuO, remain identical in intensity for a precipitate calcined at 330 °C or 600 °C. Only a decrease in intensity between 2.5 Å and 6 Å for a precursor calcined at 330 °C is observed, which may originate from the superimposition of spectra from a carbonate containing Cu phase and CuO. The damping in the amplitude in the range from 2.5 Å – 6 Å may also originates from an increase in particle size caused by sintering (Figure 23), which can be excluded because of the large particle size of CuO (90 Å calcined at 330 °C and 170 Å calcined at 600 °C) [69].

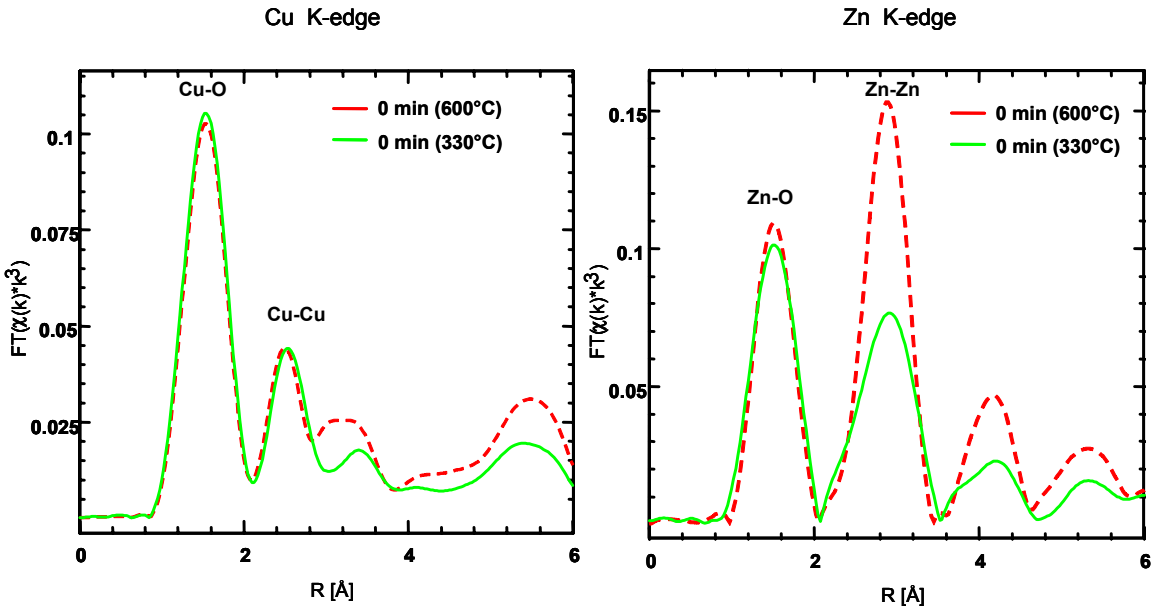

Figure 26 Cu and Zn K edges FT(χ)k*k^3) recorded at room temperature for a 0 min aged precipitate calcined at 330 °C and 660 °C

The first peak in the Zn K edge FT(χ(k)*k^3) is attributed to Zn surrounded by oxygen in a distorted tetrahedral coordination and the second peak is attributed to the first Zn shell in ZnO. The Zn K edge FT(χ(k)*k^3) of the precipitate calcined at 330°C exhibits a strong decrease in intensity of the Zn-Zn shell and in the range from 2 Å – 6 Å. Simulation of the spectrum assuming ZnO reveals strong deviations in the distances and Debye-Waller factors. Although the particle size of ZnO (40 Å calcined at 330°C; 155 Å calcined at 600°C) may account for the decreased intensity of the FT(χ(k)*k^3), the pronounced increase in intensity of the FT(χ(k)*k^3) and the deviations in the distances indicate the defect rich ZnO structure or

less likely the existence of an additional Zn containing phase. The comparison of the Cu and Zn FT(χ(k)*k^3) indicate that the HT-CO_3 is mainly located at Zn centers. It is assumed that the residual carbonate species after calcination at 330 °C is located at the interface of CuO/ZnO and prevents sintering of the oxide particles during reduction. Furthermore, the structural disorder of ZnO observed in the Zn FT(χ(k)*k^3) (Figure 26) indicates an incomplete removal of residual hydroxides or carbonates incorporated in the bulk and/or the presence of oxygen vacancies (ZnO_{1-x}).

4.3.3 Conclusion

The onset temperature of the formation of crystalline CuO during calcination depends strongly on the catalyst composition. The lower onset temperature of the crystallization of CuO from the amorphous precursor compared to the crystalline precursor (Figure 23) clearly demonstrates the “memory” of the material on the calcination treatment. The in situ XRD investigations predict a larger CuO particle size for the amorphous precipitates compared to the crystalline precipitates.

Increasing the calcination temperature results in larger CuO crystallites (sintering). The corresponding loss in surface area may be the origin of the reduced activity of Cu/ZnO catalysts obtained from precursors calcined at temperatures above 350 °C. However, the role of the residual carbonates remaining in the oxide precursor (HT-CO_3) after calcination remains unclear. The HT-CO_3 may serve as growth inhibitor for the oxides [17] or may partially decompose during reduction leading to defect-rich oxide crystallites. The results presented show, that combined XAS/UV-Vis/MS investigations during temperature programmed calcination are a powerful tool to elucidate the origin of the HT-CO_3. Eventually, UV-Vis spectroscopy may add complementary information to the EXAFS (XANES) data and may thus enable to unravel the origin of the deviations in the Zn K-edge FT(χ(k)*k^3) (Figure 26).

4.4 Structure of the CuO/ZnO precursors as function of precipitate ageing

The structure of the CuO/ZnO precursor calcined under the conditions described in chapter 2.6 is investigated as function of precipitate ageing. Figure 27a shows the CuO crystallite size of the calcined precursor determined by line profile analysis of XRD patterns of the CuO/ZnO precursors. A strong decrease in CuO crystallite size with ageing can be seen for the precursors obtained from amorphous precipitates (0 min and 15 min), whereas the CuO crystallite size remains nearly constant for the precursors obtained from crystalline precipitates (30 min and 120 min).

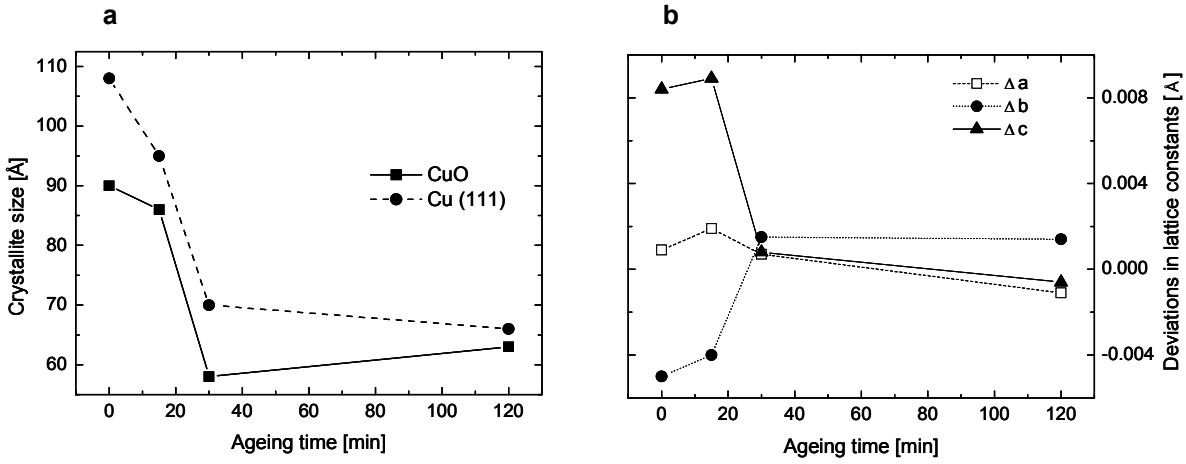

Figure 27 Crystallite size of CuO in CuO/ZnO precursors and of Cu in the reduced Cu/ZnO catalysts as function of precipitate ageing determined from XRD line broadening (a) and deviations in the lattice constants of CuO in CuO/ZnO precursors as function of precipitate ageing (b).

Deviations in the lattice constants of CuO obtained by XRD refinement of a CuO model structure (ICDD-PDF-2: 5-661) to the experimental patterns are depicted in Figure 27 b. For the CuO/ZnO precursors obtained from precipitates aged for 0 min and 15 min, the lattice constants determined deviate significantly from those of ideal CuO. Conversely, only minor deviations in the lattice constants of CuO were observed for the CuO/ZnO precursors obtained from precipitates aged for 30 min and 120 min.

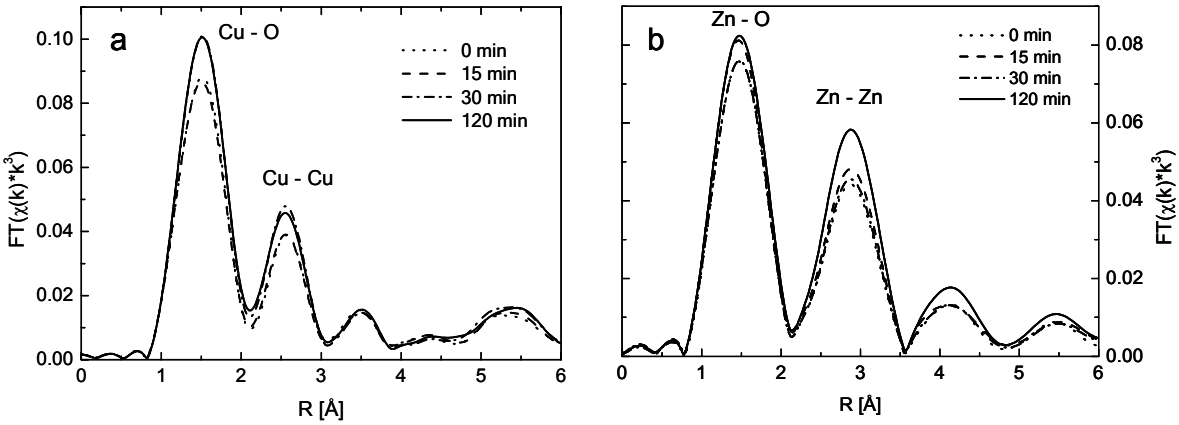

Figure 28 Experimental Cu K edge (a) and Zn K edge (b) FT ($\chi(k)*k^3$) of CuO/ZnO precursors obtained from precipitates aged for 0, 15, 30 and 120 min measured at 300 K in He

The distinct distortion of the CuO short-range structure is also visible in the Cu K edge FT($\chi(k)*k^3$) of the four CuO/ZnO precursors (Figure 28a). The first peak in the FT($\chi(k)*k^3$) which is attributed to Cu surrounded by oxygen in a square-planar coordination and the second peak, which is attributed to the first Cu shell in CuO, exhibit a strong decrease in intensity for the precursors obtained from precipitates aged for 0 min and 15 min.

The Zn K edge FT($\chi(k)*k^3$) reveals a strongly decreased intensity of the first Zn-O shell for the precursors obtained from 0 min and 15 min aged precipitates, which correlates with the observed distortion in the CuO short-range structure for the short aged precipitates. Moreover, the Zn K edge FT($\chi(k)*k^3$) reveals an increased intensity of in the range above 2 Å for the precursors obtained after 120 min ageing, whereas the FT($\chi(k)*k^3$) of the precursors obtained from 0 min, 15min, and 30 min ageing remains nearly constant.

The long-range (Figure 27) and short-range structure (Figure 28) of CuO of the four CuO/ZnO precursors exhibit a characteristic dependence on the crystallization of the initially amorphous precipitates that occurs after about 30 min ageing. The decrease in the CuO crystallite size of the calcined CuO/ZnO precursor is in good agreement with the in situ XRD results during calcination (Figure 23), which predicts a smaller CuO crystallite size obtained from the longer aged precipitates compared to the short aged precipitates. Hence, a similar trend can be assumed for the Cu/ZnO catalysts (e.g. decreasing Cu crystallite size with increasing ageing time, Chapter 5.2.2.1). The CuO lattice constants show a remarkable shift towards that of regular CuO in the CuO/ZnO precursors obtained from precipitates aged for

30 min or 120 min (Figure 27 b). The deviations in the CuO lattice constants of CuO/ZnO precursors obtained from short-aged precipitates (0 min and 15 min) can be assigned to the formation of a Zn-doped CuO ($Cu_{1-x}Zn_xO$). [70, 71]

The defects in the long-range structure of the CuO/ZnO precursors obtained from short-aged precipitates can also be found in the corresponding short-range structure (Figure 28). The first peak in the XAFS FT(χ(k)*k^3) which corresponds to four oxygen atoms in a square-planar coordination and the second peak, which corresponds to the first Cu shell in CuO, (Figure 28a) exhibit a strong increase in intensity for the precursors obtained from precipitates aged for 30 min and 120 min. A similar increase is also visible in the FT(χ(k)*k^3) of the corresponding reduced Cu/ZnO catalysts (Figure 41). The increase in FT(χ(k)*k^3) amplitude of the CuO/ZnO precursor and the Cu/ZnO catalysts may be explained by (i) an unlikely decrease in the Debye-Waller factor, which at least for the Cu/ZnO catalysts is in contrast to the increase in microstrain detected by XRD and NMR (Chapter 5.2), (ii) an increase in the apparent coordination number because of changes in crystallite size, which can be excluded because of the rather large crystallites (> 60 Å [69]) and the overall decrease in crystallite size with ageing, or most likely (iii) a decreasing amount of Zn in the CuO phase and the resulting copper catalyst. Hence, the deviations in the "real" structure of CuO in the calcined precursors obtained from short-aged precipitates (Figure 27 b and Figure 28 a) are caused by Zn centers in the CuO structure. Similarly, Zn in the calcined CuO/ZnO precursors was proposed for Cu/ZnO catalysts with various Cu to Zn ratios [36].

The distinct distortion in the CuO short-range structure of the CuO/ZnO precursors obtained from 0 and 15 min aged precipitates is also visible in the Zn-O shell of the Zn K-edge FT(χ(k)*k^3) (Figure 28 b). However, comparing the 30 min and 120 min aged precursor the increased intensity in the Zn K-edge FT(χ(k)*k^3) in the range between 2 Å and 6 Å indicates that the precipitates still undergo chemical/microstructural changes after 30 min ageing in the mother liquor. Assuming that the presence of residual HT-CO_3 in the CuO/ZnO precursor is visible in the range from 2 Å to 6 Å in the Zn K-edge FT(χ(k)*k^3) (Figure 26) and that the amount of the HT-CO_3 species can be attributed to dissolution re-crystallization processes of the amorphous progenitor of aurichalcite (Chapter 4.3.1), the Zn K-edge FT(χ(k)*k^3) support the result of a delayed crystallization of the amorphous progenitor of aurichalcite during ageing (UV-Vis; Chapter 4.2.2).

4.5 Reduction of CuO/ZnO precursors as function of precipitate ageing

4.5.1 Results

4.5.1.1 TG/MS (TPR)

The evolution of the water gas phase concentration during a temperature programmed reduction of a thermo-gravimetric experiment (TG/MS) and the consumption of hydrogen during conventional temperature-programmed reduction (TPR) of two CuO/ZnO precursors (0 min and 120 min ageing) in the temperature range from 300 K to 523 K is depicted in Figure 29.

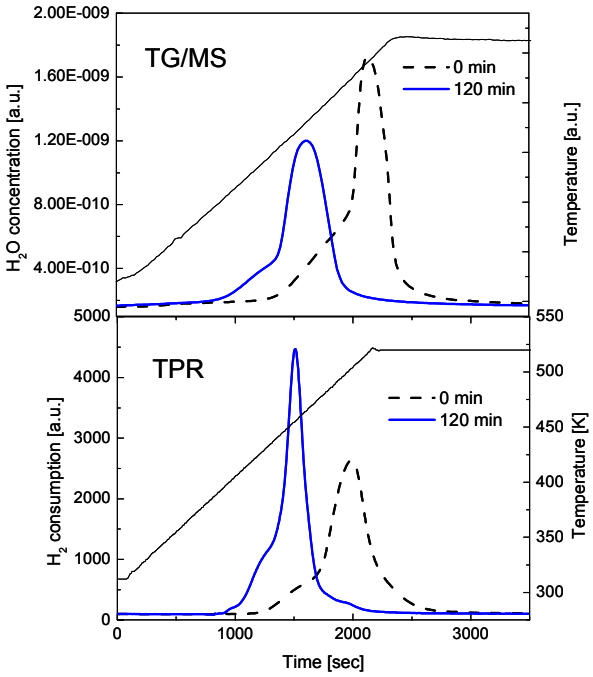

Figure 29 H_2O gas phase concentration during temperature-programmed reduction (TG/MS) and hydrogen consumption during conventional temperature-programmed reduction (TPR) of the two CuO/ZnO precursors (0 min and 120 min ageing) in the temperature range from 300K to 523 K (heating ramp 6 K/min).

Both TPR traces exhibit characteristic shoulders left to the main reduction peak. Compared to the narrow reduction peak at 454 K of the CuO/ZnO precursor obtained from a 120 min aged precipitate, the TPR traces of the CuO/ZnO precursor obtained from a non-aged precipitate is much broader and shifted to higher reduction temperatures (503 K). Qualitatively, the H_2O

evolution during temperature-programmed reduction measured by TG/MS is in good agreement with the onset temperature of the TPR reduction peaks.

The onset temperature of the relative mass loss during reduction of the four precursors coincides with the shift of the TPR peak to higher reduction temperatures with increasing precipitate ageing time (Figure 30). The difference in the mass loss during temperature programmed reduction of the CuO/ZnO precursors obtained from precipitates aged for 120 min and 0 min (Figure 30) is partly caused by a different composition of the materials. A quantitative determination of the Cu content in the catalyst obtained from the copper K edge jump and zinc K edge jump exhibits a decrease in copper content from 75 mol-% (0 min ageing) to 73 mol-% copper (120 min ageing) with respect to the metals.

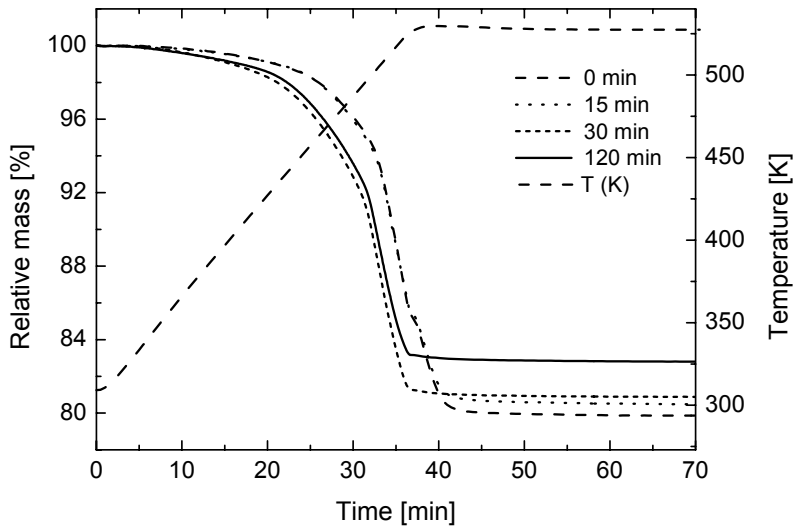

Figure 30 Weight loss from thermogravimetric measurements during temperature programmed reduction (300 K to 523 K; 6 K/min) of CuO/ZnO precursors in 2% H_2 as function of precipitate ageing.

Moreover, deviations in the mass loss of the four precursors during reduction were observed because of different amounts of residual nitrates and carbonates in the materials. The evolution of the gas phase composition during TPR of CuO/ZnO obtained from precursors aged for less than 30 min clearly indicates the decomposition of residual nitrates (NO, m/e = 30) and carbonates (CO_2, m/e = 44). The amount of residual carbonates and nitrates in the precursors decreases with increasing ageing time. Residual copper oxide phases as a result of

an incomplete reduction of the CuO/ZnO precursors were not detected (detection limit of XAFS analysis ~1 %).

4.5.1.2 XAS

In order to assign the TPR peaks to chemical phases present during reduction, time-resolved XANES measurements were performed. The evolution of the Cu K edge XANES spectra during temperature-programmed reduction of a CuO/ZnO precursor (15 min ageing) is shown in Figure 31 a. A transition from the characteristic near-edge structure of CuO to that of Cu metal can be seen. PCA yielded three reference compounds (CuO, Cu_2O, Cu) required to reconstruct the set of experimental XANES spectra in Figure 31 a. Target transformed XANES spectra of CuO and Cu obtained by precipitation of malachite ($Cu_2(OH)_2(CO_3)$), followed by calcination and reduction are in good agreement with the first and the last experimental spectrum in Figure 31 a, respectively. Differences between the Cu K edge spectrum of commercial Cu_2O and the corresponding target-transformed spectrum can be attributed to a different crystallite size and the occurrence of highly disordered Cu_2O during reduction.

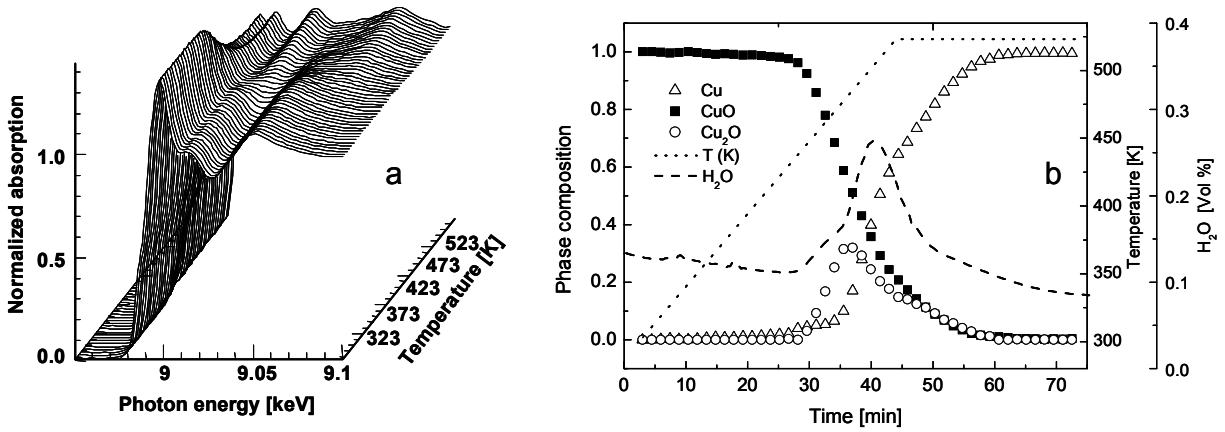

Figure 31 (a) Evolution of Cu K edge XANES spectra during temperature programmed reduction (300 K to 523 K; 6 K/min) of a CuO/ZnO precursor (15 min aged precipitate) in 2% H_2 and (b) the corresponding phase composition (CuO, Cu_2O, and Cu) together with the evolution of H_2O during reduction.

A quantitative phase analysis was obtained from a least-squares fit of a linear combination of the Cu and CuO reference spectra and the target transformed spectra of Cu_2O to each

experimental XANES spectrum measured during reduction of the CuO/ZnO precursor. The resulting evolution of the phase composition during reduction of CuO/ZnO (15 min ageing) and the corresponding H_2O evolution are shown in Figure 31 b. A sequential reduction pathway from CuO to intermediate Cu_2O and, eventually, to Cu metal was found, which is in good agreement with previous investigations [36,72]. The asymmetric profile at the end of the reduction is caused by a declining degree of reduction under isothermal conditions.

The evolution of the CuO content of the four CuO/ZnO precursors during TPR is depicted in Figure 32. With increasing precipitate ageing time the onset of reduction is lowered from 462 K (0 min and 15 min) to 444 K (30 min and 120 min). Thermogravimetric experiments under the same reduction condition reveal identical shifts in the onset temperature (Figure 30).

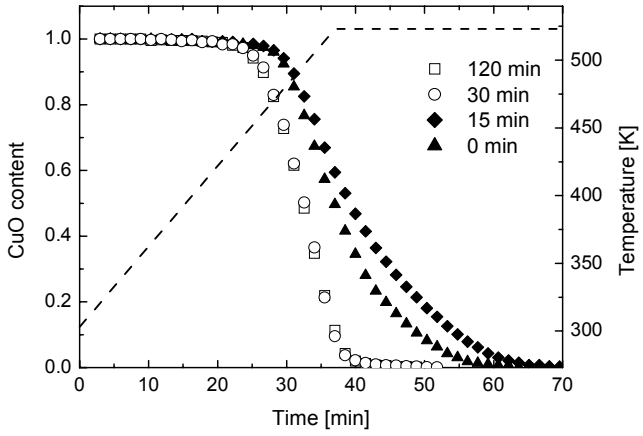

Figure 32 Evolution of CuO content from XAS measurements during temperature-programmed reduction (300 K to 523 K; 6 K/min) of CuO/ZnO precursors in 2% H_2 as a function of precipitate ageing.

In Figure 33 the Zn K edge FT(χ(k)*k^3) of the calcined precursor and the reduced catalyst obtained from non-aged and 120 min aged precipitates and a ZnO reference prepared by calcination of precipitated hydrozincite ($Zn_5(OH)_6(CO_3)_2$) are depicted. The Zn K edge FT(χ(k)*k^3) of both CuO/ZnO precursors (i.e. 0 min and 120 min) exhibit a considerable decrease in intensity compared to the FT(χ(k)*k^3) of the reduced Cu/ZnO catalyst. Moreover, a significant decrease in the intensity of the Zn FT(χ(k)*k^3) in the range below 2 Å for both Cu/ZnO catalysts is observed compared to that of ZnO, which confirms the defect rich character of ZnO after the reduction of the calcined precursor.

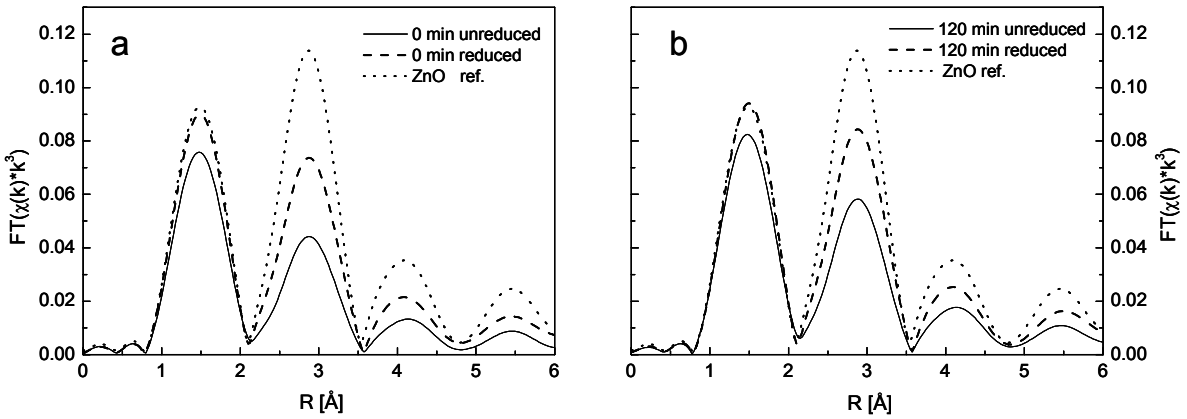

Figure 33 Zn K edges FT(χ(k)*k^3) of CuO/ZnO precursor and the Cu/ZnO catalyst obtained from precipitates aged for 0 min (a) and 120 min (b), and ZnO as reference obtained from calcined $Zn_5(OH)_6(CO_3)_2$ measured at 300 K in He

4.5.1.3 XPS (NEXAFS)

The near-surface structures (6 monolayers) of the CuO/ZnO precursor and the reduced Cu/ZnO catalyst in hydrogen and methanol steam reforming gas atmosphere were investigated using near edge X-ray absorption fine structure (NEXAFS) spectroscopy. The corresponding Cu L_3 and Zn L_3 NEXAFS spectra of the CuO/ZnO precursor and the Cu/ZnO catalyst obtained from precipitates aged for 15 min and 30 min are depicted in Figure 34.

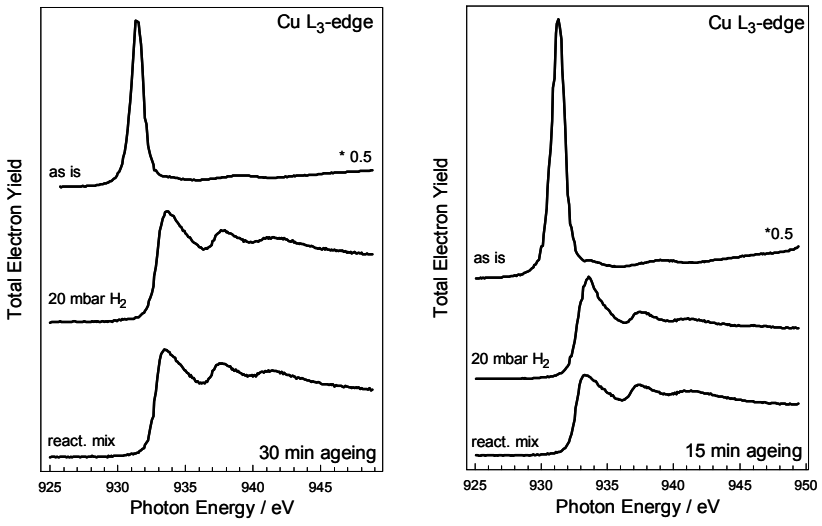

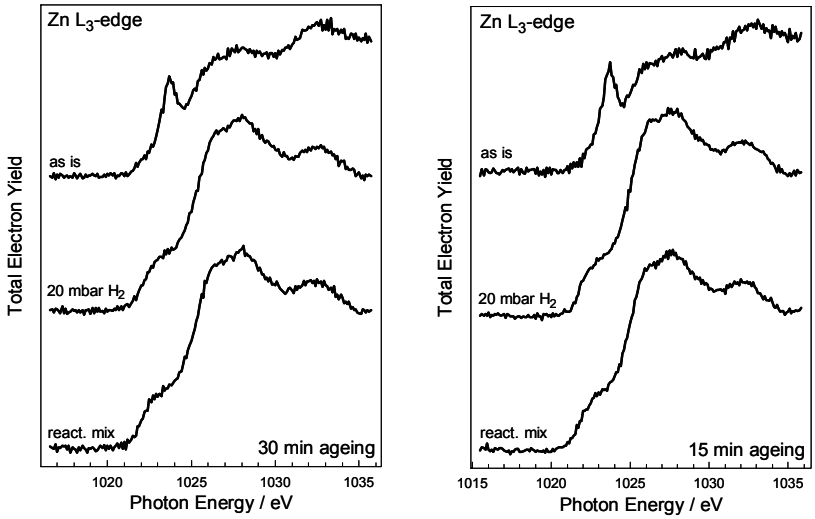

Figure 34 Cu L_3 edge and Zn L_3 edge NEXAFS spectrum of the CuO/ZnO precursor (as is), the reduced Cu/ZnO catalyst (20 mbar H_2), and the catalyst in methanol steam reforming gas mixture (react. mix.) obtained from precipitates aged for 15 min (right) and 30 min (left).

From comparing the CuO/ZnO precursor with the reduced Cu/ZnO catalyst, characteristic changes of the NEXAFS for both edges (i.e. Cu L_3 and Zn L_3) were observed. Converseley, the Cu L_3 and Zn L_3 NEXFAS spectra measured in hydrogen and steam reforming gas mixture roughly remain similar. The Zn L_3 NEXAFS indicates the presence of a zinc species different to ZnO by the occurrence of a distinct resonance at the onset of the absorption edge (Figure 34). In order to assign the NEXAFS spectra of the precursor/catalyst to chemical phases several reference spectra were recorded. In Figure 35 Cu L_3 and Zn L_3 NEXAFS spectra of CuO/ZnO precursor and Cu/ZnO catalyst obtained from precipitates aged for 30 min, are compared with suitable reference spectra (Cu_2O, CuO, Cu, ZnO and $Zn_5(OH)_6(CO_3)_2$). The Cu L_3 NEXAFS spectrum of the CuO/ZnO precursor correspond to CuO, while the Cu L_3-NEXAFS spectrum of the reduced catalyst correspond to Cu. The Zn L_3 edge NEXAFS spectrum of the calcined precursors deviates significantly from that of ideal ZnO (Figure 35). The distinct pre-edge feature (indicated by the arrow) is also reflected in the spectra of pure zinc hydroxy carbonates.

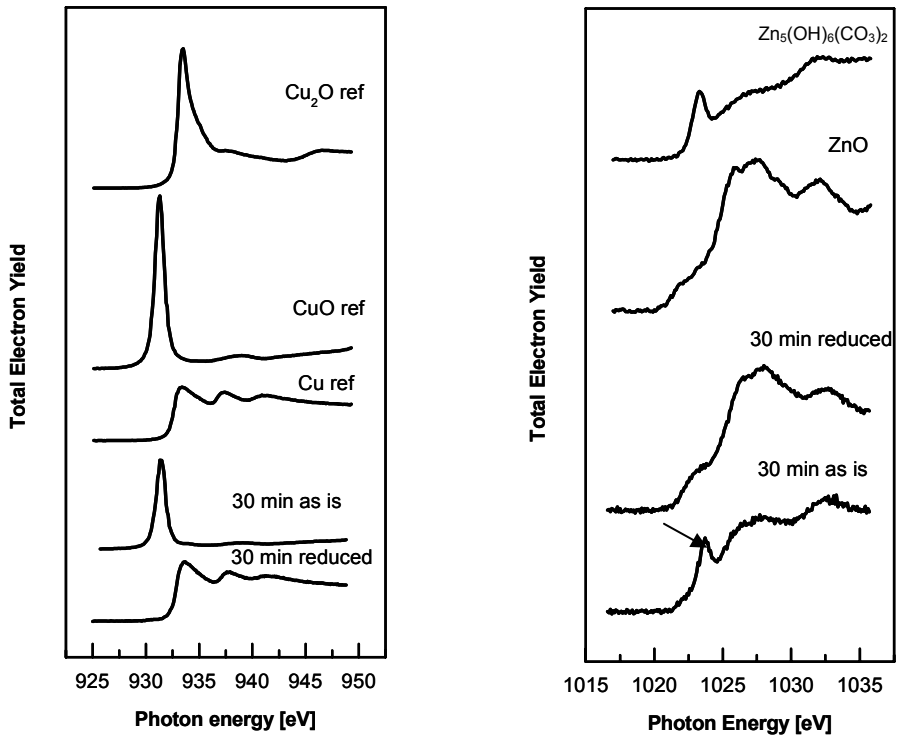

Figure 35 Cu L_3 and Zn L_3 NEXAFS spectrum of the CuO/ZnO precursor (as is) and the reduced Cu/ZnO catalyst (reduced) obtained from a precipitate aged for 30 min, a $Zn_5(OH)_6(CO_3)_2$ reference, ZnO obtained from calcined $Zn_5(OH)_6(CO_3)_2$, Cu_2O, CuO, and Cu

Quantitative phase analysis obtained from a least-squares fit of a linear combination of the $Zn_5(OH)_6(CO_3)_2$ and ZnO reference spectra to the experimental Zn NEXAFS spectra of the calcined precursor result in a phase composition of 75 % carbonate species and 25 % ZnO. For the CuO/ZnO precursor obtained from precipitates aged for 15 min a phase composition of 87 % carbonate species and 23 % ZnO is necessary to simulate the Zn L_3-edge NEXAFS. The carbonate species decomposed during the reduction of the both catalyst in H_2 and a NEXAFS spectrum typical for ZnO was obtained.

4.5.2 Discussion

The four Cu/ZnO materials studied can be separated into two groups with respect to the onset temperature of reduction of the corresponding CuO/ZnO precursors (Figure 32). CuO/ZnO precursors obtained from precipitates aged for 0 min and 15 min exhibit a higher reduction temperature (~ 450 K), compared to precursors obtained from precipitates aged for 30 min

and 120 min (~ 500 K). The lower reduction temperature of the precursors obtained from long-aged precipitates compared to those obtained from short-aged precipitates is because of the smaller CuO crystallite size (~60 Å and ~90 Å, respectively (Figure 27), and eventually the more homogeneous microstructure (Chapter 5.2.2.3; TEM). The increase in crystallite size during reduction of the CuO/ZnO precursor (~90 Å, 0 min ageing) to the corresponding Cu/ZnO catalyst (~110 Å, 0 min) indicates a pronounced sintering of the copper particles. This lowered stability towards sintering is consistent with the larger amount of isolated copper particles and the diminished interface between Cu and ZnO in the catalysts obtained from short-aged precipitates [73]. Conversely, the more homogenous particle size distribution and the improved interface between copper and zinc oxide in the Cu/ZnO catalysts obtained from long-aged precipitates increase the degree of dispersion and prevent sintering of the copper particles during reduction (~65 Å for Cu and CuO). A detailed description of the microstructural modifications of the four Cu/ZnO catalysts using TEM is given in chapter 5.2.2.3.

Conventional TPR also shows clear differences between CuO/ZnO precursors obtained from amorphous (0 min ageing) or crystalline (120 min ageing) precipitates (Figure 29). The quantitative XANES analysis (Figure 31) yields a sequential reduction according to CuO → Cu_2O → Cu. Similar investigations concerning the reduction of CuO in the CuO/ZnO/ZrO_2 system [74] and the reduction of CuO and Cu_2O in H_2 [75] are in good agreement with our results. Furthermore, it can be seen that the H_2O evolution observed during the in situ XAFS experiments correlates well with the phase composition during reduction (Figure 31 b) and the TPR measurements (Figure 29). The first maximum in the H_2O evolution indicates the maximum amount of the intermediate Cu_2O phase, while the second maximum correlates with the inflection point in Cu metal formation. The narrow TPR peak of the aged precursor (Figure 29) is in very good agreement with the homogeneous microstructure of the corresponding single-phase Cu/ZnO catalyst. A heterogeneous microstructure of the Cu/ZnO catalysts obtained from non-aged precipitates can already be inferred from the broad high-temperature TPR peak of the corresponding CuO/ZnO precursor. The characteristic grouping of the CuO/ZnO precursors obtained from short-aged (0 and 15 min) and long-aged (30 and 120 min) precipitates clearly reflects the dominant influence of the preparation (i.e. ageing procedure) not only on the structure of the precipitate but also on the structure of the CuO/ZnO precursors (Figure 27 and Figure 28), the reduction behavior (Figure 29 and Figure 32), and, eventually, the resulting Cu/ZnO catalyst.

The bulk structural (Figure 30, Figure 33) and surface structural (Figure 34, Figure 35) investigations clearly indicate the presence of residual carbonate species in the four CuO/ZnO precursors. The amount of the residual carbonate in the CuO/ZnO precursor decreases with increasing ageing time. A complete decomposition of the carbonate species during reduction in the near-surface region (Figure 34, Zn L_3-NEXAFS) was observed. The first peak in the Zn K edge FT(χ(k)*k^3) which is attributed to Zn surrounded by oxygen in a tetrahedral coordination (Figure 33) can be used as indicator for the presence of residual carbonates in the ZnO bulk. The similar intensity in the first shell of the Zn K edge FT(χ(k)*k^3) comparing the ZnO reference with the reduced catalysts (0 and 120 min) indicates a complete decomposition of residual carbonates in the bulk during reduction. The reduction induced carbonate decomposition results in structurally disordered ZnO in the range from 2 Å to 6 Å (Figure 33). Additionally, the increasing average particle size of ZnO induced by the reduction (52 Å to 64 Å $\rightarrow$ 0 min, 40 Å to 64 Å $\rightarrow$ 120 min), may contribute to the observed increased intensity of the Zn K-edge FT(χ(k)*k^3) after reduction. Gas phase analysis comparing the amount of CO_2 evolving during reduction to the amount of residual carbonate (HT-CO_3) in the precursor after calcinations at 330 °C have to follow in order to quantify the degree of carbonate decomposition during reduction. The reduction induced decomposition of residual carbonates may be caused by the reduction of surface near Cu^{2+} species dissolved in the ZnO matrix [76, 77].

5 Cu/ZnO catalysts as function of precipitate ageing

The strong influence of precipitate ageing of the precursor on the catalytic activity of the resulting catalysts has already been described in the literature. [17, 39, 40] A strong increase in the activity of catalysts obtained from precipitated precursors that were aged for more than 30 min in the mother liquor was found in comparison to the non-aged precursors. However, the corresponding structure-activity relationships remained unclear.

5.1 Methanol steam reforming activity

The effect of precipitate ageing on the methanol steam reforming activity of the resulting Cu/ZnO catalysts was investigated with in situ XAS/MS and corroborated with catalytic measurements in a tubular stainless steel reactor. The H_2 production rate determined in the in situ XAS cell and the methanol conversion determined in the tubular stainless steel reactor as a function of ageing time are compared in Figure 36.

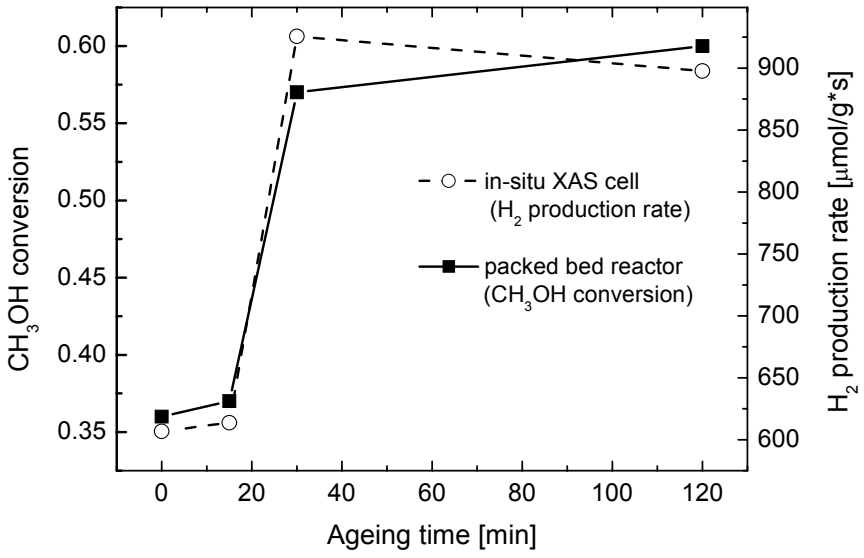

Figure 36 Methanol steam reforming activity of Cu/ZnO catalysts at 523 K as a function of precipitate ageing. The methanol conversion determined in a packed bed reactor is depicted in comparison to the H_2 production rate obtained during the in situ XAS experiment.

The activity of the Cu/ZnO catalysts strongly increases between 15 min and 30 min ageing time from initially 36 % methanol conversion (600 µmol/g*s H_2 prod. rate; 15 min ageing) to 60 % conversion (900 µmol/g*s H_2 prod. rate; 30 min ageing). The same evolution of the methanol steam reforming activity of the Cu/ZnO catalysts as a function of ageing time was found for the in situ XRD experiments. The good agreement between the performance measured in the in situ XAS cell and the tubular reactor (Figure 36) indicates that the structural data obtained from in situ XAS experiments under conditions of differential conversion (~ 10 %) permit deducing reliable structure-activity relationships.

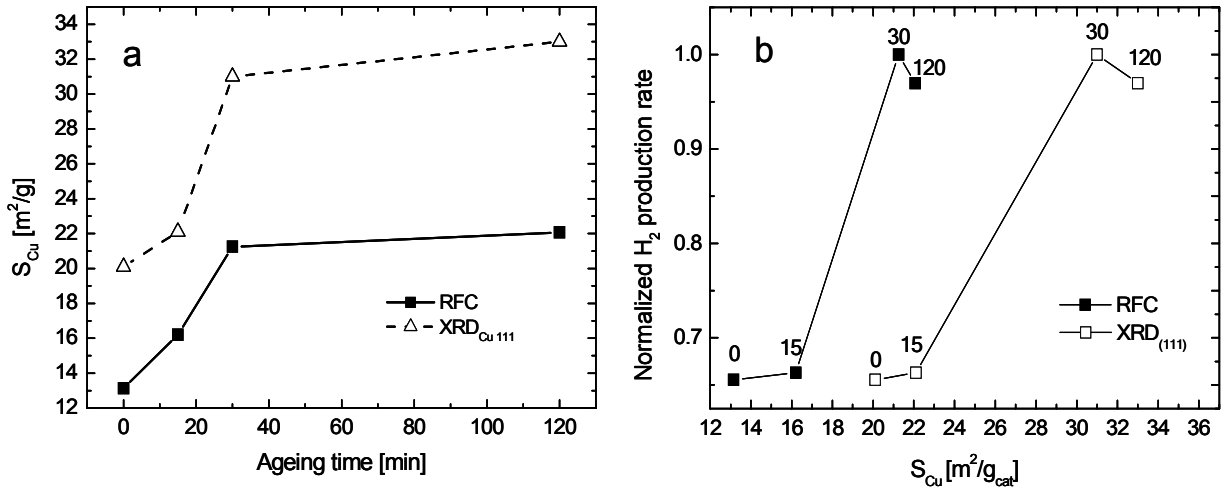

Figure 37 (a) Specific copper surface area of the Cu/ZnO catalyst as a function of precursor ageing determined by N_2O titration and estimated from the XRD copper particle size (Figure 26, Cu 111). (b) Normalized H_2 production rate according to Figure 6 as a function of the specific copper surface area.

The specific copper surface area as determined by N_2O titration is compared to that calculated from the copper crystallite size (XRD) assuming spherical particles (Figure 37). Apparently, an increasing ageing time results in an increase in the Cu surface area from initially 13 m^2/g after 0 min ageing (20 m^2/g from XRD) to 21 m^2/g after 120 min ageing (33 m^2/g from XRD). Both methods reveal similar trends in the evolution of the Cu surface area as a function of precipitate ageing. Cu/ZnO support interactions that reduce the accessible Cu surface area and a non-spherical morphology of the Cu particles may account for the deviations in the Cu surface areas obtained, in addition to a bi-modal particle size distribution or re-oxidation of partially reduced ZnO [69]. For comparison, the normalized H_2 production rates measured

during the in situ XAS measurements as a function of the specific Cu surface area are depicted in Figure 37 b. The H_2 production rate is normalized to the maximum activity of the most active catalyst in the steam reforming of methanol (30 min ageing). A non-linear correlation of the normalized activity and the Cu surface area is observed.

5.2 Microstructure of Cu/ZnO catalysts

5.2.1 Introduction

Recent investigations have shown that differently prepared Cu/ZnO catalysts may possess different active specific copper surfaces and, thus, exhibit additional microstructural factors contributing to the correlation between surface area and catalyst performance [78,79]. Klier proposed that Cu^+ species dissolved in ZnO enhanced the catalytic activity for methanol synthesis [59]. Based on surface investigations of model catalysts with Zn-deposited on Cu 111 surfaces, Fujitani et al. [80] suggested that a metallic Cu-Zn surface alloy is the catalytically active species for methanol synthesis. In addition to the alloying effect, dynamical morphology changes of the Cu particles may be caused by changes in the reduction potential of the gas phase (wetting /non-wetting) [81,86]. Furthermore, it is assumed that the methanol synthesis activity is enhanced by hydrogen spill-over from ZnO which acts as a reservoir of adsorbed hydrogen [82]. Apparently, ZnO not only increases the dispersion of the copper particles and prevents sintering. However, the synergistic effect of Cu and ZnO and the nature of the active sites remain to be elucidated.

Here, complementary bulk methods are employed to investigate the long-range order (in situ X-ray diffraction) and the short-range order (in situ X-ray absorption spectroscopy and ex situ nuclear magnetic resonance spectroscopy). Additionally, high resolution transmission electron microscopy has been performed on the reduced Cu/ZnO catalyst to elucidate the morphology and microstructure of the Cu and ZnO crystallites. A structural model of the active Cu/ZnO catalyst as a function of precipitate ageing and its influence on the catalytic activity is proposed.

5.2.2 Results

5.2.2.1 In-situ XRD

Figure 38 depicts the X-ray diffraction patterns of two Cu/ZnO catalysts (0 min and 120 min ageing) measured under methanol steam reforming conditions at 523 K. Quantitative phase analysis of the of the in-situ XRD patterns of the four Cu/ZnO catalysts (0, 15, 30, 120 min) revealed a phase composition of 68 mol-% copper and 32 mol-% zinc oxide. No significant differences in the phase composition of the active Cu/ZnO catalysts were observed, while the individual copper diffraction lines in each pattern exhibit significant differences in their profiles.

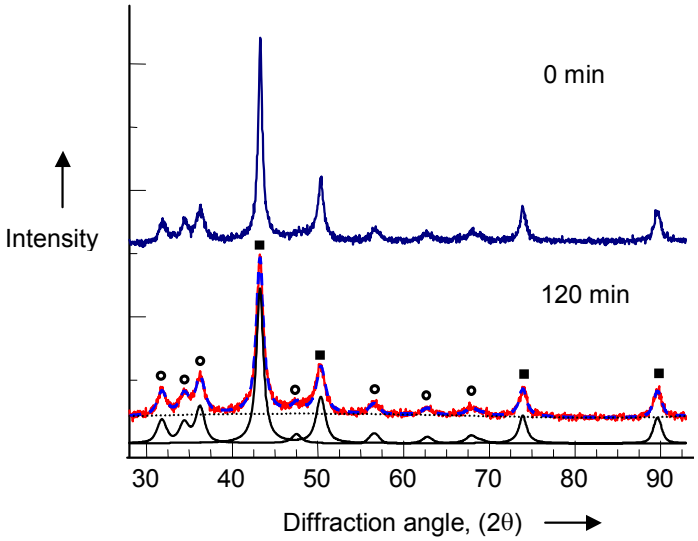

Figure 38 In situ X-ray powder diffraction patterns of two Cu/ZnO catalysts (▪ Cu phase; ○ Zn phase) obtained from precursors aged for 0 min and 120 min measured at 523 K under methanol steam reforming conditions. The Pawley method was employed to simulate the experimental patterns by a sum of profile functions and a background polynomial.

Microstructural changes of the active Cu/ZnO catalyst under working conditions were elucidated by a detailed line profile analysis of the X-ray diffraction patterns. Both particle size and microstrain yield a symmetric line broadening in the corresponding X-ray diffraction pattern. Based on an analysis of the Cu 111 line profile as a function of precipitate ageing, a decrease of the copper crystallite size from initially 110 Å (0 min ageing) to 70 Å (120 min ageing) (Figure 39b) is accompanied by an increase in copper microstrain from initially

0.09% after 0 min ageing to 0.25% after 120 min ageing (Figure 39a). In comparison, copper particles obtained from the reduction of CuO (obtained from the calcination of malachite, $Cu_2(OH)_2(CO_3)$) exhibited a particle size of 300 Å and a microstrain of only 0.06 %.

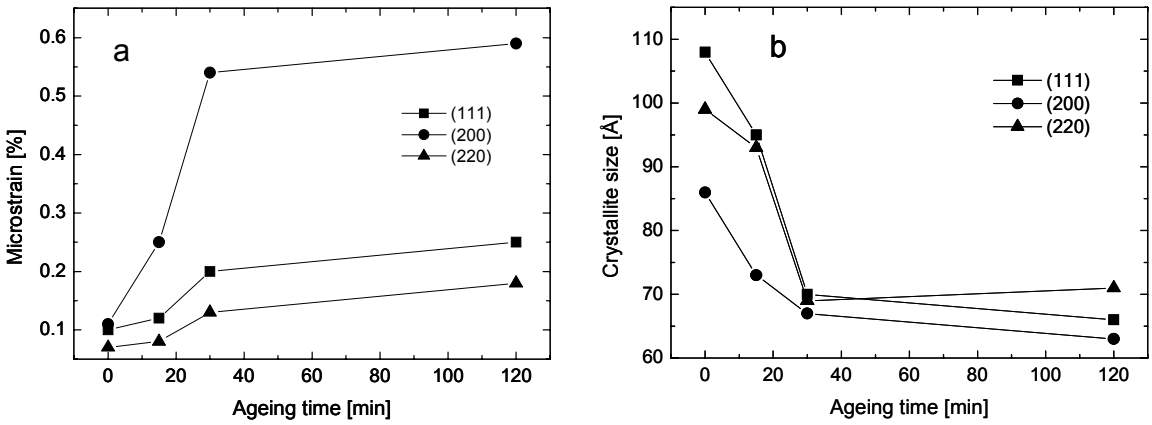

Figure 39 (a) Copper microstrain (b) and crystallite size as function of precipitate ageing determined from the Cu 111, 200, and 220 XRD lines measured at 523 K of Cu/ZnO catalysts under methanol steam reforming reaction conditions.

Crystallite size and microstrain obtained from the analysis of three different copper diffraction lines (111, 200, 220) as function of precipitate ageing is shown in Figure 39a and 39b. Distinct deviations in both crystallite size and microstrain between the different copper lattice planes can be seen. The Cu/ZnO samples analyzed here exhibited a preferred orientation in the [111] direction and a maximum in microstrain in the [100] direction. Nevertheless, a decrease in crystallite size and an increase in microstrain as a function of precipitate ageing were observed for all individual copper diffraction lines. A Williamson-Hall plot based on the XRD patterns of the four Cu/ZnO catalysts confirmed the strong anisotropy (non-linearity between β^* and d^*) in the Cu/ZnO catalysts visible in Figure 39. Hence, the crystallite size and the microstrain had to be determined by analyzing individual X-ray diffraction lines.

5.2.2.2 NMR

In order to corroborate the in situ X-ray diffraction experiments, ex situ NMR investigations of the various Cu/ZnO catalysts were performed. Similar to X-ray diffraction line broadening, the line profile and breadth of the ^{63}Cu NMR signal is determined by the crystallite size and

microstrain of the copper particles [83,84]. Since the NMR line width is determined by the spin-spin relaxation time (chapter 2.3.1) which depends on the number of neighbors near a nucleus, one can expect that an increasing number of less coordinated surface nuclei compared to the bulk nuclei is associated with a distribution of relaxation times (i.e. line broadening). Conversely, for ^{63}Cu and ^{65}Cu there should be no electrical field gradients (I=3/2) in crystalline copper metal due to the cubic symmetry of the copper site. Strain or other defects destroy the symmetry in the neighborhood of the observed nuclei and result in electrical field gradients detectable using NMR spectra. Hence, large and highly ordered copper crystallites result in small and symmetric NMR lines. A decreasing copper crystallite size leads to symmetric NMR line broadening, whereas an increasing microstrain results in asymmetric line profiles or even additional NMR lines.

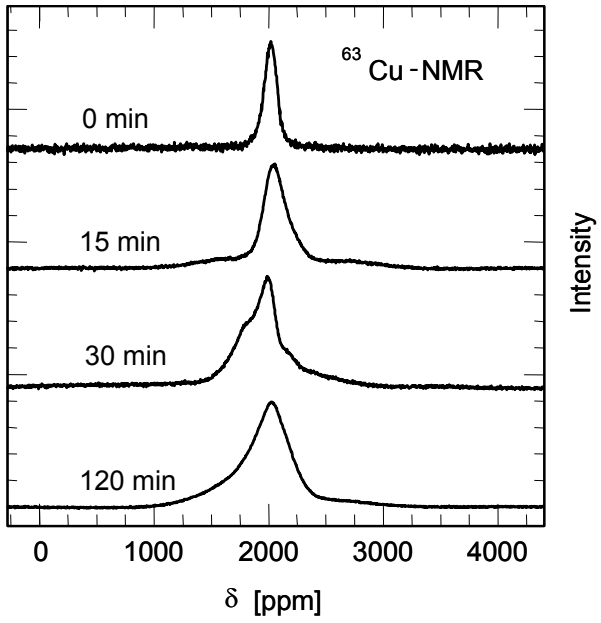

Figure 40 ^{63}Cu NMR spectra of four Cu/ZnO catalysts prepared from precursors aged for 0 min, 15 min, 30 min, and 120 min measured at 4.2 K.

The ^{63}Cu-NMR spectra of the differently aged Cu/ZnO catalysts are shown in Figure 40. The NMR spectra of the Cu/ZnO catalysts are in good agreement with the X-ray diffraction patterns. The NMR spectra of the catalysts obtained from precursors aged for 0 and 15 min exhibit a symmetric line broadening indicating large and well-ordered Cu particles. Conversely, the NMR spectra of the catalysts obtained from precursors aged for 30 and 120

min show an asymmetric line broadening corresponding to small and strained Cu nanoparticles. The results obtained for ^{65}Cu correspond to those for ^{63}Cu.

5.2.2.3 In situ XAS

X-ray absorption spectra of the Cu/ZnO catalysts were measured at the Cu K edge under methanol steam reforming reaction conditions at 523 K to analyze the short and medium range order structure of the Cu/ZnO materials obtained from differently aged precipitates. The resulting pseudo radial distribution functions ($FT(\chi(k)*k^3)$) of the four Cu/ZnO catalysts are compared in Figure 41a. Qualitatively, the $FT(\chi(k)*k^3)$ of the catalysts are very similar above 3 Å, whereas the peak at R = 2.2 Å (not phase-shift corrected), which is attributed to the first Cu-Cu distance in fcc copper metal, exhibits a strong increase in amplitude with increasing ageing time.

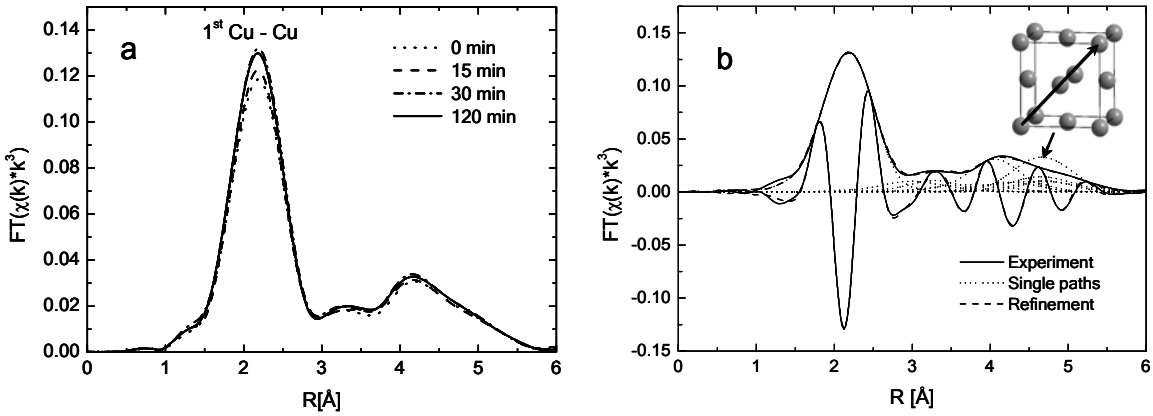

Figure 41 Experimental Cu K edge $FT(\chi(k)*k^3)$ of Cu/ZnO catalysts obtained from precipitates aged for 0, 15, 30 and 120 min measured at 523 K in methanol steam reforming gas mixture (a) and refinement of a theoretical EXAFS function (dashed) to the experimental Cu K edge $FT(\chi(k)*k^3)$ (solid) of a Cu/ZnO catalyst (b) (120 min ageing). The four most prominent single-scattering paths (dotted) in the EXAFS function together with one multiple-scattering path (arrow in unit cell) are depicted.

The result of a refinement of the Cu fcc model structure to the experimental Cu $FT(\chi(k)*k^3)$ of a Cu/ZnO catalyst (120 min ageing) together with the most prominent scattering paths are

shown in Figure 41b. The good agreement between theory and experiment indicates that no additional phases (e.g. copper oxides) are detectable in the EXAFS spectrum. The Debye-Waller factors of the multiple scattering path (Figure 41b) used to estimate the amount of microstrain in the Cu/ZnO catalysts obtained from the aged precipitates are given in Figure 40. An increase in the Debye Waller factor with ageing time is detected confirming an increase in microstrain in the copper particles. Conversely, the simultaneous decrease of the amount of Zn in the copper phase should yield a decrease in the Debye-Waller factor (i.e. an increase in amplitude) as seen in the first Cu shell of the corresponding Cu/ZnO catalysts (Figure 42). Therefore, the behavior of the particular "focusing" multiple scattering path as a probe for microstrain in the copper phase is in good agreement with the increase of microstrain as a function of precipitate ageing as obtained by XRD line profile analysis.

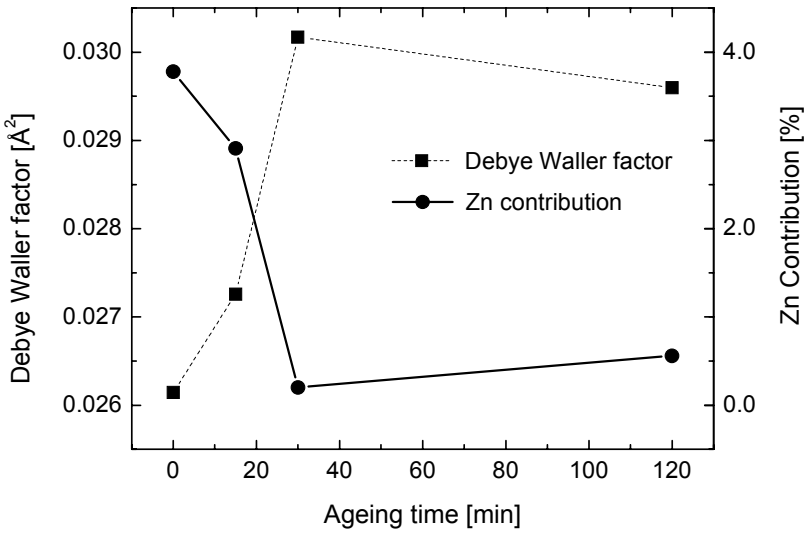

Figure 42 Debye-Waller factors of the multiple-scattering path indicated by the arrow in Figure 41 as function of precipitate ageing obtained by refinement of a theoretical Cu EXAFS function to the experimental FT(χ(k)*k^3) of four Cu/ZnO catalysts (0, 15, 30, and 120 min ageing) measured at 523 K together with (b) the contribution of a Cu-Zn shell to the Cu K edge FT(χ(k)*k^3) of the Cu/ZnO catalysts as function of precipitate ageing.

In addition, the distances of the first Cu shell in the four FT(χ(k)*k^3) Cu/ZnO catalysts were obtained from the EXAFS analysis. Figure 43 shows the evolution of the deviations in the distance of the first Cu shell (relative to a = 3.615 Å for bulk fcc copper) in comparison to the copper lattice constants determined by XRD refinement. The decrease in the distances of the

first Cu shell coincides with the decrease in copper lattice constant with ageing time. The lattice expansion of the Cu crystallites in the Cu/ZnO catalysts obtained from precipitates aged for 0 min and 15 min may indicate the presence of Zn occupying copper lattice sites as previously observed in Cu/ZnO catalysts with varying molar ratios [72, 85].

In order to quantify the amount of Zn in the Cu nanoparticles, an additional Zn shell with a Cu-Zn distance of 2.66 Å [86] was included in the theoretical EXAFS calculation. For the refinement, the distances of the Cu-Cu and the Cu-Zn scattering paths were kept constant, while the sum of the coordination numbers of the Cu-Cu and Cu-Zn scattering paths was constrained to be 12 in the refinement.

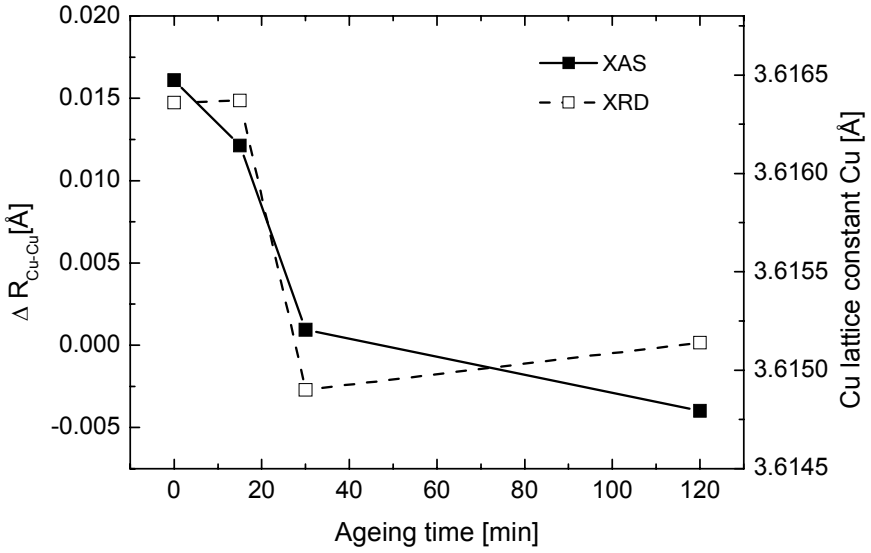

Figure 43 Variation of the Cu lattice parameter determined by XRD at 523 K under methanol steam reforming conditions and deviations in the distance of the first Cu shell obtained from an EXAFS refinement to the experimental Cu K edge FT(χ(k)*k^3) as a function of precipitate ageing.

The amount of Zn scatterers necessary to simulate the first shell of the experimental spectra of the four Cu/ZnO catalysts is shown in Figure 42 indicating a decreasing amount of Zn occupying Cu lattice sites in the catalysts obtained from precipitates aged for 30 min and 120 min. The increase in Cu-Cu distance of ~0.016 Å in the Cu/ZnO catalysts obtained from short-aged precipitates is about one order of magnitude larger than the corresponding lattice expansion of 0.0014 Å as detected by XRD. This discrepancy may be accounted for by the XAFS refinement procedure employed, which considers an average of the Cu-Cu distance (R_{Cu-Cu} = 2.55 Å) and the Cu-Zn distance (R_{Cu-Zn} = 2.66 Å) in the first shell. This may result

in larger distance deviations in the short-range order compared to the long-range lattice expansion as determined by XRD.

5.2.2.4 TEM

Transmission electron micrographs of Cu/ZnO catalysts obtained from a non-aged (0 min) and an aged (120 min) precipitate are depicted in Figure 44.

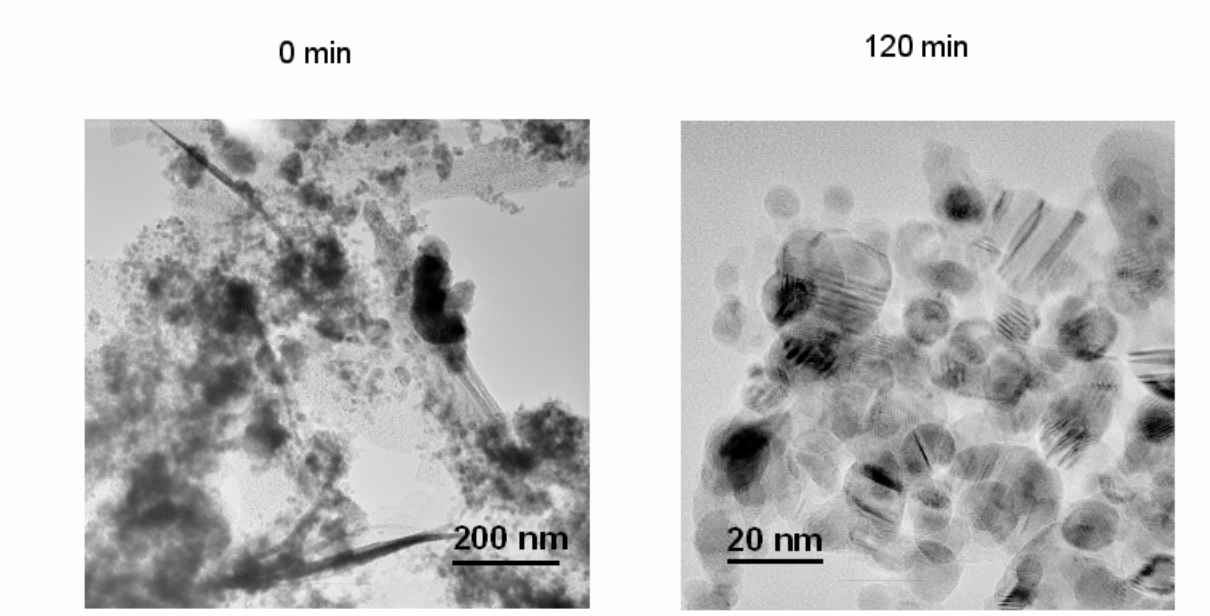

Figure 44 Transmission electron micrographs of Cu/ZnO catalysts obtained from hydroxycarbonate precipitates aged for 0 min and 120 min.

Electron diffraction and electron energy loss spectroscopy identified only Cu and ZnO as majority phases in the samples under investigation. Various morphologies of Cu and ZnO particles were detected in the Cu/ZnO catalyst obtained from non-aged precipitates, such as large isolated Cu particles, large ZnO plates and needles, and to a lesser amount nanostructured Cu and ZnO particles (Figure 44, 0 min). After 30 min of precipitate ageing, a transition to a homogeneous microstructure of the corresponding Cu/ZnO catalysts was observed. Although the catalyst obtained by 30 min precipitate ageing mainly contains

nanostructured Cu and ZnO particles, ZnO plates were also found as minor component. In the Cu/ZnO catalysts obtained from precipitates aged for more than 120 min, mostly nanostructured Cu/ZnO particles were found with only minute amounts of isolated Cu or ZnO particles detectable (Figure 45).

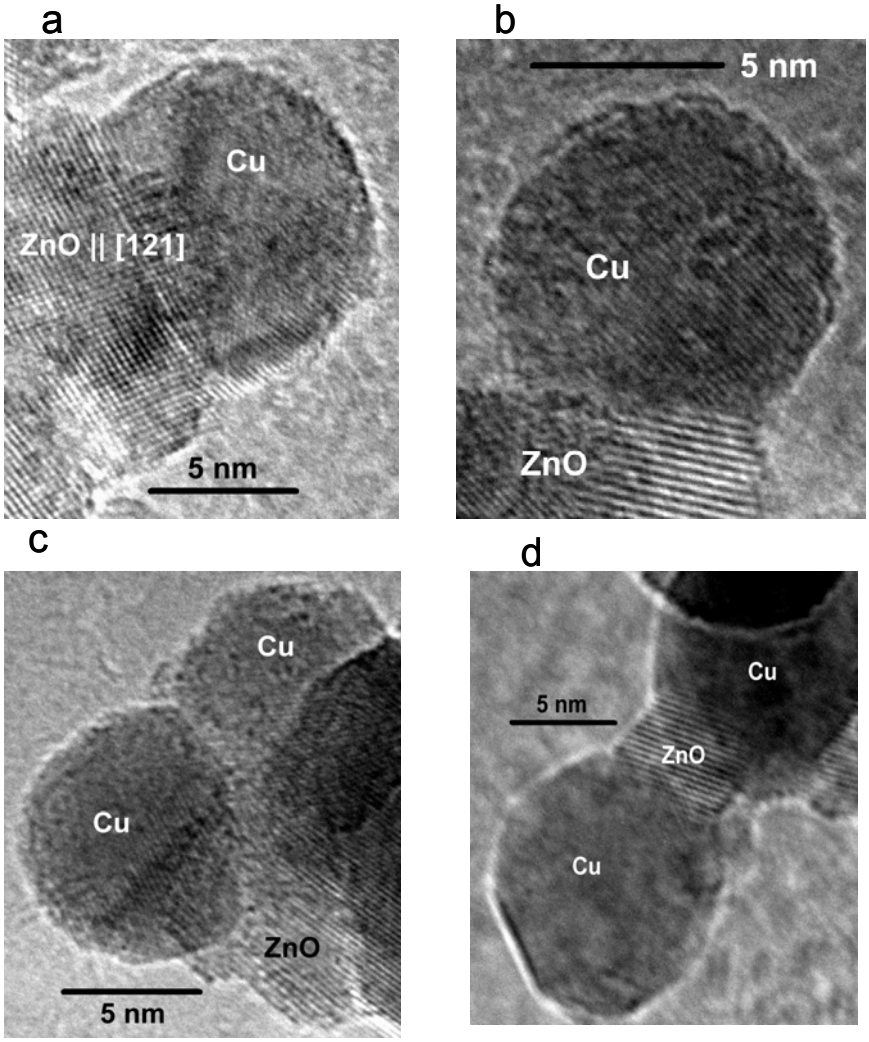

Figure 45 High-resolution transmission electron micrographs of a Cu/ZnO catalyst obtained from a copper zinc hydroxycarbonate precipitate aged for 120 min.

High-resolution electron micrographs show a marked interface between the Cu and ZnO particles (Figure 45 a and b). Well-defined copper clusters on large ZnO particles, like the ones observed in the model systems [87], are clearly absent in Cu/ZnO catalysts prepared similar to industrially used copper catalysts. The Cu and ZnO particles in the Cu/ZnO catalysts obtained from longer-aged precipitates are round-shaped or oval-shaped independent of their size. The high-resolution micrographs reveal a variety of epitaxial relations between

Cu and ZnO (e.g. Cu[110] || ZnO[100], Cu[111] || ZnO[100]) with an average contact angle between the Cu and ZnO particles of ~ 61 °. Zinc oxide exhibits a higher degree of structural order than the copper nanoparticles in the reduced Cu/ZnO catalyst, while the distinct defects in the ZnO structure may be indicative of the oxygen deficient nature of the ZnO particles in the catalysts. Moreover, ZnO particles are often found to be located between Cu particles, thus efficiently preventing them from sintering (Figure 45 c and d).

5.2.3 Discussion

The crystalline copper zinc hydroxycarbonate precipitates obtained after prolonged ageing results in Cu/ZnO catalysts that reveal a pronounced increase in MSR activity compared to the catalysts obtained from the originally amorphous precipitates (Figure 36). The Cu/ZnO catalysts obtained from long-aged precipitates exhibit a decreased copper crystallite size (Figure 39b) and an increased copper surface area (Figure 37a). However, the non-linear correlation of the normalized activity and the specific Cu surface area (Figure 37b) indicates that additional structural parameters govern the activity of the specific copper surface of the more active Cu/ZnO catalysts. The structural and catalytic properties of the Cu/ZnO materials studied confirm that in addition to the copper surface area, the increased microstrain in the nanostructured Cu particles as detectable by XRD (Figure 39a) and XAS (Figure 42) correlates with the improved MSR activity of Cu/ZnO. In addition to determining the microstrain in the copper nanoparticles by in situ XRD and EXAFS, we could show that ex situ ^{63}Cu nuclear magnetic resonance (NMR) spectroscopy investigations of the freshly reduced catalysts are in good agreement with the XRD results concerning the copper particle size and microstrain evolution as function of precipitate ageing (Figure 40). Moreover, tensile strain in the Cu nanoclusters was also reported by Wagner et al. based on Cu L_{III} edge ELNES measurements of Cu/ZnO model catalysts [90].

The influence of a strained copper bulk on the electronic properties of the surface was studied by theoretical calculations based on density functional theory [88]. These studies indicate, that strained copper surfaces can affect the catalytic activity because of changes in, for instance, adsorption energies and dissociation barriers of hydrogen. Investigations of single crystal model systems revealed that Cu 110 planes are more active in methanol synthesis and water

gas shift reaction than Cu 111 or Cu 100 planes [89]. However, as the effect of lattice strain on surface reactivity is more pronounced for Cu 111 surfaces than for Cu 100 or Cu 110 surfaces [90], it appears to be oversimplified to assign the observed increase in catalytic activity (Figure 36) to a change in the relative ratio of the Cu facets exposed. Furthermore, evaluation of various XRD lines in the patterns of the reduced Cu/ZnO catalysts revealed a strong anisotropy in Cu particle size and microstrain (Figure 39).

TEM images of the Cu/ZnO catalysts described here show a number of epitaxial relations between Cu and ZnO (e.g. Cu [111] || ZnO [110]), which explains the anisotropic distribution of microstrain in the copper particles. For the copper crystallite size, the anisotropy appears to be more pronounced for the catalysts obtained from short-aged precipitates, which is consistent with the heterogeneous microstructure of these materials.
The correlation between microstrain in the copper nanoparticles (Figure 39a) and catalytic properties (Figure 36) clearly indicates that the improved interface of Cu and ZnO in the long-aged catalysts has a considerable influence on the microstructure of the Cu nanoparticles and emphasizes the role of ZnO in determining the microstructure of the copper phase in addition to dispersing the copper particles and reduce sintering. The characteristic crystallization of the Cu-Zn hydroxycarbonate precipitates during ageing coincides with the increase in activity of the resulting Cu/ZnO catalysts. TEM investigations show that calcination of the amorphous precipitates results in a heterogeneous microstructure with a majority of separated CuO and ZnO crystallites and, hence, a less active Cu/ZnO catalysts upon reduction. Conversely, calcination and reduction of the crystalline precipitates obtained after ageing yields catalysts where CuO and ZnO are distributed in a homogeneous microstructure with small and disordered Cu crystallites with a distinct interface with ZnO. The higher degree of disorder in the Cu nanoparticles, which corresponds to an increased deviation from the “ideal” structure of bulk copper metal, results from an increased interface area between Cu and ZnO and is indicative of a more active copper catalysts.
High-resolution transmission electron microscopy (TEM) and in situ TEM studies have been performed on copper particles supported on ZnO with a copper concentration of less than 10 % [87,90]. These studies showed faceted well-ordered Cu particles on a large and well-defined ZnO support. Changes in the morphology of the Cu particles, the ratio of the copper facets, and the surface area upon varying the reduction potential of the gas phase were impressively illustrated by in situ TEM. However, these copper model systems were prepared by impregnation of ZnO crystals with a solution of Cu-acetate. This preparation procedure

deviates considerably from the preparation of industrially used catalysts (co-precipitation) and, hence, the well-defined model systems under investigation probably exhibit a microstructure different from that of a catalyst prepared for an industrial application.

In addition to the microstrain detected in the copper particles, the presence of Zn in both the CuO in the precursor and the Cu in the resulting catalyst emphasize the defect-rich state of the "real" structure of the copper phase in Cu/ZnO catalysts (Figure 42). The increase in the copper lattice constant (~3.616 Å) and the distance of the first Cu shell (Figure 43) of Cu/ZnO catalysts obtained from short-aged precipitates indicate a larger amount of Zn in the copper clusters compared to the Cu/ZnO catalysts obtained from long-aged precipitates (Figure 42). Bulk α-brass formation should only occur at temperatures above 580 K [78] while at a working temperature of the catalyst of 523 K the limit of Zn in Cu amounts to about 1 % Zn [91]. Higher oxygen vacancy concentrations at the ZnO surface may increase the tendency of α-brass formation in the copper bulk due to an enhanced diffusion rate through the Cu/ZnO interface and an improved miscibility of Cu and Zn in the real structure of the Cu/ZnO catalyst. It is more likely though, that the formation of a Cu-Zn alloys during reduction at 523 K is the direct consequence of the presence of Zn in CuO already in the CuO/ZnO precursors (Figure 27b and Figure 28a). It is evident from Figure 42 that the amount of Zn in the copper nanoparticles exhibits a negative correlation with the microstrain in the copper phase and the performance of the Cu/ZnO catalysts (Figure 36). Apparently, the presence of Zn in the copper particles is not the main source of the microstrain observed and is not required in the "real" structure of a more active Cu/ZnO catalyst.

5.3 Model of microstructural changes of real Cu/ZnO catalysts as function of ageing

The effect of precipitate ageing on the microstructural properties of the resulting Cu/ZnO catalyst is schematically depicted in Figure 46. The short-aged precipitates (0 min and 15 min) yield on average larger Cu and ZnO particles upon calcination and reduction (Figure 39b), which are more separated in these materials and exhibit a reduced Cu/ZnO interface. Assuming that copper microstrain originates from an epitaxial orientation of copper on ZnO, the lower strain in the copper particles is indicative for this reduced Cu/ZnO interface. In total, the larger Cu crystallite size, the reduced interaction between Cu and ZnO and the lower

degree of microstrain in the copper crystallites result in less active Cu/ZnO catalysts obtained from short-aged precipitates.

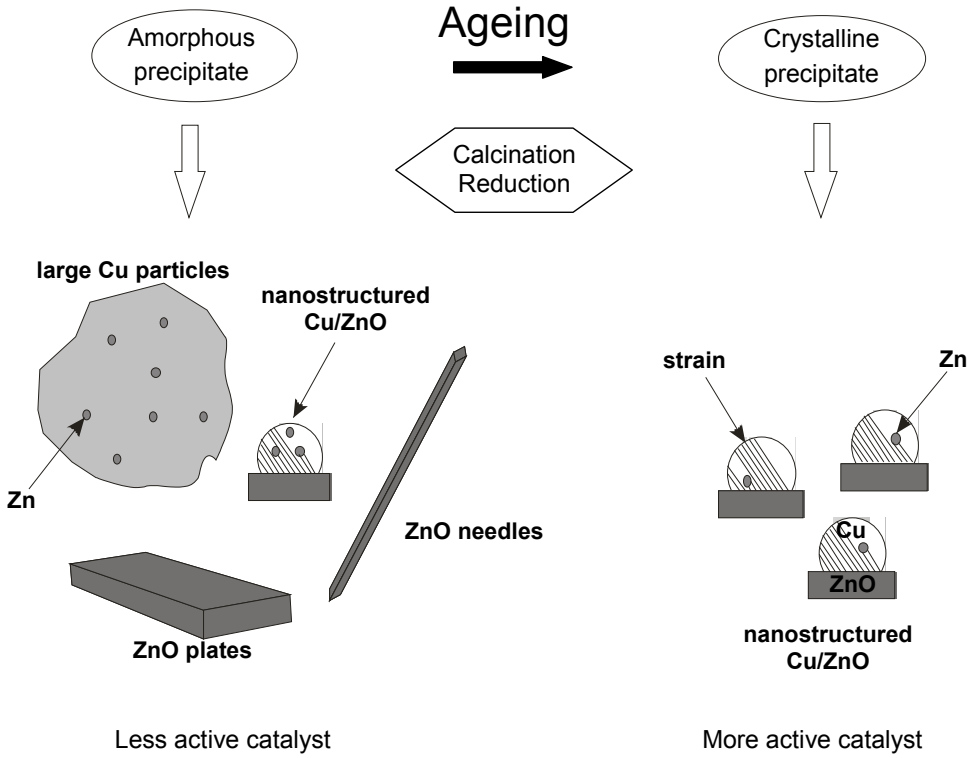

Figure 46 Schematic model of the microstructural characteristics of Cu/ZnO catalysts obtained from differently aged precipitates (amorphous (< 30 min), crystalline (> 30 min). Increasing ageing time leads to a more homogenous microstructure, a decrease in average copper crystallite size of the Cu/ZnO catalysts, and an increase in the microstrain in the copper clusters because of the improved interface between Cu and ZnO. Additionally, increased precipitate ageing results in a decreased amount of Zn in Cu.

Increasing the ageing time of the precipitates (30 min and 120 min) leads to in a more homogeneous microstructure of the resulting Cu/ZnO catalysts, which exhibits on average smaller Cu and ZnO crystallite sizes and higher copper surface areas. The improved interface between Cu and ZnO in these materials is indicated by the considerably higher degree of microstrain in the copper crystallites. Apparently, the crystalline precipitates obtained after prolonged ageing time possess a well-defined distribution of Cu and Zn centers in the hydroxycarbonates. Upon calcinations and reduction, this results in a reduced amount of Zn centers in both the calcined CuO/ZnO precursors and the reduced Cu/ZnO catalysts. In total,

the homogeneous microstructure and narrow crystallite size distribution of the Cu/ZnO catalysts obtained from long-aged precipitates in addition to the increased copper surface area and the degree of microstrain, as well as the decreased amount of Zn in Cu result in a much higher methanol steam reforming activity.

From the various methods described for the preparation of Cu/ZnO materials (impregnation, sol-gel synthesis, hydrothermal synthesis, chemical vapour deposition, mechanical milling) co-precipitation was found to be most suitable to prepare highly active Cu/ZnO catalysts [92]. Each precipitation parameter (pH, temperature, solvent, precipitation agent, additives, solution composition and ageing) as well as the post-treatment of the precipitates (washing, drying, calcination and reduction) may strongly influence the microstructure of the resulting Cu/ZnO catalyst. From the study described here it emerges, that modification of the ageing process such as stirring velocity and the volume of the precipitation vessel could exert a strong influence on the microstructure of the resulting Cu/ZnO catalyst. The effect of precipitate ageing on copper crystallite size and microstrain of the resulting Cu/ZnO catalyst is hardly influenced by slight modifications of a given preparation and ageing procedure and can be readily adjusted by proper control of temperature and pH. However, the time of transition from an amorphous to a crystalline precipitate and, hence, from a heterogeneous microstructure of a less active Cu/ZnO catalysts to a homogeneous microstructure of a more active catalysts, may depend on the amount of precipitate formed and may deviate from the ~30 min reported here.

6 Conclusion and Outlook

Microstructural characteristics of nanostructured copper zinc oxide catalysts for methanol steam reforming were investigated as a function of ageing of the precipitated hydroxycarbonates during catalyst preparation. Precipitate ageing is the first post-precipitation treatment and is accompanied by re-dissolution of the precipitates, recrystallisation, and crystal growth. The structure-activity correlations presented here indicate that crystallinity, phase composition, and homogeneity of the resulting precursor strongly influence the microstructural properties of the final copper catalyst. Hence, the structural characteristics of the precipitates as adjusted by an appropriate ageing procedure govern the properties of the final catalyst and are not annihilated by subsequent treatment procedures ("chemical memory" effect). The schematic model proposed for the structural characteristics of the active Cu/ZnO catalyst as a function of precipitate ageing emphasizes the defect-rich nature of the Cu and ZnO phase in the "real" structure of Cu/ZnO catalysts and its implication for the catalytic activity in the steam reforming of methanol. Adjusting the appropriate homogeneous microstructure while maintaining the same chemical composition yielded a strong increase in catalytic activity. The deviation of the "real" structure of more active copper catalysts from the "ideal" structure of bulk fcc copper metal confirms the requirement of "structural complexity" of superior heterogeneous catalysts instead of "chemical complexity".

With respect to a knowledge-based preparation of new materials, it emerges, that while a "good" precipitate can be turned into a "poor" catalyst by inappropriate treatment conditions, a "poor" precipitate may never again be transformed into a "good" catalyst. The characteristic transformation from originally amorphous precipitates into crystalline products is transmitted over the entire multi-step preparation including calcination and reduction. Therefore, microstructure design of superior heterogeneous catalysts has to start at the very first stages of catalyst preparation. It is thus important to monitor the formation of catalyst precursors during precipitation and precursor ageing by developing in-situ solid sensitive spectroscopy methods. The in-situ diffuse reflectance UV-Vis spectroscopy investigations during ageing in the mother liquor indicate a delayed crystallization of aurichalcite compared to the transition of the amorphous progenitor of rosasite (~30 min). Since the crystallinity of the precursor affects the microstructural homogenity of the catalyst and, thus, the catalytic activity, it can be

concluded that prolonged precipitate ageing after the main crystallization at approximately 30 min will result in an improved catalytic activity. A slight increase in the catalytic activity determined in the stainless steal reactor (~ 2.5 %) between 30 and 120 min ageing was observed, whereby the H_2 production rate determined in the XAS cell reveals the opposite trend. Further investigations have to follow in order to unravel the influence of prolonged precipitate ageing (< 30 min) on the microstructure of the catalyst and the resulting catalytic activity.

The nature and the origin of the residual carbonates (HT-CO_3) in the calcined precursor and the effect on the catalytic activity of the resulting catalyst could not be completely elucidated. In the present work, we were able to show that the HT-CO_3 species is mainly located at Zn centers (EXAFS and XPS, Zn edge). The complete decomposition of the carbonate species during reduction in the surface near region may cause a defect-rich ZnO_{1-x} species (x = number of oxygen vacancies). The "real" structure of zinc oxide in the catalyst deviates considerably from those of "ideal" hexagonal ZnO. Further studies will aim at elucidating the role of ZnO in the real catalyst and the nature of the residual carbonates, which is assumed to be the origin for the defect rich character of ZnO in the catalyst. A combined XAS/UV-Vis/MS experiment may help to unravel the origin of the HT-CO_3.

A lack of understanding of the performance-governing character of the early stages will render a successful design of new catalysts impossible. Hence, in addition to studying structure-activity relationships of solid catalysts, the "memory" of the material on proper and improper treatment of its precursor needs to be elucidated and considered in a rational catalyst design. Optimizing calcination and reduction conditions has to follow. The binary Cu/ZnO catalysts described here exhibit a reduced complexity with respect to the most active Cu/ZnO/Al_2O_3 catalyst. The results presented in this work enable to distinguish between an active and less active microstructure of the catalyst using XRD, XAS, NMR, and TEM, and, thus, the transfer of those results opens up the opportunity to identify the active microstructure of the more complex ternary system. Additionally, the effect of pH, temperature, stirring velocity, and reactor volume on the precursors formed during co-precipitation of ternary Cu,Zn,Al-hydroxycarbontes should be further investigated to enable a controlled adjusting of the appropriate homogenous microstructure.

7 Appendix

7.1 Publication Index

O. Bartels, A. Constantinescu, B. Kniep, K.D. Becker, *Möessbauer-Spektroskopie zur Untersuchung der Bildungskinetik von Eisennitriden und –carbiden*, Z. Anorg. Allg. Chem., **2002**, 628, 2192

B. Kniep, A.Constantinescu, D. Niemeier, and K.D. Becker, *An in-situ Study of the Formation of Cementite, Fe_3C*, Z. Anorg. Allg. Chem. **2003,** 629, 1795-1804

B.L. Kniep, T. Ressler, A. Rabis, F. Girgsdies, M. Baenitz, F. Steglich, R. Schlögl,

Rationales Design von nanostrukturierten Kuper-Zink-oxid Katalysatoren für die Methanol Dampf Reformierung, Angewandte Chemie **2004,** 116, 114-117

B.L. Kniep, F. Girgsdies, T.Ressler, *Microstructural Characteristics of Cu/ZnO Catalysts as Function of Precipitate Ageing for Methanol Steam reforming*, J. Catal., **2005,** submitted

T. Ressler, B.L. Kniep, I. Kassatkine, R.Schlögl, *Microstrucutre of Cu/ZnO catalyst - Bridging the gap*, Angewandte Chemie **2005**, in press

R.E. Jentoft, B. Kniep, M. Swoboda, T. Ressler, *Development of a Combined X-Ray absorption and UV-Vis In-Situ Spectroscopy*, Hasylab Annual report **2004**

M. Hävecker, B.L. Kniep, E. Kleimenov, P. Schnörch, D. Teschner, S. Zafeiratos, H. Bluhm, A. Knop-Gericke, T. Ressler, R. Schlögl, *Combined in situ XPS and in situ soft XAS study of Cu/ZnO catalysts for methanol steam reforming,* Bessy Annual Report **2004**

7.2 Curriculum Vitae

Benjamin-Louis Kniep
Fritz-Haber-Institut der MPG
Abteilung Anorganische Chemie
Faradayweg 4-6
14195 Berlin
Tel.: 030/8413-4444
Fax: 030/8413-4405
e-mail: kniep@fhi-berlin.mpg.de

Persönliche Daten

geboren am	06.11.1973
in	Leonberg / Baden-Württemberg
Staatsangehörigkeit	deutsch
Familienstand	ledig

Ausbildung

Aug.1985 - Juni 1993	Dietrich Bonhoeffer Gymnasium, Hilden, Abschluss: Abitur
Okt. 1993 - Okt. 1994	Wehrdienst / Marine
Okt. 1994 - Okt. 1996	Chemiestudium / Heinrich-Heine Universität Düsseldorf
Okt. 1996 - Mai 2000	Fortsetzung des Chemiestudiums / Technischen Universität Carolo-Wilhelmina zu Braunschweig, Abschluss: Dipl.-Chem.
Aug. 2000 - März 2001	Diplomarbeit: „ In-situ Untersuchungen zur Bildungskinetik von Zementit, Fe_3C“, Institut für Physikalische und Theoretische Chemie der Technischen Universität Braunschweig, Prof. K.D. Becker
Jan. 2002	Doktorarbeit: “Microstructural Modifications of Copper Zinc Oxide Catalysts as Function of Precipitate Ageing”, Fritz-Haber-Institut der Max-Planck Gesellschaft, Prof. R. Schlögl

7.3 List of Figures

7.4 References

1 Key World Energy Statistics, International Energy Agency, **2004**, 6

2 J.J. Spivey, Catalysis Royal Society of Chemistry, 16, **2002**, 73-131

3 L. Alejo, R. Lago, M.A. Pena, J.L.G. Fierro, Appl. Catal. A., 162, **1997**, 281

4 S. Velu, K. Suzuki, T. Osaki, Catal. Lett., **2000**, *69*, 43-50

5 E. Ruckstein, Y.H. Hu, Appl. Catal. A, **1995**, *133*, 149

6 V.R. Choudhary, B.S. Uphade, A.S. Mamman, Catal. Lett., **1995**, *32*, 387

7 M.C.J. Bradford, M.A. Vannice, Appl. Catal. A., **1996**, *142*, 73

8 W. Vielstich, A. Lamm, H.A. Gasteiger, Hanbook of Fuel Cells, **2004**, 132

9 J.P. Breen, J.R.H. Ross, Catal Today, **1999**, 51, 521

10 C.J. Jiang, D.L. Trimm, M.S. Wainright, N.W. Cant, Appl. Catal. A. **1993**, 97, 145

11 K. Takahashi, H. Kobayashi, N. Takezawa, Chem. Lett., **1985**, 6, 759

12 H. Purnama, T. Ressler, R.E. Jenthoft, H. Soerijanto, R. Schlögl, R. Schomäcker, Appl. Catal. 259, **2004,** 83

13 N. Takezawa, N. Iwasa, Catal. Today, **1997**, 36, 45

14 B. Lindström, L.J. Petterson, Proc 2000 Fuel Cell Seminar, Portland, Oregon, **2000**, 325

15 H. Kobayashi, N. Takezawa, C. Minochi, Chem. Lett. **1976**, 1347.

16 H.G. El-Shobaky, M. Mokhtar, G.A. El-Shobaky, Appl. Catal. A ,**1997**,162, 281.

17 B. Bems, M. Schur, A. Dassenoy, H. Junkes, D. Herein, R. Schlögl, Chem. Eur. J. 9, **2003** 2039

18 J-L. Li, X.-G. Zhang, T. Inui, Appl. Catal. A ,147, **1996**, 23

19 D. Jingfa, S. Qi, Z. Yulong, C. Songying, W. Dong, Appl. Catal. A., 139, **1996**, 75

20 Ernee Muhamad, Master Thesis, **2005**

21 Z.-S. Hong, Y. Cao, J-F Deng, K.-N. Fan, Catal. Lett., 82, **2002**, 37

22 R. Becker, H. Parala, F. Hipler, O.P. Tkachenko, K.V. Klementiev, W. Grünert, H. Wilmer, O. Hinrichsen, M. Muhler, A. Birkner, C. Wöll, S. Schäfer, R.A. Fisher, Angew. Chem. Int. Ed., 43, **2004**, 2839

23 H.L. Castricum, H. Bakker, B. van der Linden, E.K. Poels, J. Phys. Chem. B, **2001**, 105, 7928

24 M.S. Spencer, Top. Catal. 8, **1999**, 259

25 G. Sengupta, D.P. Das, M.L. Kundu, S. Dutta, S.K. Roy, R.N. Sahay, K.K. Mishra, Appl. Catal. 55, **1989**, 165

26 T. Shishido, Y. Yamamoto, H. Morioka, K. Takaki, K. Takehira, Appl. Catal A, 263, **2004**, 249

27 M.S. Spencer, Catal. Lett. 66, **2000**, 255

28 H. Clöfen, S. Mann, Angew. Chem. 115, **2003**, 2452-2468

29 J.W. Gibbs, Collected Works, Vol. 1, Dover, New York, **1961**, 252

30 N. Jongen, P. Bowen, J. Lemaitre, J.C. Valmalette, H. Hoffman, J. colloid Interface Sci., 266 **2000**, 189

31 S.H. Lee, Y.S. Her, E. Matijevic, J. Colloid Interface Sci. 186, **1997,** 193

32 R. Boistelle, J.P. Astier, J. of. Cryst. Growth, 90, **1988**, 14

33 W. Ostwald, Z. Physik. Chem. , 22, **1897**, 289

34 P.T. Cardew, R.J. Davey, Proc. R. Soc. Lond. A 398, **1985**, 415

35 T. Fujitani, J. Nakamura, Catal. Lett. 56, **1998**, 119

36 M.M Günter, T.Ressler, B.Bems, C.Büscher, T.Genger, O.Hinrischsen. M.Muhler and R.Schlögl, Catal. Lett. 71, **2001**, 37

37 J.-L. Li, T. Inui, Appl. Catal. A, 137, **1996**, 105

38 M. Schur. B. Bems, A. Dassenoy, I. Kasatkine, J. Urban, H. Wilmes, O. Hinrichsen, M. Muhler, S. Schlögl, Angew. Chem. Int. Ed., 42, **2003**, 3815

39 D.Waller, D. Stirling, F.S. Stone, M.S. Spencer, Farad. Disc. 87, **1989**, 107

40 S.H. Taylor, G.J. Hutchings, A.A. Mirzaei, Catalysis Today 84 ,**2003**, 113

41 D.M. Whittle, A.A. Mirzaei, J.S.J. Hargreaves, R.W. Joyner, C.J. Kiely, S.H. Taylor, G.J. Hutchings, Phys. Chem. Chem. Phys. 4 ,**2002**, 5915

42 R.A. Young, The Rietveld Method, Oxford University Press, **1993**

43 G.K. Willamson, W.H. Hall, Acta. Metall., 1, **1953,** 22

44 T. Ressler, J. Wong, J. Roos, I.L. Smith, Environ.Sci.Technol. 34, **2000**, 950

45 W. Kraus, G. Nolze, Bundesanstalt für Materialwissenschaften unf –prüfung (BAM), Berlin

46 D.E. Sayers, E.A. Stern, F.W. Lytle, Phys. Rev. Lett., 27, 1971, 1204

47 A.L. Ankudinov, B. Ravel, J.J. Rehr, S.D. Conradson, Phys Rev B,58 ,**1998**, 7565

48 T. Ressler, J. Synch. Radiat., 5 ,**1998**, 118

49 T. Ressler, J. Wong, J. Roos, I.L. Smith, Environ.Sci.Technol., 34 , **2000**, 950

50 J.C. Linden, G.E. Tranter, J.L. Holmes, Encyclopedia of Spectroscopy and Spectrometry, vol 2, **2000**

51 J.W. Ewans, M.S. Wainright, A.J. Bridgewater, D.J. Young, Appl. Catal. 7, **1983**, 75.

52 Design of the original XAS cell for time resolved measurements done by Michael Hagelstein and Thomas Neisius in a cooperation between ID24 ar ESRF and Fritz-Haber-Institute

53 The malachite reference was taken from the NASA, California Institute of Technology, UV-Vis library

54 A.N. Pestryakov et al., Chem. Phys. Lett., 385, **2004,** 173

55 S. Velu, K. Suzuki, M. Okazaki, M.P. Kapoor, T. Osaki, F. Ohashi, J. Catal., 194, **2000**, 373

56 F. Boccuzzi, S. Coluccia, G. Martra, and N. Ravasio, J. Catal. 184, **1999**, 316

57 C.Y. Fong et al., Phys. Rev. Lett., 25, **1970**, 1486

58 L Wang, N.C. Gilles, J. Appl. Phys., 94, **2003**, 973

59 K Klier, Adv. Catal. 31, **1982**, 243

60 X. Gao, M.A. Banares, I.E. Wachs, J. Catal. 188, **1999**, 325

61 I.L. Botto, M.B. Vassallo, E.J. Baran, G. Minelli, Mat. Chem. Phys. 50, **1997**, 267

62 D.M. Whittle, A.M. Mirazei, J.S.J. Hargreaves, R. W. Joyner, C.J. Kiely, S.H. Taylor, G.H. Hutchings, PCCP, 4, **2002**, 5915

63 S.H. Taylor, G.H. Hutchings, A.A. Mirazei, Catal. Tod. 84, **2003**, 113

64 M.M. Harding, B.M. Kariuki, R. Cernik, G. Cressey, Acta Cryst. B, 50, **1994**, 673

65 R.J. Reddy, F. Nieto, A.S. Navas, N. Jb. Miner. Mh, 7, **2004**, 302

66 Wu-Hsun Cheng, Mat. Chem. Phys. 41, **1995**, 36

67 G.J. Millar, I.H. Holm, P.J.R. Uwins, J. Drennan, J.Chem.Soc, Faraday Trans. 94, **1998**, 593

68 T.M. Yurieva, React. Kinet. Catal. Lett. 55, **1995**, 513

69 B.S. Clausen, L. GrÅbæk, H. Topsoe, L.B. Hansen, P. stolze, J.K. Norskov. O.H. Nilsen, J. Cata. 141, **1993**, 386

70 D. Prabhakaran, A.T. Boothroyd, J. Cryst. Growth , **2003,** 77

71 R.A. Brozi, S.J. Stewart, G. Punte, R.C. Mercader, R.D. Zysler, M. Tovar, Solid State Comm.,

2001, 311

72 M.M. Günter, T. Ressler. R.E. Jentoft, B. Bems, J. Catal. 203, **2001**, 133

73 T. Ressler, B.L. Kniep, I. Kasatkin, R. Schlögl, Angew. Chem. 2005, accepted

74 J. Sloczynski, R. Grabowski, A. Kozlowska, P. K. Olszewski, J. Stoch, Phys. Chem. Chem. Phys. 5 , **2003**, 4631

75 J.Y. Kim, J.A. Rodriguez, J. C. Hanson, A.I. Frenkel, P.L. Lee, J. Am. Chem. Soc. 125 , **2003** 10684

76 G. Petrini, F. Montino, A. Bossi, F. Grabassi, Preparation of Catalysts III, Elsevier, Amsterdam, **1983**, 735

77 R.G. Herman, K. Klier, G.W. Simmons, B.P. Finn, J.B. Bulko, T.P. Kobylinski, J. Catal., 56, **1979**, 407

78 Y. Knai, T. Wanatabe, T. Futjitani, M. Saito, J. Nakamura, T. Uchijama, Catal. Lett. 27 ,**1994** 67

79 J. Nakamura, I. Nakamura, T. Uchijama, Y. Kanai, T. Wanatabe, M. Saito, T. Fujitani, Cata. Lett. 31, **1995**, 325

80 T. Futjitani, J. Nakamura, Appl. Cata. A 191 , **2000**, 111

81 B.S. Clausen, J. Schiøtz, L. Gråbæk, C.V. Ovensen, K.W. Jacobsen, J.K. Norskov, H.Topsøe, Top. Catal. , **1994**, 367

82 R. Burch, S.E. Golunski, J. Chem. Soc. Faraday Trans. 86 , **1990**, 2683

83 A.-V. Chadwick, I.-J.-F. Popett, D.-T.-S. Maitland, M.E. Smith, Chem. Mater. 10, **1998**, 864

84 B.H. Suits, M. Meng, R.W. Siegel, Y.X. Liao, J. Mater. Res., 9, **1994**, 336

85 H. Berndt, V. Briehn, S. Evert, Appl. Catal. A 86 , **1992**, 65

86 J.D. Grunwaldt, A.M. Molenbroek, N.-Y. Topsøe, H. Topsøe,, B.S. Clausen, J. Catal. 194, **2000**, 452

87 P.L. Hansen, J.B. Wagner, S. Helveg, J.R. Rostrup-Nielsen, B.S. Clausen, H. Topsoe, Science 295, **2002**, 2053.

88 S Sakong, A. Groß, Surface Science 525, **2003**, 107

89 J.Yoshihara, C.T. Campbell, J. Catal. , **1996**, 776

90 J.B. Wagner, P.L. Hansen, A.M. Molenbroek, H. Topsoe, B.S. Clausen, S. Helveg, J. Phys. Chem. B 107, **2003**, 7753

91 M.S. Spencer, Surface Science 192, **1987**, 323

92 R.A. Brozi, S.J. Stewart, G. Punte, R.C. Mercader, R.D. Zysler, M. Tovar, Solid State Comm., **2001**, 311